The Photodynamic and Structural Analyses of Advanced Materials for Solar Fuel Conversion

Brian Pattengale
Marquette University

Recommended Citation
Pattengale, Brian, "The Photodynamic and Structural Analyses of Advanced Materials for Solar Fuel Conversion" (2018). *Dissertations (2009 -)*. 789.
https://epublications.marquette.edu/dissertations_mu/789

THE PHOTODYNAMIC AND STRUCTURAL ANALYSES OF ADVANCED MATERIALS FOR SOLAR FUEL CONVERSION

by

Brian A. Pattengale

A Dissertation submitted to the Faculty of the Graduate School,
Marquette University,
in Partial Fulfillment of the Requirements for
the Degree of Doctor of Philosophy

Milwaukee, Wisconsin

August 2018

ABSTRACT

THE PHOTODYNAMIC AND STRUCTURAL ANALYSES OF ADVANCED MATERIALS FOR SOLAR FUEL CONVERSION

Brian A. Pattengale

Marquette University, 2018

Mitigating the current and future climate and pollution issues that have been brought on by the combustion of fossil fuels is of utmost importance and will rely on, in part, the availability of renewable fuel sources. Of the possible sources of energy, solar is abundant, but must be harnessed efficiently and stored as a solar fuel to overcome the current storage issues that limit photovoltaic cells. One such fuel, $H_2(g)$, represents a carbon-neutral source of energy if it can be efficiently liberated from water via the water splitting reaction. Thus, much attention is focused on designing materials to perform the water splitting reaction efficiently as well as fundamentally understanding the complex dynamics that occur during the coupled light-harvesting and catalytic events that comprise photocatalysis. Herein, these concepts are applied to two classes of materials with a focus on their application to solar fuel photocatalysis.

One class of materials that has shown promise as an oxygen evolution reaction (OER) catalyst is bismuth vanadate ($BiVO_4$) due to its visible light absorption, stability, and photocatalytic ability. However, fundamental understanding of the factors that limit the photocatalytic efficiency of $BiVO_4$ toward OER are poorly understood. Chapter 3 focuses on both revealing and resolving the limiting attributes of $BiVO_4$, thereby significantly enhancing its photocatalytic OER efficiency.

A second class of emerging materials investigated are porous zeolitic imidazolate frameworks (ZIFs), a subclass of metal organic frameworks (MOFs). The excited state dynamics of ZIF-67 are characterized in chapter 4, demonstrating a long-lived charge separated (CS) state in the material after photoexcitation. The understanding of the nature of this CS state is then extended by optical studies that reveal metal-to-metal charge transfer (MMCT) as a contributing mechanism to charge separation in ZIFs. A further study then shows that the electron in this CS state can be extracted through interfacial electron transfer from excited ZIF to an organic dye species providing crucial insights into the ability of ZIFs as intrinsic photocatalyst materials. Following these fundamental studies, ZIF-67 is applied as an efficient hydrogen evolution reaction (HER) photocatalyst in conjunction with an auxiliary photosensitizer in chapter 5.

ACKNOWLEDGEMENTS

Brian A. Pattengale

Throughout my graduate career at Marquette, I have had the pleasure of being surrounded by many great people, without whom this work could not have been completed. I would like to first extend my most sincere thanks to my advisor, Prof. Jier Huang, for her guidance and advice throughout my graduate studies. She constantly challenged me to grow as a scientist and patiently gave me space to work through the hurdles that research presented to me; her example will surely guide me as I transition into the next phase of my professional career. I would additionally like to thank the current members of our group, specifically Sizhuo and Wenhui, for helping prepare numerous samples, bouncing ideas back and forth, and for many long hours helping with around the clock synchrotron X-ray absorption experiments without which these studies could not have been completed.

I am gracious for the excellent staff and faculty at the Marquette Chemistry department that maintain a supportive, positive, and collaborative environment to perform research in. I would like to also thank my committee members for their guidance throughout my graduate career. I thank Prof. Scott Reid for his advice and encouragement related to pursuing a doctoral degree. I also owe thanks to the late Prof. Rajendra Rathore for motivating me to perform at my highest level from the very beginning of my graduate career during combined group meetings through several program checkpoints.

As mentioned above, synchrotron X-ray absorption experiments were a crucial component of much of the research herein. I am grateful for the staff at the Advanced Photon Source at Argonne National Laboratory for their guidance and help in performing these experiments. I would like to give a special thanks to Xiaoyi Zhang for her numerous long hours setting up and assisting with time-resolved measurements and her help in better understanding X-ray science.

I would not be the person that I am, or in the position that I am in, without the love and support of my parents Dave and Rochelle. They instilled in me the value of education, both formal and informal, and were supportive of me through the highs and lows of my graduate education. I thank them for this and so much more; the depth of my gratitude for the life I was given by these two cannot be expressed in words.

Finally, I would like to thank my wife Hannah, as I couldn’t have done any of this without her. She has supported my dreams and decisions since our very first year of undergraduate, often at great sacrifice, and motivates me to be the best me that I can be. Thank you for your love, your patience, and the many laughs that make life so much fun.

TABLE OF CONTENTS

CHAPTER

LIST OF TABLES

LIST OF FIGURES

Chapter 1

INTRODUCTION

1.1 Need for Renewable Energy Sources

In response to climate change and pollution that have been brought on by the combustion of fossil fuels, renewable energy sources are necessary for a sustainable society in the future. Renewable energy sources, including solar, geothermal, wind, and hydroelectric[1-4] have been under rigorous development in recent years due to the threat of climate change and the need to meet rising global energy demands. These technologies are all related by one unifying similarity – utilization of naturally-occurring forces and forms of energy to produce carbon-neutral energy usable by modern society. They also suffer from the same flaw that has propagated fossil fuel use in the past two to three centuries – the energies captured by renewable sources need to be stored in a form that is efficient, transportable, and available for widespread use.[5] Of the available sources of renewable energy, abundant solar energy represents the most promising line for development; sunlight provides $3x10^{24}$J of energy per year, exceeding the yearly global energy demand by four orders of magnitude.[6] Thus, solar energy systems have the potential to outcompete finite fossil fuel sources if they can be made with high efficiency and low cost.

1.2 Artificial Photosynthesis

While currently implemented solar energy systems focus predominantly on Si-based p-n junction photovoltaic cells that convert sunlight directly into electrical current, they suffer from difficulties in storing electrical energy using the current battery technologies available. One of the solutions to the energy storage issue that arises from photovoltaic cells is to couple the light-harvesting event directly with the formation of chemical bonds that store the energy in a stable compound termed a solar fuel, i.e. a stable, energy dense compound synthesized from solar energy input that can be later utilized to generate energy. This idea is far from novel, as nature has been performing this process, natural photosynthesis, for billions of years.

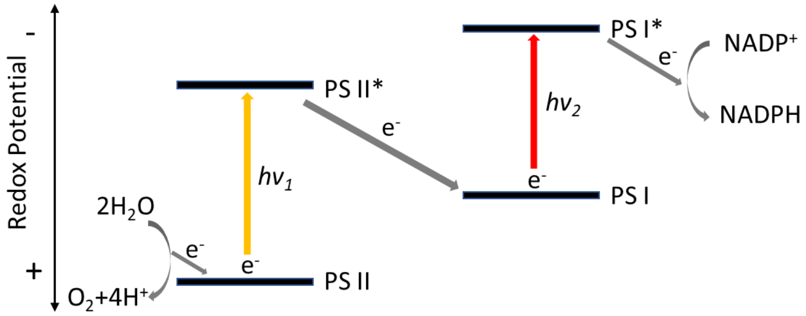

Figure 1.1. Schematic diagram for natural photosynthesis. Photosystem II (PS II) and Photosystem I (PS I) are photoexcited by different photon energies shown as hv_1 and hv_2.

The schematic diagram for natural photosynthesis is shown plotted against an arbitrary redox potential axis in Figure 1.1. Photosynthesis occurs by photoredox-mediated transfer of electrons from water to the final electron acceptor, CO_2, following a Z-scheme to perform the necessary redox reactions.[7-9] The light absorbing pigments in photosystem II (PS II) first absorb light to be promoted to their excited state, where the electrons in the excited pigments move down a potential gradient in the electron transport chain to eventually reach Photosystem I (PS I). The highest occupied molecular orbital (HOMO) of PS II is at a potential more positive than the water oxidation potential, allowing the oxidation of water at Mn oxygen evolution center to regenerate the ground state PS II. PS I, which is shifted to a more negative potential with respect to PS II, is a better reductant than PS II in its excited state and can reduce $NADP^+$ to NADPH, which acts as reducing redox mediator to eventually perform CO_2 fixation. In this manner, the photosynthetic scheme utilizes two separate reaction centers to perform oxidation and reduction reactions with the spatial separation of the electron and hole occurring via intermediate species prior to the slow OER catalysis step. Additionally, the redox potentials of the HOMO and lowest unoccupied molecular orbital (LUMO) of each photosystem are tuned such that only PS II can perform the oxidative OER, and only PS I can perform the respective reduction reaction. Furthermore, each photosystem is tuned to absorb slightly different regions of the Visible-NIR spectrum, ensuring that the light absorption of each photosystem isn’t completely parasitic to the other.

Artificial photosynthesis is a process that aims to mimic the important steps in natural photosynthesis in order to produce solar fuel with the final reduction step.[10-12] Much attention has been focused on utilizing this scheme by the formation of H_2 gas, simple hydrocarbons, or other solar fuels.[6] The generation of $H_2(g)$ can be accomplished by performing the water splitting reaction (Equation 1.1):

$$2H_2O \rightarrow O_{2(g)} + 2H_{2(g)} \tag{1.1}$$

$$2H_2O \rightarrow O_{2(g)} + 4H^+ + 4e^- \qquad (E^o = +1.23V \text{ vs. NHE}) \tag{1.2}$$

$$2H^+ + 2e^- \rightarrow H_{2(g)} \qquad (E^o = 0V \text{ vs. NHE}) \tag{1.3}$$

The OER and HER half-reactions (Equations 1.2, 1.3 respectively) are shown with their standard electrochemical potentials vs. NHE. While the HER step is facile, the OER step requires a +1.23 V driving force that calculates to approximately 237 kJ/mol. Further complicating the OER step are the complex kinetics associated with four oxidizing equivalents (holes) reaching the surface of the electrocatalyst to perform redox chemistry with two molecules of H_2O. Thus, efficiently performing OER electrochemically is an active area of research. However, a more attractive approach is to directly utilize light energy to overcome the energetic barriers associated with water splitting.

The basic overview of natural photosynthesis outlines three important considerations that need to be replicated in any artificial photosynthetic system: 1) absorption of significant portion of the solar spectrum, 2) efficient charge-separation mechanisms, and 3) separated reaction centers with tuned redox potentials. The first artificial photosynthetic system that performs the water-splitting reaction (Eq. 1.1) was the photoelectrochemical cell (PEC) developed by Fujishima and Honda in 1972.[2]

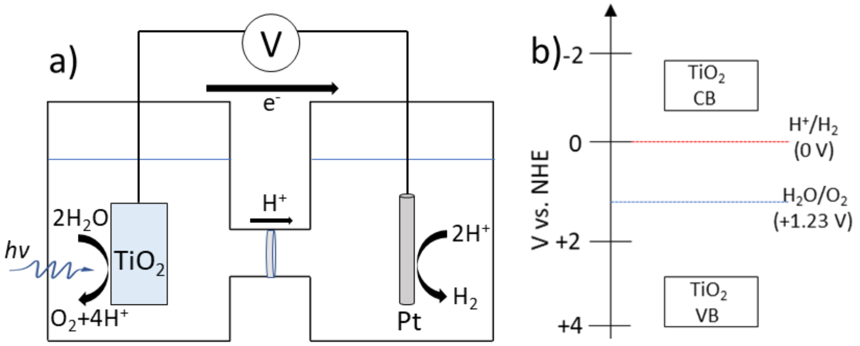

Figure 1.2. Fujishima and Honda PEC cell (a) and TiO_2 band diagram[13] on electrochemical scale vs. NHE(b).

Figure 1.2a shows the historic PEC developed by Fujishima and Honda. The construction of the system is based on the concept of separating the OER and HER centers of the water splitting reaction by utilizing different materials tailored to each reaction, thus following the schematic of natural photosynthesis. On the OER side of the device, an n-type semiconductor, TiO_2, was used as the photoanode. The complementary HER reaction was performed by a well-known HER catalyst, Pt metal. The operation of the device occurs by photochemical OER at the TiO_2 photoanode, producing electrons and protons (Equation 1.2). The electrons travel to the Pt counter electrode while protons move into the other compartment along their diffusion gradient through a proton-selective membrane, after which HER reaction takes place at the Pt electrode.

The diagram in Figure 1.2b illustrates the simplified band diagram of TiO_2 plotted on an electrochemical scale along with the redox potentials of OER and HER in order to represent the energetics of the Fujishima and Honda cell. In this system, TiO_2 has a large bandgap (3.2eV) so it can only absorb UV light. If irradiated with light of sufficient energy, the generated electron-hole pair can either recombine or separate such that the electron and hole can perform their respective redox chemistries. Due to the redox potentials of OER and HER, and electron in the conduction band will have sufficiently negative electrochemical potential to reduce H^+ to H_2(g). Likewise, the valence band position is sufficiently positive to accept electrons from (or to transfer its holes to) H_2O. Thus, after photoexcitation, holes can perform OER while electrons are transferred to Pt, where they then have sufficient potential to perform HER by reducing protons that have moved to the HER compartment. To assist the OER reaction to occur, an oxidizing potential can also be applied to the photoanode in conjunction with illumination to further assist charge separation and to increase the overpotential.

Of the three vital criteria defined to mimic natural photosynthesis, the Fujishima-Honda cell, referred to henceforth as a photoelectrochemical cell (PEC), meets only one: the existence of a charge separation mechanism due to the band bending effect at the semiconductor-electrolyte interface that assists interfacial charge separation.[14] Because of the deficiencies present in the original Fujishima-Honda cell design, much work has been focused on improving PEC designs by, largely, two main methods: 1) utilizing a photoanode material or hybrid material that is capable of harvesting visible light and 2) replacing expensive metal Pt electrode with a photocathode material that can absorb light to drive HER efficiently.

Visible Light Absorbing PEC Photoanode Materials

While the TiO_2 system presented in the Fujishima-Honda cell achieves the overall photocatalytic water-splitting reaction, it is unable to do so efficiently in real world applications due to the lack of visible light absorption. One method to harvest visible light without changing the photoanode material uses a concept developed by Michael Grätzel in his pioneering work on dye-sensitized solar cells utilizing mesoporous TiO_2.[1,6] Rather than utilizing the bandgap transition of TiO_2 to populate its conduction band, a visible light absorbing dye molecule is anchored to the surface of the TiO_2 semiconductor, where the dye molecule with highly negative excited state oxidation potential with respect to the TiO_2 conduction band (CB) position injects an electron into the CB of TiO_2 after photoexcitation. This process generates an oxidized dye molecule that must then be regenerated by electrons from OER. This device, known as a dye-sensitized water splitting cell[15] is outlined schematically in Figure 1.3.

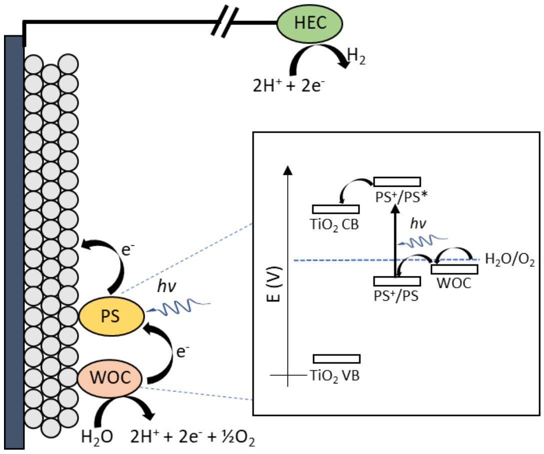

Figure 1.3. Schematic representation of a dye-sensitized water splitting cell based on mesoporous TiO_2. The device design is shown at left, with integrated water oxidation catalyst (WOC) and photosensitizer (PS). The simplified energetic diagram is shown at right.

Because many of the dye molecules typically utilized (such as porphyrins,[16-18] Ru-polypyridyl dyes,[19-21] etc.) are not efficient OER catalysts themselves, an optimized system would have an efficient OER catalyst present to relay electrons from water to the oxidized dye, termed a water oxidation catalyst (WOC). One type of WOC that offers high synthetic tunability is a homogeneous molecular catalyst such as Ru complexes,[22,23] Ru-dimer complexes,[24-26] Ir-based complexes,[27,28] and recently developed molecular catalysts based on earth abundant metals such as Fe[29-31] and Co.[32,33] Another appropriate catalyst type is a heterogeneous catalyst such as IrOx,[34-36] Co_3O_4,[37-39] CoPi,[40,41] MnOx,[42,43] etc. and the catalyst can either functionalize an existing electrode, such as TiO_2, as layers or nanostructures, or can act as the photoanode themselves.

While this strategy of using a dye-sensitized photoanode to perform OER has the advantage of utilizing a high extinction coefficient molecular moiety to drive photocatalysis, it is disadvantaged by increased complexity, the possibility of dye degradation, dye or catalyst leaching, etc. To overcome the possible issues in dye-sensitized TiO_2 photoanode, one strategy is to utilize a different semiconductor material with smaller bandgap that is capable of absorbing visible light and appropriate VB edge to drive OER, thus eliminating the complex catalyst-dye-semiconductor design.

Because the potential difference required for OER is approximately 1.23V, the semiconductor photoanode materials must, in principle, have a bandgap > 1000 nm in order to drive OER provided that the VB edge is sufficient to drive OER. However, in reality, electrons must transfer between semiconductor and liquid phase junctions, resulting in energy losses and, additionally, overpotentials are required to drive OER efficiently.[44] As a result, the ideal bandgap range for a single-absorber photoanode is in the range of 1.6-2.4 eV, representing a balance between maximum absorption of solar irradiation and proper overpotentials.[45,46] While many metal oxide and metal sulfide semiconducting materials fit this criteria,[47] two materials that have been under extensive development are hematite, Fe_2O_3,[48-51] and bismuth vanadate, $BiVO_4$, the latter of which is discussed in detail in a following section.

Visible Light Absorbing PEC Photocathode Materials

Beyond the single-absorber PEC with light absorbing photoanode, there is also great opportunity to develop PEC schemes that more closely resemble natural photosynthesis by incorporating light absorbing semiconductor materials in the photocathode. The criteria for such photocathode materials is that their CB edge needs to be more negative than the hydrogen evolution catalyst (HEC) in order to drive HER. In addition, following the Z-scheme of natural photosynthesis,[52] the CB edge of WOC must be negative of the VB edge of HEC, to ensure that electrons can transport from WOC to HEC.

Much work has been ongoing to develop robust, efficient photocathode materials to optimize the HER half of the PEC design without the use of noble metals like Pt. Many efficient single-phase catalysts have been developed, such as MoS_2,[53] CoS,[54] FeS_2,[55] Ni-Mo,[56] Ni-Sn,[57] etc. In addition to these catalysts, various homogenous catalysts have been utilized, such as cobaloximes,[58] Dubois-type nickel catalysts,[59] and Fe-porphyrins.[60] More closely aligned with the concept of a dual-light absorbing artificial photosynthetic device, dye-sensitized photocathodes have been developed that allow hole transfer from a photoexcited dye molecule to the VB of a p-type semiconductor. One example is p-type NiO sensitized with coumarin 343 molecular dye[61] or triphenylamine-perylenemonoimid donor-acceptor dye complexes.[62] Additionally, semiconductor-photosensitizer-HEC assemblies have been developed, such as NiO-coumarin 343-Fe complex by the

Hammarström group.[63] Additional photosensitizers are under development such as CdSe quantum dots[64] or CdSe/CdS assemblies.[65]

With the ability to tune two absorbers to perform their respective reactions, it is possible to drive the water splitting reaction without any electrochemical input, meaning that energy input is solely visible light. Some monolithic devices[44,66,67] have been developed using this scheme and such a device has been termed an artificial leaf by the Nocera group.[68] In the wireless configuration, these devices have reached an impressive solar-to-hydrogen efficiency of 3%, implying a bright future in artificial leaf devices. The forefront of such devices have been pushed even further by the Nocera group to couple the water splitting reaction with biological CO_2 reduction mechanisms to produce a system that exceeds the CO_2 reduction efficiency of natural photosynthesis.[69]

Evidently, momentum is building in the solar fuel materials field to identify and develop robust, low-cost, and efficient materials that can be applied to either the OER, HER, or further solar fuel reactions such as CO_2 reduction. As such, there is great need to both fundamentally understand existing materials, along with ways to tailor them to more efficiently perform their function, and to develop new classes of materials that represent the next generation of solar fuel materials. The following sections introduce two classes of materials that are currently under intense development in the field, namely a metal oxide OER photoanode material, $BiVO_4$, and zeolitic imidazolate frameworks, a subclass of metal organic framework (MOF) materials that are in the beginning stages of development to perform solar fuel producing reactions.

1.3 Bismuth Vanadate ($BiVO_4$) OER Photocatalysts

As suggested in the previous section, the replacement of TiO_2 within the PEC design with a semiconductor that absorbs visible light would be beneficial due to greater absorption of the solar spectrum. The ideal candidate would have this property, but also have comparable stability to TiO_2. The most promising candidate for this application is bismuth vanadate ($BiVO_4$), an n-type semiconductor that meets these criteria.[70-73]

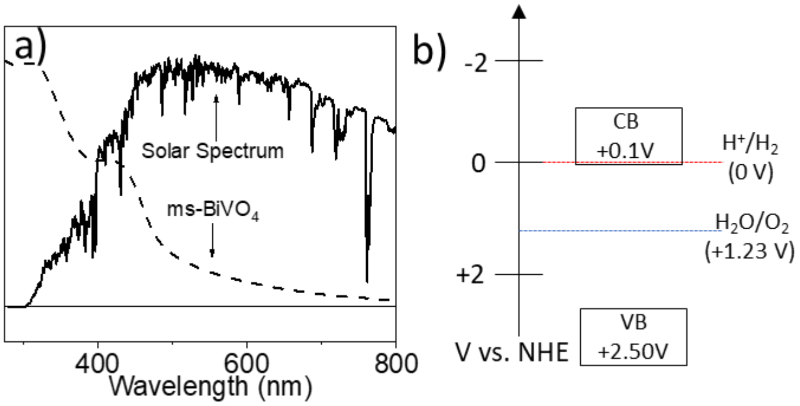

Figure 1.4. ASTM G173 solar spectrum and normalized ms-$BiVO_4$ UV-Visible absorption spectrum (a). Band diagram of ms-$BiVO_4$ vs. NHE (b).

The UV-Visible absorption spectrum of a particular phase of $BiVO_4$, monoclinic scheelite (ms-$BiVO_4$, Figure 1.4a) shows that the bandgap approaches 520nm (≈2.4eV) and overlaps with the blue-shoulder of the solar spectrum. While the majority of the solar spectrum is still not absorbed, the overlap is significantly better than that of TiO_2, which can only absorb light < 380nm. The band gap diagram (Figure 1.4b) shows that the VB edge is sufficiently positive for the OER half reaction to occur, but the CB edge is slightly too positive to perform HER. While water splitting can still be accomplished by applying a small positive potential to the $BiVO_4$ photoanode, the band alignment isn't ideal for this reason. However, the stability and performance of $BiVO_4$ have suggested that it is a very promising OER catalyst; much research is focused on improving the materials and engineering the band edges to better match the HER potential.[74] In discussing the properties of $BiVO_4$, the crystalline structure will first be outlined as it influences the light-absorbing properties and photocatalytic performance, after which some of the methods used to tailor the material to perform the OER efficiently are discussed.

Crystalline Phases of $BiVO_4$

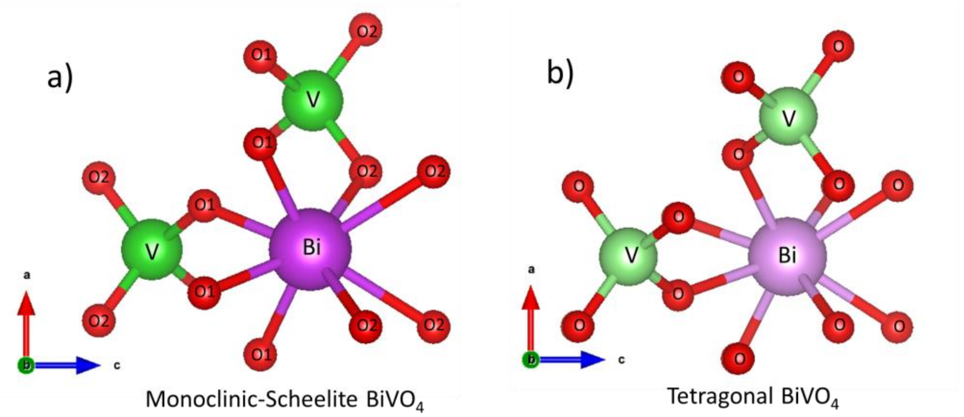

Monoclinic-Scheelite $BiVO_4$

Tetragonal $BiVO_4$

Figure 1.5. Monoclinic-Scheelite (a) and Tetragonal (b) structures of $BiVO_4$ viewed along the crystallographic b axis, using published crystal structures.[75]

The natural mineral of $BiVO_4$, pucherite, has an orthorhombic crystal structure in contrast with the monoclinic-scheelite or tetragonal phases adopted by synthesized samples.[76] In either phase, the oxidation states of Bi and V are +3 and +5, respectively. The phase depends on the synthetic conditions; the tetragonal (t-$BiVO_4$) phase is formed at higher temperature. These two phases are depicted in Figure 1.5 viewed along the crystallographic b axis. In the monoclinic-scheelite phase, the oxygen atoms are labeled as O_1 or O_2, depending on the Bi/V-O bond distance. Four distinct Bi-O bond distances are present (2.354 Å , 2.372 Å , 2.516 Å and 2.628 Å), in which the shorter two distances are represented by O_1 and the longer two distances as O_2. The distances between V and O are different as well, with V-O1 (1.69 Å) and V-O2 (1.77 Å). The tetragonal phase has only a single V-O distance (1.72 Å) and two similar Bi-O distances (2.453 Å and 2.499 Å). The structural differences outlined indicate that the Bi and V centers become more symmetric in the tetragonal phase, with loss of the repeating compressed, expanded, compressed etc. pattern along the crystallographic c axis. The impacts of the different structures on of $BiVO_4$ on its function will be examined by first comparing their electronic band edge structures and correlating it to the photocatalytic properties.

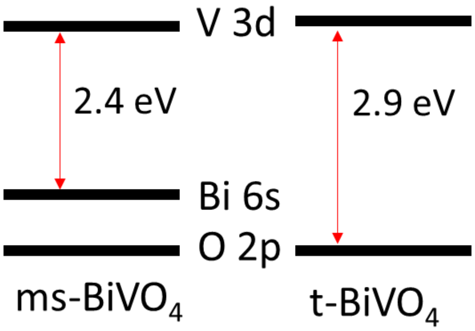

Figure 1.6. Simplified band edge electronic structure diagram for ms-$BiVO_4$ and t-$BiVO_4$.

The electronic band structures for the two phases of $BiVO_4$ are of interest because it is known that the tetragonal phase has a larger bandgap by its UV-Visible spectrum while ms-$BiVO_4$ exhibits a smaller bandgap and better visible light absorption.[77,78] This observation was supported by computational[79,80] and experimental[74,81] works that implicated a predominantly Bi 6s or hybridized Bi 6s/O 2p state at the valence band edge of ms-$BiVO_4$. Figure 1.6 shows the simplified band edge structure of each of the phases of $BiVO_4$. The conduction band edge is composed mostly of V 3d character for both phases. The valence band edge of the symmetric (about Bi and V), with respect to metal to oxygen distance, tetragonal phase is composed of O 2p character with no Bi character near the edge. Conversely, the structurally distorted monoclinic phase has the Bi 6S character due to stabilization of a Bi 6s lone pair that hybridizes with O 2p orbital.[82]

The smaller bandgap and thereby enhanced visible light absorption explain, in part, the superior activity for OER of the monoclinic phase[77,83] Thus, only the monoclinic phase will be discussed henceforth, and will be referred to as simply $BiVO_4$. With fundamental understanding of the material's structure, efforts are ongoing to improve the material. The most widely applied modification to $BiVO_4$ is doping, which will be introduced in respect to the deficiencies in the parent $BiVO_4$ material that it aims to correct.

$BiVO_4$ Doping Studies

Semiconductor doping is a widely-applied modification as very small dopant amounts (as small as 1 dopant atom for 10^9 atoms in the host lattice[84]) can impart changes in the host material, such as the majority carrier, band structure, photocatalytic activity, and carrier density and photodynamics. These effects have been extensively studied in more common semiconductors, such as TiO_2.[85-87] Since TiO_2 is n-type, it can be doped with electron-donating atoms to raise the fermi level. The increased fermi level manifests itself in enhancing the band-bending effect when in contact with an electrolyte, generating a larger electric field that enhances charge separation in the semiconductor and improves the interfacial charge-transfer events that define catalytic activity.

Within the bulk of the semiconductor, dopants can increase the carrier density and, thus, increase the carrier mobility. However, dopant atoms can also have negative effects on semiconductor performance, such as providing trap states in the band gap that lead to enhanced trap-mediated recombination of the electron-hole pair or decreased mobility of carriers after photoexcitation. If a state exists close to the valence band, then it is a hole trap; If it is located close to the conduction band then it will act as an electron trap. Another important distinction is the proximity to the CB or VB. If the trap state is close to the band, then it is a shallow trap state since small perturbations could result in the carrier becoming untrapped. If the trap state is located far away from the band (closer to the center of the bandgap), then it is a deep trap state from which the carrier is not easily removed. These traps can be conceptualized as a potential well due to the existence of new eigenstates after doping. The nature of the trap states introduced, however, is complex; it could be due to states of the dopant atom, distortions of the parent structure, surface states imparted by doping, etc. Therefore, it is important to systematically study the fundamental effects of each dopant on the properties of the parent material.

Table 1.1: Comparison of doping studies on $BiVO_4$ for OER. Citations: *a*[78], *b-d*[66], *e*[88], *f*[89], *g-i*[90],*j*[91],*k*[92],*l*[93]. Photocurrent comparisons were made at 1.0V vs. Ag/AgCl.

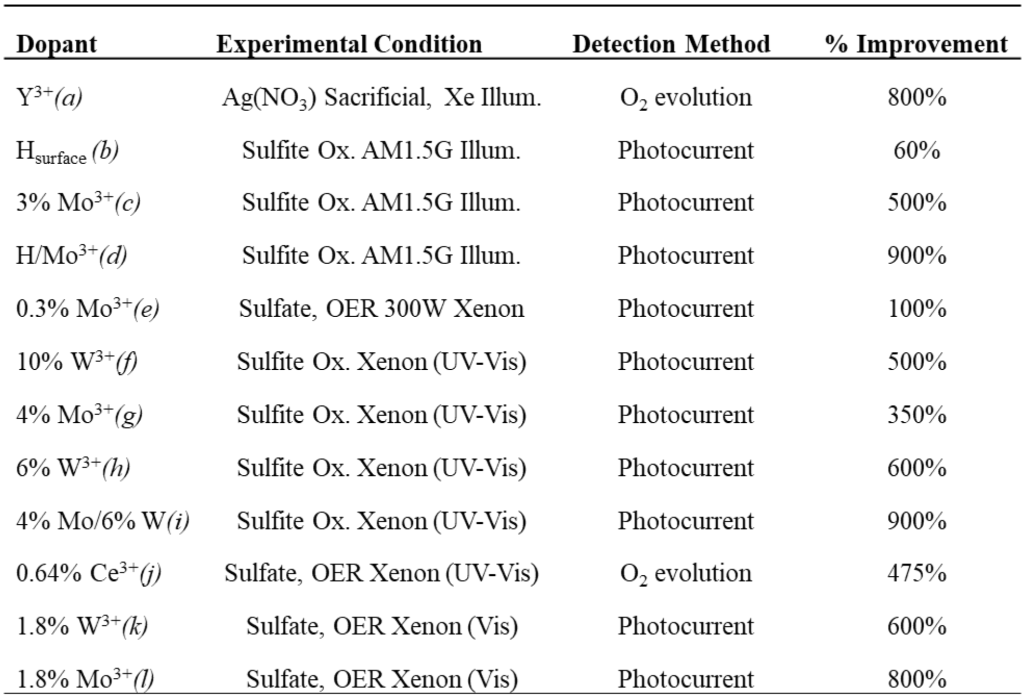

Dopant	Experimental Condition	Detection Method	% Improvement
Y^{3+}*(a)*	$Ag(NO_3)$ Sacrificial, Xe Illum.	O_2 evolution	800%
$H_{surface}$ *(b)*	Sulfite Ox. AM1.5G Illum.	Photocurrent	60%
3% Mo^{3+}*(c)*	Sulfite Ox. AM1.5G Illum.	Photocurrent	500%
H/Mo^{3+}*(d)*	Sulfite Ox. AM1.5G Illum.	Photocurrent	900%
0.3% Mo^{3+}*(e)*	Sulfate, OER 300W Xenon	Photocurrent	100%
10% W^{3+}*(f)*	Sulfite Ox. Xenon (UV-Vis)	Photocurrent	500%
4% Mo^{3+}*(g)*	Sulfite Ox. Xenon (UV-Vis)	Photocurrent	350%
6% W^{3+}*(h)*	Sulfite Ox. Xenon (UV-Vis)	Photocurrent	600%
4% Mo/6% W*(i)*	Sulfite Ox. Xenon (UV-Vis)	Photocurrent	900%
0.64% Ce^{3+}*(j)*	Sulfate, OER Xenon (UV-Vis)	O_2 evolution	475%
1.8% W^{3+}*(k)*	Sulfate, OER Xenon (Vis)	Photocurrent	600%
1.8% Mo^{3+}*(l)*	Sulfate, OER Xenon (Vis)	Photocurrent	800%

For $BiVO_4$, there is much interest in finding appropriate dopants to solve its shortcomings, namely its poor charge separation[94] and carrier mobility[89,90]. Many dopants have been attempted, with the highest photocurrents arising from W and Mo doping. Table 1.1 compares some publications and the % improvement that was observed from doping compared to the undoped $BiVO_4$ that they reported. It is immediately evident that different preparations were optimized with very different dopant concentrations by at%. The highest % improvement in this set of studies is 800% (our data, Mo/$BiVO_4$) for a singly-doped catalyst, with dual-doped catalysts at approx. 900%. Additionally complicating the comparison of these studies, however, is the experimental conditions. Many groups preferentially perform sulfite oxidation, a facile one electron oxidation that does not suffer from the kinetic issues that OER does. The photocurrent curves generated typically have much higher photocurrent with sulfite oxidation compared to OER for this reason, and have better fill factor. But, the photocurrents obtained are then incomparable to the real-world OER application. All of the above comparisons utilize Xenon lamps, but some are AM1.5G to simulate natural sunlight, some utilize the full Xenon UV-Vis spectrum, and others utilize only the visible spectrum (>400-420nm).

Due to the complications that arise from so many different experimental parameters for photoelectrocatalysis, it is difficult to effectively compare the performances of photoanodes across different studies. Additionally, there is a lack of fundamental studies that reveal the role that each dopant atom plays in the material. Without these fundamental studies in place, photoanodes will be optimized for the desired characteristic (likely photocurrent) without thorough understanding of how the material is being changed. Thus, there is a substantial need for fundamental studies that explore the structural and photodynamic nature of doped $BiVO_4$ materials.

The optimization of pristine $BiVO_4$ is presented in Chapter 3, where the optical, structural, and photocatalytic properties of the material are systematically studies by varying the thickness of the photoanode film. The trends observed highlight the limitations of pristine $BiVO_4$ and suggest that improving the photogenerated carrier mobility is key to improving the material. Following optimization of pristine $BiVO_4$, the material is doped with W, revealing altered photodynamics including electron-hole pair lifetime and carrier trapping. The structural and photodynamic changes explain the improved photocatalysis activity toward OER. Mo is then used as a dopant to determine if it can address some of the shortcomings of the W dopant, namely the distorted structure and limited mobility. By comparing the changes imparted due to Mo-doping and W-doping, it is confirmed that Mo is the superior single-dopant atom. However, as highlighted in Table 1.1, future state-of-the-art $BiVO_4$ materials might adopt a co-doping strategy to incorporate two or more different doping schemes. With the fundamental properties of W/$BiVO_4$ and Mo/$BiVO_4$ demonstrated herein, a clearer trajectory toward improving $BiVO_4$ photoanodes is provided.

1.4 Metal Organic Frameworks as Emerging Photocatalyst Materials

Metal organic frameworks (MOFs) are a class of porous materials constructed from metal or metal oxide nodes connected together by organic based linkers to form 3-dimensional structure. Due to the nature of their construction, it is possible to greatly tune the structure of MOFs by modifying the node structure, linker length, linker identity, etc.[95] This important property is inherent to the nature of their construction, which is based in the concept of reticular chemistry[96] that has been pioneered by Prof. Omar Yaghi in the past 20 years after his group's first report of microporosity in a MOF.[97] The concept of reticular chemistry is based on a class of materials having a periodic net that is formed from rigid molecular building blocks. The design principle maintains that, by using rigid molecular building blocks, pre-determined ordered structures will be formed, implying that the synthetic chemist can have near-complete control the structure of the product by controlling the structure of the starting materials, a level of control that is not possible in most classes of solid state materials beyond the molecular scale.[98]

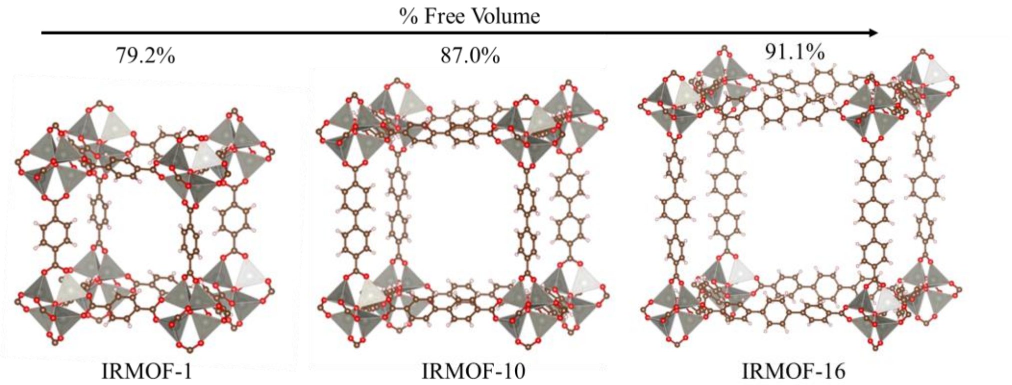

Figure 1.7. Isoreticular expansion of MOF-5 (IRMOF-1) performed by the Yaghi group. Structures were reproduced from the reported crystallographic data.[99]

Because of this property, MOF tunability is a very controllable design principle. For example, one can imagine extending the length of a given linker molecule in a MOF to put more space between the nodes, giving a larger cavity and larger pores. This process, called isoreticular expansion (i.e. expanding the structure without changing the net, or topology, of the MOF) was applied to a series of Zn MOFs based on the well-known MOF-5 structure (Zn and ditopic benzenedicarboxylate).[99] Figure 1.7. shows the expansion of the pores and cavity of MOF-5 (IRMOF-1) when longer linkers were used to form the MOF structure. The expansion of the structure is accompanied by an increase in the % free volume, or the space not occupied by atoms in the structure.

This example shows that one of the most important and tunable characteristics of MOF materials is their porosity, having up to >90% of their volume composed of free space and internal surface areas > 6,000 m^2/g.[100] Because of their massive surface areas, MOFs have been widely applied as gas adsorption materials.[101,102] Additionally, they have been widely applied as gas separation materials due to either molecular sieving with small pore size or due to different adsorbent-adsorbate interactions.[103] While adsorbent-adsorbate interaction mechanisms are less clear, there has been work, particularly by the Long group, on MOFs with open metal sites within porous channels that allow gas capture/separation by specific interactions with the substrate, affording selectivity.[104-106]

One of the most exciting emerging applications of MOFs is in heterogeneous catalysis.[107,108] Because of their porous structure, they have the ability to provide a tunable reaction environment, can provide selectivity to small molecular species based on pore size, and can incorporate familiar catalyst species into their cavities that cannot escape through the pores, termed nanoconfinement.[109] Additionally, catalyst species or photosensitizers can be incorporated into the framework by modification/substitution of the linkers or nodes, giving promising applications in heterogeneous photocatalysis.[110,111] Because of their heterogeneous nature while having the ability to incorporate single-site catalyst species, these types of MOFs represent a material that has both the advantages of homogeneous catalysis (high selectivity and catalysis efficiency) and heterogeneous catalysis (ease of separation and recyclability).

While MOF modifications and designs to impart photocatalysis activity are not the focus herein, they represent a rapidly developing facet of the solar fuels fields, as numerous systems have been developed related to the water splitting reaction.[112] One of the common drawbacks of MOF materials, however, is their chemical and thermal stability. Therefore, an optimum MOF catalyst material would be part of a class of MOF materials that are tunable, stable, and constructed from low-cost materials, such as zeolitic imidazolate frameworks.

Zeolitic Imidazolate Frameworks

Zeolitic Imidazolate Frameworks (ZIFs), a subclass of MOFs, are named for their structural homology with traditional zeolites (metal-imidazole-metal bond angle of 145° like Si-O-Si angle in zeolites).[113] There are various topologies that ZIFs adopt, depending on their compositions, with pore apertures ranging from 0.7-13.1 Å and cavity size ranging from 0.7-16.5 Å. For ZIFs, the metal node is a transition metal ion (Co^{II} and Zn^{II}, most commonly) and the ligand is imidazolate (deprotonated imidazole) with or without various functional group modifications. The overall chemical formula of ZIF is $M(IM)_2$, where M represents a metal ion in the +2 oxidation state and IM represents imidazolate, with +1 charge. Therefore, the ZIF structure has an overall neutral charge.

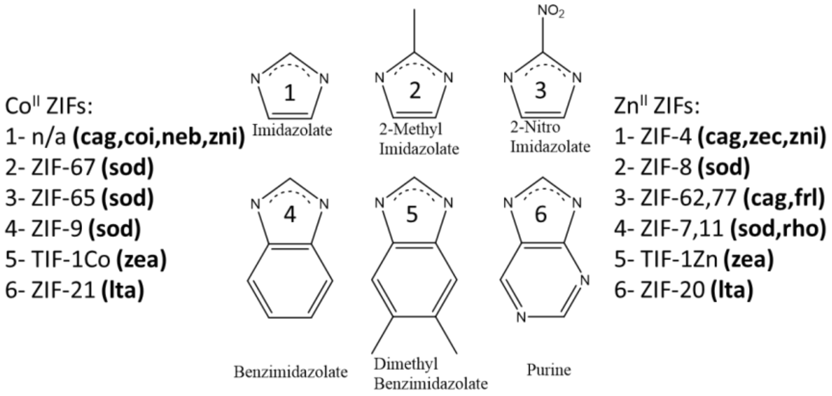

Figure 1.8. Representative ligands used in ZIF synthesis and their corresponding Co^{II} (left) and Zn^{II} (right) names and possible topologies.

There are various imidazolate linkers that have been used in ZIF synthesis[114] (Figure 1.8). In general, similar structures can be obtained utilizing either Co^{II} or Zn^{II} metal nodes, with various possible topologies especially for the least derivatized imidazolate unit. For the more complex imidazolate units, there are typically a smaller distribution of possible topologies, which supports the observation that ZIF topology is largely ligand-directed with only weak dependence on metal node identity. It has been proposed that linker-linker interactions are responsible for this dependence, which is more evident for the bulky and highly-conjugated benzimidazolate-based derivatives. Because of the structural tunability of ZIFs, like other MOFs, they have widely-varying pore sizes and surface areas that largely affects their most-researched application of gas separation and storage.[114]

The inherent tunability of ZIF structures, together with their excellent chemical and thermal stability[115], positions them as a possible candidate for heterogeneous catalysis reactions. Indeed, many exploratory works have been reported, such as ZIF-9 as a catalyst for the Knoevenagel reaction[116], ZIF-8 as a catalyst for styrene carbonate synthesis,[117] conversion of CO_2 to chloropropene carbonate,[118] and Friedel-Crafts acylation,[119] and yolk-shell ZIF-8 nanostructures as a size-selective catalyst for small molecules, namely ethylene and cyclohexene, hydrogenation.[120]

Driven by the need to reduce global dependence on fossil fuels, there has been a focus on applying ZIF-based catalysts to photocatalytic reactions. One type of reaction that has been focused on is the degradation of environmental pollutants, which is often studied by the degradation of organic dye molecules that can be monitored easily by UV/Visible spectroscopy. In one example, ZIF-8 with deposited Pt was grown onto TiO_2 nanotubes, where it was observed that ZIF-8/Pt had enhanced phenol photodegradation in comparison to Pt/TiO_2.[121] In another example, cationic dye methylene blue (MB^+) was degraded using pure ZIF-8 under UV-radiation, which generated degradative hydroxyl radicals.[122] It was also shown that TiO_2 nanoparticles could be encapsulated within the ZIF-8 framework, which led to an 8x increase in MB^+ and rhodamine B photodegradation activity compared to TiO_2 NPs alone.[123] Another recent study applied ZIF-8 as a size-screening layer over ZnO to selectively adsorb and photoreduce Cr(VI), which is small enough to permeate a ZIF-8 layer, compared to a larger organic dye molecule.[124] A recent visible-light driven system to degrade rhodamine B was developed by self-assembly of ZIF-8 around light absorbing Bi_2S_3 nanorods, greatly increasing the dye degradation activity.[125]

The application of ZIF photocatalysts has also been extended into the realm of solar-fuels producing photocatalytic reactions, more closely aligning them among the possible materials to develop into PEC technologies. To date, the most studied application of ZIFs in this area has been their application to CO_2 reduction. The experimental work has been largely performed by Xinchen Wang's group using Co^{2+}-based ZIF-9. Through multiple studies, it was found that a series of different photosensitizer materials could be used to harvest light and, using ZIF-9 as a co-catalyst, reduce CO_2 to CO with some selectivity over the competitive HER using organic solvents and triethanolamine electron donor. Using CdS as a photosensitizer, an apparent quantum yield of 1.93% was achieved for reduction of CO_2 to CO.[126] Using $[Ru(bpy)_3]^{2+}$ as a photosensitizer in a similar system, an apparent quantum yield of 1.48% was reached.[127] With the organic semiconductor carbon nitride g-C_3N_4 that contains no noble metals, an apparent quantum yield of 0.9% was realized.[128] Through these reactions, it was suggested that ZIF-9 benzimidazolate linkers provide a reaction environment to promote CO_2 adsorption and transformation, however another comparative study suggests that the metal ion also plays a role. By replacing Co^{2+} in ZIF-67 with Zn^{2+} (ZIF-8), the reaction yield decreased by over an order of magnitude, suggesting that the open-shell Co^{2+} metal center plays a role in the reaction.[129] The exact contribution of ZIF to CO_2 reduction, however, is poorly understood.

Prospects for ZIFs in Solar Fuel Catalysis

In nearly all of these examples, ZIF plays the role as either an inert host for catalytic species or has an indefinite role during the photocatalytic process. Evidently, there is not a clear understanding of the roles that ZIFs might play as potential photocatalyst materials. While many applications have already been found, their continued development is largely hampered by a lack of fundamental understanding of their photodynamic and photocatalytic properties. The work herein aims to relieve this deficiency by utilizing steady-state and time-resolved spectroscopic tools to investigate the roles of ZIF materials as prospective solar fuels catalysts and to explore some examples of photocatalytic applications.

In Chapter 4, the intrinsic photochemical response of a Co^{2+} based ZIF, ZIF-67, is investigated using time-resolved optical and X-ray absorption spectroscopies, revealing a long-lived charge-separated state with LMCT character. Because the nature of charge separation in the material is rather unclear, a second study focuses on the mechanism of charge separation in the material. By doping ZIF-67 with different metals, namely closed shell Zn^{2+} and open shell Cu^{2+}, it was demonstrated using time-resolved optical and element-specific time resolved X-ray absorption spectroscopy that a shift in electron density between metals of different identity is observed, strongly indicating a metal-to-metal charge transfer mechanism. In both of these fundamental photodynamic studies, a clear promise for ZIF-67 and other ZIF materials is suggested in regard to their photocatalysis applications. To demonstrate application of this charge separated state with LMCT character toward interfacial electron transfer, an important prerequisite to photoredox catalysis, a study was performed in which molecular dye methylene blue (MB^+) was photoreduced after selective excitation of ZIF-67 Co^{2+} d-d transitions. This result showed, for the first time, that photoinduced interfacial charge separation can be achieved in ZIF materials, a crucial characteristic of a heterogeneous photocatalyst material. These studies highlight the great promise of ZIF materials in photocatalysis and guide the development of the next generation of ZIF-based photocatalytic system.

Following the fundamental photodynamic studies, the photocatalytic applications of ZIF-67 are investigated in Chapter 5. As suggested by the somewhat low selectivity for CO_2 reduction over the competing HER,[126-128] ZIF-67 was investigated as an HER photocatalyst. While direct excitation of ZIF-67 with TEOA electron donor did not produce product, it was found that addition of $[Ru(bpy)_3]^{2+}$ photosensitizer led to efficient HER. Unlike the previous studies, the role of ZIF was systematically investigated by optical transient absorption spectroscopy, demonstrating charge transfer from $[Ru(bpy)_3]^{2+}$ to ZIF-67, and by *in situ* X-ray absorption spectroscopy, revealing a key reaction intermediate and allowing the proposal of a reaction mechanism.

Chapter 2

EXPERIMENTAL METHODS

2.1 Experimental for Chapter 3

Materials

Bismuth(III) nitrate ($Bi(NO_3)_3 \cdot 5H_2O$) was purchased from Ward's Science (Rochester, NY) and vanadyl(IV) acetylacetonate ($C_{10}H_{14}O_5V$) was purchased from Acros Organics (Geel, Belgium). Ammonium metatungstate hydrate ($(NH_4)6H_2W_{12}O_{40} \cdot XH_2O$) was obtained from Strem Chemicals (Newburyport, MA) and ammonium molybdate tetrahydrate ($(NH_4)_6Mo_7O_{24} \cdot 4H_2O$) was obtained from Electron Microscopy Science (Hatfield, PA). Acetic acid (≥99.7%) from SigmaAldrich (Milwaukee, WI) and acetylacetone (>99.0%) from TCI America (Portland, OR) were used. Sodium sulfate ($NaSO_4$) and sodium sulfite (Na_2SO_3) were obtained from Ward's Science. Fluorine-doped tin oxide (FTO) glass (2 mm thick) was purchased from Solaronix (Aubonne, Switzerland) and cut to 1.25 × 2.50 cm dimensions for electrode fabrication. Aqueous solutions were prepared from highly polished deionized H_2O showing >16 MΩ-cm resistivity. Nitric acid from Sigma-Aldrich and hydrogen peroxide (30%) from J.T. Baker (Avantor Materials, Center Valley, PA) were used to make piranha glass-etching solution.

Synthesis of $BiVO_4$ Thin Films and Photoanodes

$BiVO_4$ films were prepared by an organic deposition method.[130] The Bi and V precursors (1:1 molar ratio) were dissolved in acetic acid (4 equivalents) and acetylacetone (1equivalent), respectively by sonication. Then, the two solutions were mixed and sonicated to make a 0.05 M BiVO4 stock solution with respect to Bi and V. The stock solution was then diluted to 0.04M. Films were prepared by drop-coating 25µL of 0.04M precursor onto a piranha-etched quartz substrate for optical studies or onto cleaned FTO slides for photoanodes. The photoanodes had the top 3mm of the film masked using scotch tape during the drop-coating step to give area for electrical connection. The drop-coating was allowed to dry for 30 minutes in air and then the films were calcined in air at 450˚C for 90 minutes to form $BiVO_4$ from the amorphous precursor films.

Thickness Dependence Study Films Preparation

Following the above procedure, the $BiVO_4$ precursor solution was instead prepared at 0.08 M and either used directly to prepare samples, or diluted to 0.04 M, 0.02 M, or 0.01 M using acetylacetone.

$W/BiVO_4$ and $Mo/BiVO_4$ Preparation

For $W/BiVO_4$ and $Mo/BiVO_4$ films, the initial volume of acetic acid was reduced to incorporate a given amount of 0.04 mM dopant dissolved in acetic acid using sonication. The final concentration was diluted to 0.04 M with respect to Bi and V atoms, as in undoped films. Drop-coated films were calcined in air at 450˚C for 90 minutes.

Standard Characterization

Steady-state UV-Visible spectra were collected using an HP Agilent 8453 spectrometer. Powder X-ray diffraction (pXRD) was performed using a Rigaku Miniflex II XRD diffractometer (Cu Kα). For thickness dependence studies, XRD patterns were collected directly from thin films on quartz substrate. For doping studies, the film was removed from multiple samples and ground in methanol for 10 minutes, then dried in air before pXRD characterization. Scanning electron microscopy was performed with a JEOL JSM-6510LV operating in secondary electron mode. Representative images of each sample studied are shown in Figure 2.17.

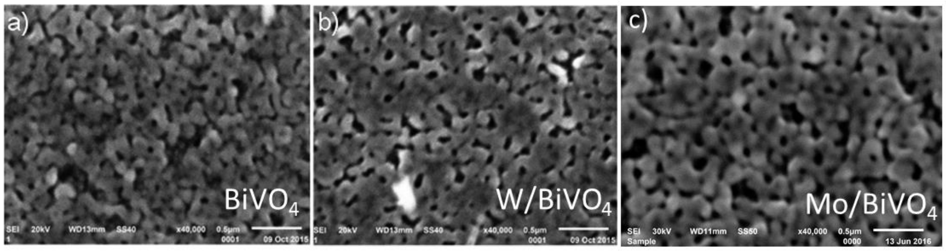

Figure 2.1. SEM images of (a) $BiVO_4$, (b) 1.8 at% W/$BiVO_4$, and (c) 1.8 at% Mo/$BiVO_4$.

Femtosecond Transient Absorption Spectroscopy (OTA)

The pump-probe TA spectroscopy utilizes a regenerative amplified Ti-Sapphire laser system (Spectra Physics Solstice, 800nm, <100 fs fwhm, 3.5 mJ/pulse, 1kHz repetition rate). Tunable pump energies are generated in TOPAS to generate wavelengths ranging from 250 to >2,000 nm. The UV-Visible probe pulse supercontinuum was generated in a translated CaF_2 window (330-720 nm). Measurements were performed in a Helios ultrafast spectrometer (Ultrafast Systems LLC). The energy of 315nm pump pulses used for all measurements were 0.35 μJ. Thin films were continuously translated to avoid sample degradation.

Photoelectrochemical (PEC) Measurements

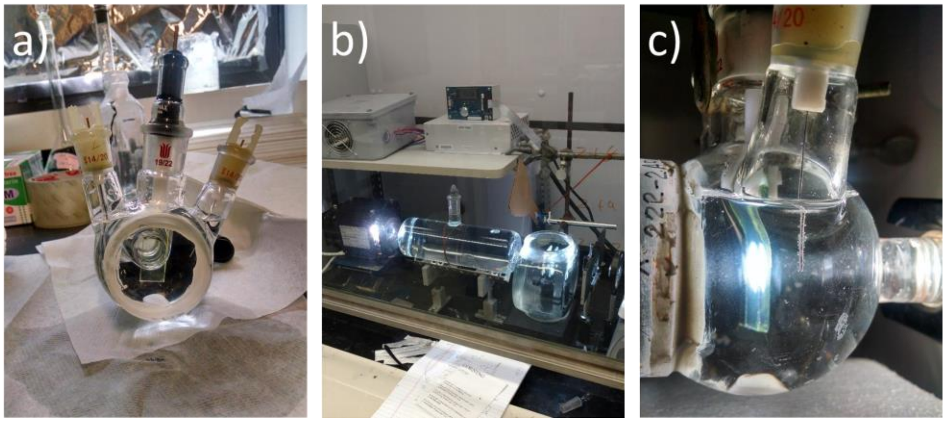

Figure 2.2. Image of the as-assembled PEC cell (a) with Ag/AgCl (3M NaOH) reference electrode on left, $BiVO_4$ working electrode (middle, centered in quartz illumination window) and Pt wire counter electrode on right. The quartz window is attached to the cell using Loctite Hysol epoxy. The Xenon path (b) consists of a 1 foot long water filter to remove IR irradiation, then passed through an additional IR filter and 400nm long-pass filter. The Xenon irradiation is then passed through an aperture to block any unfiltered light and is then focused onto the film using a lens (c).

The PEC experiments were performed at room temperature in a home-made three-electrode cell equipped with flat quartz window for photoanode illumination (Figure 2.18) with description of the Xenon setup in the figure description. The as-prepared $BiVO_4$ films on FTO were used at working electrodes in N_2 purged 0.1M Na_2SO_4 electrolyte at PH 7. The filtered Xenon lamp has a 310 mW/cm^{-2} power density at the sample. The linear sweep voltammetry curves (J-V curves) were recorded at 25 mV/s scan rate. The working electrode is in a glass joint that allows rotation for either front- or rear-illumination geometries.

X-ray Absorption Spectroscopy

XAS measurements were performed at the beamline 12BM of the Advanced Photon Source at Argonne National Laboratory. The spectra were collected at room temperature by fluorescence mode using a 13-element geranium solid state detector. One ion chamber is placed before the sample and used as the incident X-ray flux reference signal. There are two ion chambers after the sample; between the two chambers a metal foil reference (Pt, V) is placed and used for energy calibration.

2.2 Experimental for Chapter 4

Materials

Methanol (Certified ACS, > 99.8%) was purchased from Fisher Chemical and 2-methylimidazole ($C_4H_6N_2$, 97%) was purchased from Alfa Aesar. Cobalt Nitrate Hexahydrate ($Co(NO_3)_2{\cdot}6H_2O$, 99%) was obtained from Acros Organics. For piranha etching, Nitric Acid from Sigma-Aldrich and hydrogen peroxide (30%) from J.T. Baker was used. Quartz substrate (3”x1”, 1mm thick) was purchased from Ted Pella Inc. Copper nitrate trihydrate ($Cu(NO_3)_2{\cdot}3H_2O$, 99%) was purchased from Acros Organics and Zinc nitrate ($Zn(NO_3)_2{\cdot}6H_2O$, 99%) was purchased from Alfa Aesar.

The synthesis of ZIF-67 thin film

Following the published procedure, two precursor solutions were individually prepared in 50mL portions of methanol (0.73g $Co(NO_3)_2{\cdot}{}_6H2O$ and 1.65g 2-methylimidazole). To prepare ZIF-67, equal portions of the precursor solutions were mixed and allowed to precipitate at room temperature for 1 hour. For a typical thin film preparation, piranha-etched substrate was quickly immersed into freshly-prepared precursor mixture at a volume of 6 mL. As ZIF-67 precipitated in solution, it formed directly on the substrate to make a single ZIF-67 layer. This process was repeated a total of 3 times, rinsing the film with ethanol in-between the 1 hour growth periods.

After, the film was allowed to dry in air before characterization. For ZIF-67 suspension, the previous steps were repeated at larger volume in the absence of a substrate. The precipitated ZIF-67 was washed thoroughly with methanol via centrifugation to remove excess ligand and supernatant species. The precipitate was then resuspended in methanol without being allowed to dry to preserve particle size.

Dimethylimidazole-Co Coordination Complex

Dimethylimidazole-Co complex was prepared in 5mL volume of methanol by mixing 2.5mL of 0.08M $Co(NO_3)_2 \cdot 6H_2O$ with 2.5mL of 0.8M 1,2 dimethylimidazole. The solution instantly becomes a purple color when the ligand coordinates to Co. This solution was used directly for optical characterizations.

Mixed-Metal ZIF Synthesis

Co:Zn mixed metal ZIFs were prepared following the same method as ZIF-67 suspension, except some of the Co was substituted with Zn in order to maintain the same metal to 2-methylimidazole ratio.

CuZIF samples were prepared following an aqueous synthesis procedure using highly concentrated ligand. CuZIF-67 was prepared by dissolving 7g of 2-methylimidazole in 30mL of deionized water to make the first solution; 0.45g of $Co(NO_3)_2·6H_2O$ and 0.45g of $Cu(NO_3)_2·3H_2O$ were dissolved in 10mL of deionized water to make the second solution. The two solutions were sonicated separately to fully dissolve the precursors, and then the two solutions were mixed in a 50mL centrifuge tube and shaken for 20 seconds. After 30 minutes was allowed for ZIF growth, the solid precipitate was collected via centrifugation and washed several times with methanol. CuZIF-8 was prepared using the same procedure, except $Co(NO_3)_2·6H_2O$ was substituted by $Zn(NO_3)_2·6H_2O$ and the amount of 2-methylimidazole was increased to 9g.

MB^+-ZIF-67 Synthesis

MB^+-ZIF-67 was prepared by soaking the ZIF-67 film in a 0.1M methanol solution of MB^+ (Acros Organics, Geel, Belgium) for 15 minutes. The film was then removed from solution and allowed to dry. The control sample, MB^+-Quartz was synthesized by spin-coating a 0.1 M solution of MB^+ in methanol onto an etched quartz substrate until a comparable optical density to MB^+-ZIF-67 was obtained.

Standard characterization

X-ray diffraction (XRD) was performed using a Rigaku Miniflex II XRD diffractometer with Cu Kα radiation. Powder samples were prepared by dropping sonicated ZIF-67 precipitate samples onto a frosted glass sample plate and allowing time for methanol solvent to evaporate. Film samples on quartz substrate were directly measured using a film sample holder. Steady state UV−visible measurements were taken on a Cary 5000 UV-Vis-NIR spectrophotometer with as-prepared film samples on quartz substrate. Powder reflective spectra were recorded on the same spectrometer with internal diffuse reflectance attachment.

Atomic Force Microscopy (AFM)

Surface morphology of the thin film was characterized by a Bruker Dimension ICON AFM (Bruker, Santa Barbara), where PeakForce Quantitative Nano Mechanical (PF-QNM) mode is used. In this mode, the probe is modulated at a low, off-resonance frequency of 2 kHz and at an amplitude of 150 nm. The feedback signal is the maximum force, or Peak Force, between the tip and the sample at every tapping cycle. ScanAsyst-Air probe (Bruker, Santa Barbara) with a nominal spring constant of 0.4 N/m and tip radius of 2 nm was used. The peak force or imaging force was typically 1~3 nN. AFM images were processed by Nanoscope Analysis Software (Bruker, Santa Barbara).

Femtosecond optical transient absorption (OTA) spectroscopy

The femtosecond TA experiments were performed on the setup described in section 2.1 with the following specifications. Sapphire was used to generate the white light continuum in the wavelength range of 420 nm–780 nm. The energy of 400 nm, 530 nm and 1000 nm pump pulses were 1.0, 0.75, and 1.5 μJ, respectively. MB^+-ZIF-67 experiments were performed with the same setup using 1000nm excitation pulses with 4.6 μJ/pulse.

Nanosecond optical transient absorption spectroscopy

Nanosecond OTA measurements were carried out at Center of Nanoscale Materials of Argonne National Laboratory. The pump pulse is generated from a regenerative amplified Ti:Sapphire laser system (Newport Spectra-Physics Spitfire Pro, 1.67 kHz repetition rate and 120 fs pulse) equipped with TOPAS. The probe was based on an EOS fiber laser continuum and measured by an Ultrafast System EOS spectrometer. The same excitation pump fluences were used from the femtosecond experiments.

Steady State X-ray Absorption (XAS) spectroscopy

Steady state XAS measurements were performed using the same setup described in section 2.1, except Co reference foil was used for energy calibration.

X-ray transient absorption (XTA) spectroscopy

XTA was performed at beamline 11 ID-D, Advanced Photon Source (APS) at Argonne National Laboratory. The laser pump was based on a Nd:YLF regenerative amplified laser (1054nm, 1.6 kHz repetition rate, 5 ps FWHM). The X-ray pulse with 80 ps FWHM width at 6.5 MHz repetition rate was used as the probe. The laser pump and X-ray probe intersect at a flowing sample stream with 550 μm in diameter. The X-ray fluorescence signals were collected at 90˚ angle on both sides of the incident X-ray beam by two avalanche photodiodes (APDs). A soller slits/Fe filter combination, which was custom-designed for the specific sample chamber configuration and the distance between the sample and the detector, was inserted between the sample stream and the APD detectors. The emitted Co or Cu X-ray fluorescence collected at the specified delay time after the laser pump pulse excitation of ZIF was used to build the laser-on spectrum in APS standard operation mode. The Co or Cu fluorescence resulting from averaging the previous 50 round trips in the storage ring prior to the laser pulse were used to construct the ground state spectrum of ZIF.

2.3 Experimental for Chapter 5

$[Ru(bpy)_3]^{2+}$ Synthesis.

$[Ru(bpy)_3]^{2+}$ was synthesized following the published literature procedure.[131] Commercial $RuCl_3 \cdot H_2O$ was dried in an oven at 120° C for 3 hours. Dried $RuCl_3$ (0.4 g, 1.93 mmol), 2,2’-bipyridine (0.9 g, 5.76 mmol), and water were placed in a 100 mL flask fitted with a reflux condenser. Sodium phosphinate was prepared by adding NaOH to 31% phosphinic acid until slightly cloudy precipitate is obtained, then re-adding phosphinic acid dropwise until the precipitate redissolves. Then, 2 mL of sodium phosphinate was added and the mixture was refluxed for 30 minutes. During reflux, the initial green solution changes color to brown and finally orange. The solution was filtered to remove traces of undissolved material, and then the crude product was precipitated by the addition of potassium chloride (12.6 g) to the filtrate. The solution and solid were then refluxed to give a deep red solution which, upon cooling to room temperature, yields brilliant red-orange crystals. The crystals were filtered, washed with ice-cold 10% aqueous acetone (2x5mL) and acetone (30 mL), and then air-dried.

Photocatalytic HER Experiments.

HER photocatalysis was performed in glass vials of 9 mL volume with rubber septa. The stirred, N2 purged vials were irradiated with 450 nm LEDs at various power outputs, where the optimized power was 1.02 mW. The 400 μL Headspace samples were analyzed for H2 concentration by an Agilent 490 micro gas chromatograph with 5 Å molecular sieve column.

Standard Characterization.

UV-Visible measurements and diffuse reflectance measurements were performed on a Cary 5000 UV-VIS-NIR spectrophotometer with internal diffuse reflectance accessory. The XRD patterns were performed using a Rigaku Miniflex II XRD diffractometer with Cu Kα radiation. Emission spectrum of $[Ru(bpy)_3]^{2+}$ in acetonitrile (ACN) was collected using a PTI QM40 spectrometer. Surface morphology of the thin film was characterized by a Bruker Dimension ICON AFM (Bruker, Santa Barbara).

Femtosecond Optical Transient Absorption (fs-OTA) Spectroscopy.

The femtosecond TA experiments were performed on the setup described in section 2.1 with the following specifications. The 410 nm pump pulses were used to excite the sample (0.75 μJ/pulse). The sample preparation for OTA in HER photocatalysis section was performed by immersing either a ZIF-67 (see ZIF-67 synthesis section) or Al_2O_3 film (prepared as in our previous work)[132] in a 0.1M ethanolic solution of $[Ru(bpy)_3]^{2+}$ for 30 minutes. The as-prepared film was then dried in air and used for OTA measurement. The 410 nm pump wavelength was chosen to selectively excite

$[Ru(bpy)_3]^{2+}$, as neither bare ZIF-67 nor Al_2O_3 gives transient signal under 410 nm excitation.

Nanosecond Optical Transient Absorption (ns-OTA) Spectroscopy.

The ns-OTA measurements were performed using the same setup described in section 2.2. The same sample preparation as in fs-OTA was followed.

In Situ X-ray Absorption Spectroscopy (XAS).

In Situ XAS was performed at beamline 12-BM at APS. The 3 mL catalysis mixture was sealed and N2 purged in a custom Teflon cell with Kapton front window for X-ray irradiation and fluorescence emission and quartz rear window for photoirradiation. The X-ray fluorescence was detected by a Canberra 13-element geranium solid-state detector and the cell was irradiated from the rear window by the 450 nm LED at 1.02 mW power. The conditions for the *in situ* experiment were 1.25 M of TEOA, 4.5x10-4 M of $[Ru(bpy)_3]^{2+}$, and 1.67 g/L ZIF-67 at a 3 mL reaction volume in acetonitrile with 5 mL headspace.

Chapter 3

PHOTOPHYSICAL AND PHOTOCATALYTIC PROPERTIES OF BIVO$_4$ PHOTOANODES

While BiVO$_4$ is a promising photoanode material for OER due to its narrow bandgap and appropriate valence band edge for OER,[74,79,133] it suffers from poor charge separation,[73,134] low photogenerated carrier mobility,[135] and slow OER kinetics.[136] Often, the issues of charge separation and photogenerated carrier mobility are attributed to irregularities in the crystalline structure of a semiconductor material. These irregularities are often trap states that are formed either in the bulk of the material or at surface states. In order to improve BiVO$_4$ materials, it remains important to make a distinction between bulk states that serve the role of providing charge migration channels and surface states that perform OER and assist in interfacial electron transfer in order to understand how each contributes to the overall photocatalysis efficiency in a PEC. Once the contribution of each is well understood, then improvement methods can be precisely targeted to either the surface or the bulk of the material.

Due to the termination of the crystalline structure at the surface, it is common for semiconducting materials to develop defect states due to structural or coordination differences from the bulk crystalline structure.[137,138] These defect states often lie within the bandgap of semiconductors and represent new states that can be populated by electrons or holes, causing irregularities in the carrier migration energetics, often limiting photogenerated carrier mobility. These defect states, termed trap states, can also serve as recombination centers due to the reduced carrier mobility; photogenerated electrons and holes are unable to separate efficiently if a trapping process dominates. The carrier trapping process typically occurs on a femtosecond to picosecond timescale[139-141] before either performing their respective redox chemistries or recombining.

Doping with ions is one desirable approach to resolve poor carrier transport properties, which caused extensive carrier accumulation and recombination. Recent studies have shown that $BiVO_4$ doped with electron donor ions, such as W or Mo, have increased electrical conductivity and photocurrent for OER.[94,142-144] However, as suggested by the modest improvement of charge separation efficiency, doping can raise other issues that counteract the enhanced carrier transport. For example, the incorporation of dopants can introduce trap states which often serve as recombination centers and hinder interfacial charge separation.[145] Doping can also decrease the width of the depletion layer and thus enhance carrier recombination.[146] Therefore, careful fundamental studies of the fundamental photodynamics and the effect of dopant atoms are required.

3.1 Implicating the Contributions of Surface and Bulk States on Carrier Trapping and Photocurrent Performance of $BiVO_4$ Photoanodes

Introduction

In this study, the thickness of $BiVO_4$ films was varied such that spectroscopic investigations into their properties revealed thickness-dependent trends. Thicker films contain more bulk material than thin films, revealing information about both bulk and surface states using optical transient absorption spectroscopy (OTA), X-ray absorption spectroscopy (XAS), and photoelectrochemical cell (PEC) studies. Using this methodology, it is determined that the bulk and surface states both contribute to the poor performance of $BiVO_4$ photoanodes.

Results and Discussion

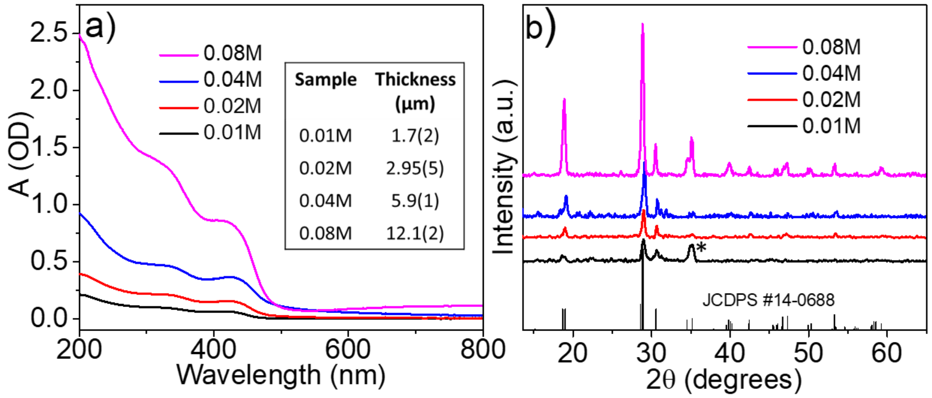

Figure 3.1. UV-Visible spectra (a) and pXRD patterns (b) of $BiVO_4$ prepared at varying thicknesses. The thicknesses at each concentration are displayed in the inset of (a) and were determined by cross-sectional SEM. The asterisk for 0.01M sample in (b) indicates that preferred orientation was observed, likely at the substrate-$BiVO_4$ interface.

$BiVO_4$ was prepared using the published organic deposition method from a 1:1 molar ratio of vanadyl-(IV) acetylacetonate and bismuth(III) nitrate in acetylacetone/acetic acid solvent.[130] Thin films were drop-coated onto quartz substrates of the same size using the same volume of precursor at varying concentrations, namely 0.1M, 0.2M, 0.4M, and 0.8M. Henceforth, the samples are referred to by their precursor concentration and their thicknesses are given in the inset of Figure 3.1a. After calcination at 450˚C for 90 min, the transparent brown-teal colored film becomes a transparent yellow film which was confirmed to be of the monoclinic scheelite phase (JCDPS card # 14-0688) via pXRD (Figure 3.1b) due to the splitting of the diffraction peaks at 19˚ and 35˚ 2θ.[77,78,83] The UV-Visible spectra in Figure 3.1a show that all samples share a similar peak profile with an absorption edge at approximately 520nm, consistent with the monoclinic scheelite phase.[147]

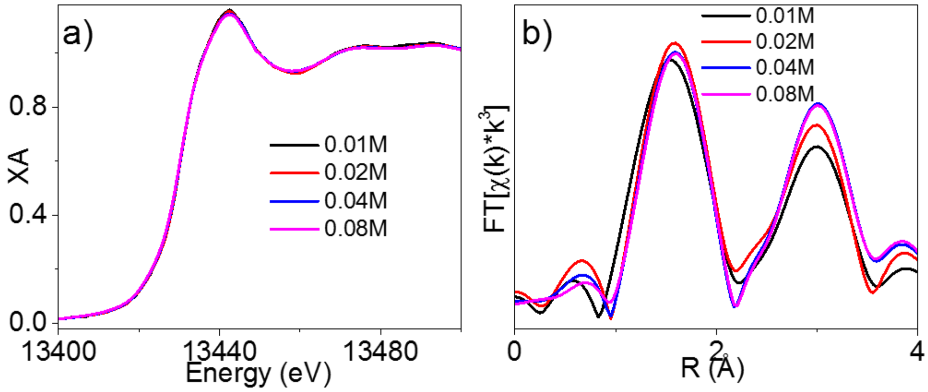

Figure 3.2. Bi L_3 edge XAS spectra in the XANES region (a) and Fourier-transformed EXAFS spectra in R-space (b).

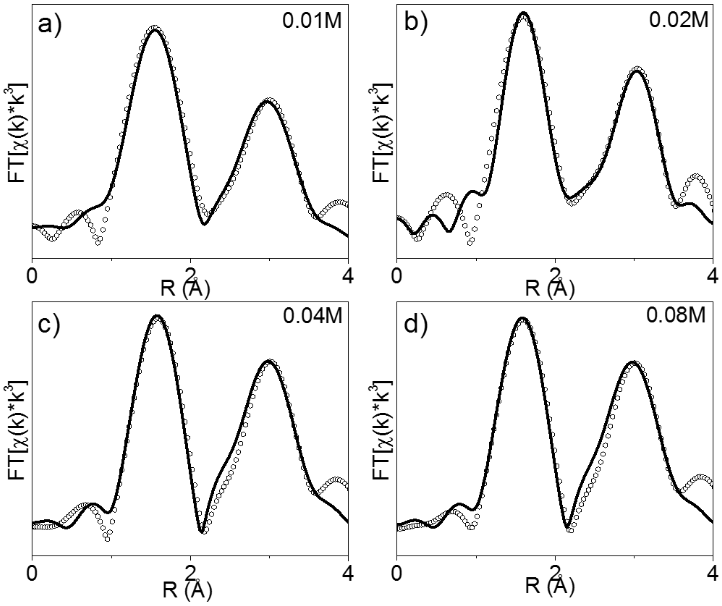

Figure 3.3. EXAFS data in R-space for Bi L_3 edge with data as open points and FEFF best fit lines.

Table 3.1. EXAFS Fitting parameters for Bi L_3 edge and V K-edge with vector distances (R±0.02 Å).

Vector	**N**	**0.01M**		**0.02M**		**0.04M**		**0.08M**	
		R (Å)	**σ^2 (Å^2)**	**R (Å)**	**σ^2 (Å^2)**	**R (Å)**	**σ^2 (Å^2)**	**R (Å)**	**σ^2 (Å^2)**
Bi-O_1	4	2.24	0.010	2.29	0.009	2.29	0.007	2.29	0.007
Bi-O_2	2	2.42	0.010	2.51	0.006	2.51	0.006	2.51	0.006
Bi-O_2	2	2.53	0.015	2.62	0.022	2.62	0.018	2.62	0.022
Bi-V	2	3.56	0.007	3.58	0.007	3.58	0.004	3.58	0.004
Bi-V	2	3.69	0.007	3.72	0.007	3.72	0.004	3.72	0.004
Bi-Bi	2	3.42	0.020	3.62	0.012	3.62	0.018	3.62	0.017
V-O_1	2	-	-	1.68	0.001	1.68	0.002	1.68	0.006
V-O_2	2	-	-	1.75	0.0005	1.75	0.001	1.75	0.001

While pXRD confirmed the bulk structure of the prepared $BiVO_4$, the local structure of the bulk and surface states is unclear. To investigate the local structure about Bi atoms, XAS was performed at beamline 12-BM at the Advanced Photon Source at Argonne National Laboratory. From the XANES region (Figure 3.2a) corresponding to the $2p_{3/2}$-6d transition,[148] little change is observed as a function of film thickness, implying that the local and electronic structure is similar at all film thicknesses. In Fourier-transformed R-space, however, differences such as a shift in the first-shell peak to shorter distance and reduction in amplitude of the spectra for thinner films are observed (Figure 3.2b). To quantify these differences, FEFF fitting was performed using the published crystal structure of $BiVO_4$ as a model. Because a significant peak is observed at >2 Å, it was necessary to include second shell scattering atoms outside of the Bi-O_8 first shell. Using the crystal structure, these additional vectors are assigned to the V and Bi atoms that are connected to the O atoms surrounding the absorbing Bi atom. The

R-space data are shown in Figure 3.3 with best fit lines using the parameters listed in Table 3.1. From the fit parameters, it can be observed that all of the Bi-O vectors, which can be inferred as the Bi-O bond distance, are significantly shortened in the thinnest sample. In addition, the Debye-Waller factor (σ^2), which represents static and dynamic disorder in the photoelectron path length[149] is larger in the thinnest sample. Because the measurements are performed at the same temperature, the disorder is assigned as static and, therefore, means that the surface structure likely contains defect states. Additionally, the V K-edge spectra were collected and fit in a similar manner, but no differences were observed in the FEFF results for 0.02M-0.08M. Because the X-ray fluorescence yield of V is only approximately 20% of Bi due to the competing auger process, it was not feasible to collect data for the 0.1M sample. The lack of change for 0.02M-0.08M, however, is in agreement with Bi L_3 edge results and confirms that the local structure changes are likely isolated to the surface states of the film.

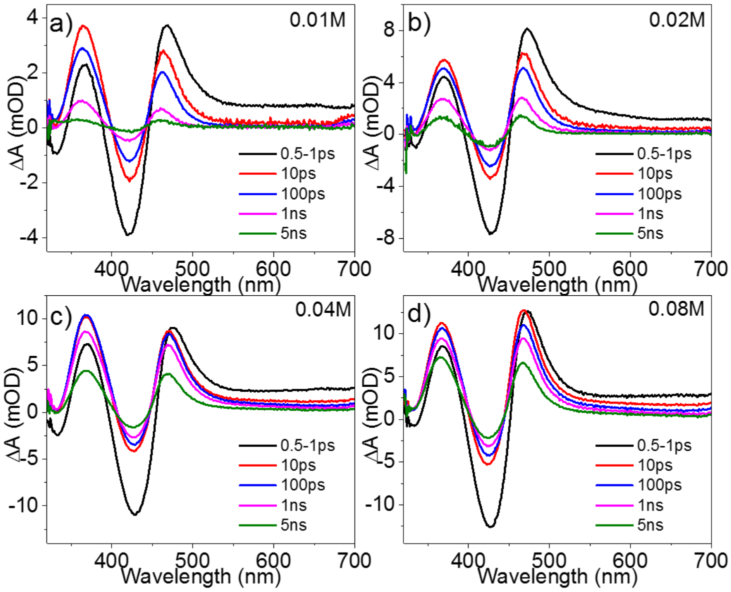

Figure 3.4. Femtosecond OTA spectra after excitation at 315nm for 0.01M (a), 0.02M (b), 0.04M (c), and 0.08M (d) $BiVO_4$.

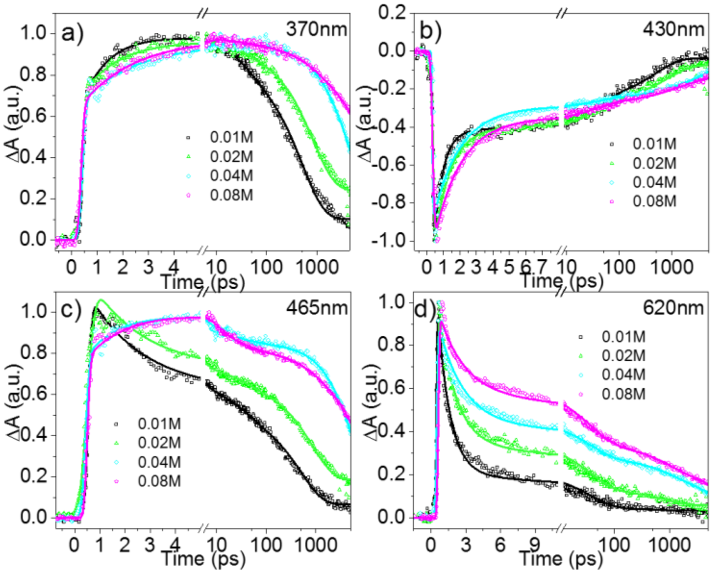

Figure 3.5. Kinetic traces and best fit lines for OTA features at 370 nm (a), 430 nm (b), 465 nm (c), and 620 nm (d). Open points are data and best fit lines are shown as solid lines.

Table 3.2. Fitting parameters for TA results. [a]Fifth time constant of 3.75 ps (22.0%). [b]Fifth time constant of 7.13 ps (15.9%). [r]Rising component.

Sample	Probe	τ_1,ps	(A_1,%)	τ_2,ps	(A_2,%)	τ_3,ps	(A_3,%)	τ_4,ps	(A_4,%)
0.01M	370	1.08	[r](24.7)	36.6	(13.6)	511	(54.0)	>>5ns	(7.6)
	430	0.53	(62.1)		(15.8)		(18.7)		(3.3)
	465	2.1	(40.4)		(14.9)		(38.6)		(6.0)
	620	1.08	(80.3)		(15.3)		(1.25)		(3.2)
0.02M	370	1.47	[r](21.7)	36.6	(5.5)	835	(5.4)		(19.2)
	430	0.96	(61.0)		(14.5)		(17.6)		(6.9)
	465	2.1	(37.2)		(8.2)		(38.7)		(15.9)
	620	1.47	(66.0)		(2.1)		(7.2)		(5.6)
0.04M[a]	370	2.1	[r](22.6)	36.6	(0.4)	835	(1.0)		(76.0)
	430	1.6	(66.5)		(60.2)		(5.6)		(21.9)
	465	2.1	[r](28.3)		(2.9)		(1.7)		(44.8)
	620	2.1	(51.6)		(18.3)		(8.9)		(21.1)
0.08M[b]	370	2.1	[r](25.1)	36.6	(2.3)	835	(9.5)		(82.7)
	430	1.6	(64.5)		(9.3)		(7.9)		(18.3)
	465	2.1	[r](23.8)		(5.5)		(6.6)		(48.1)
	620	2.1	(38.3)		(26.1)		(12.4)		(23.1)

While the local structure changes observed implied that surface states are different than bulk states, it is unclear how the more compacted and symmetric Bi center effects the photodynamics of $BiVO_4$. To investigate the contribution of surface and bulk states, transient absorption spectroscopy was performed at 0.01-0.08M $BiVO_4$ films (Figure 3.4). After 315nm excitation, the spectra all share similar features, namely positive absorption bands at 370 nm and 465 nm as well as a broad positive absorption feature at >600nm. These positive features are assigned as VB or trapped hole features based on previous works.[141,150,151] Additionally, a negative feature is observed at 430nm and is assigned to a exciton bleach feature due to the occupation of the CB by a photogenerated electron. While some changes in the evolution of the features are noticeable in the spectra, the kinetic traces and best fit lines in Figure 3.5 more clearly show the trends observed as a function of film thickness. The primary trends observed as a function of film thickness are the slower growth of positive features at 370 nm (Figure 3.5a) and 465 nm (Figure 3.5c) as film thickness increases as well as slower decay of the 620nm (Figure 3.5d) feature with an increase in film thickness. The negative exciton bleach at 430 nm (Figure 3.5b) feature shows a weaker trend, however the decay appears to be accelerated at early delay times for the thinnest films. Interestingly, there is a complete loss of the growth component at 465nm in the thinnest film, while some growth remains at 370nm.

The kinetic results were fit with a multiexponential model and the fit parameters are shown in Table 3.2. The 370nm positive feature is best represented by a rising component and multiple decay components. The rising components (τ_1) obtained from the fit vary as 1.08 ps (24.7%), 1.47 ps (21.7%), 2.1ps (22.6%), and 2.1 ps (25.1%) for

0.01, 0.02, 0.04, and 0.08M films, respectively. The rising feature at 370nm is assigned to a hole trapping process, and the increasing time constant with an increase in film thickness suggests that the trapping process if more facile in thinner films. Since thinner films contain a larger portion of surface states compared to bulk states, this result implies that photogenerated carriers in the bulk must migrate to the surface to undergo a trapping process, as revealed by the increase in time constant due to carrier diffusion. At 465 nm, the positive feature undergoes nearly instantaneous decay at early delay times (τ_2, 2.1 ps for all thicknesses) for thinner films and only has significant growth by 0.04 and 0.08M, indicating that the trapped hole feature at 465 nm is distinctly different in nature from the 370 nm trapped hole feature. By comparing the 465 nm kinetic decays to the 620 nm decays, it is observed that the kinetics are distinctly different, implying that the hole trap is not removed in thinner films. Rather, the hole trapping process at 465 nm is very fast (within IRF, <120 fs) in thinner films. Thus, the 465 nm feature is assigned as a shallow surface trap state that is populated nearly instantaneously in thinner films and the 370 nm feature is assigned as a deep surface trap state. The decay of the broad positive absorption feature at 620 nm (Figure 3.5d) is additionally affected by film thickness. The early time component, τ_1, is identical for 370 nm and 620 nm with increasing amplitude as film thickness decreases.

The later time constants (τ_2- τ_4) are assigned to recombination between the electron and trapped holes. It is observed, in agreement with the kinetic trends, that decay is amplitude-weighted to shorter time constants whereas thicker films generally have longer lifetimes. The faster decay in thinner films is attributed to trap-mediated recombination which, in combination with the assignment of two different surface hole trap states, suggests that trap-mediated recombination at the surface of $BiVO_4$ materials is an important photodynamic process. For thicker films, the negative exciton bleach feature at 430nm is the fastest decaying feature in the spectrum as seen by the 1.6 ps and large A_1 value relative to other wavelengths. If the electron in the CB is recombining with holes in the VB or trapped holes, then other features in the spectrum should share this fast decay component. Since they do not, τ_1 is assigned to an electron trapping process at 430nm. As a function of film thickness, it is observed that τ_1 varies with film thickness with values of 0.53, 0.96, and 1.6 ps for 0.01, 0.02, and 0.04-0.08M, respectively. Therefore, it is assigned to a surface trap state since it is faster in thinner films and is less limited by mobility in the bulk.

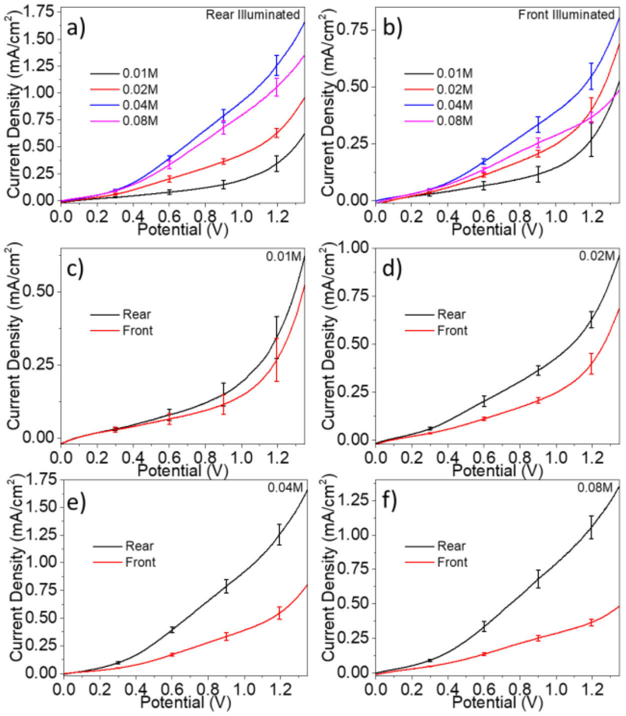

Figure 3.6. Linear sweep voltammetry (25 mV s^{-1}) of different thicknesses of $BiVO_4$ photoanodes compared under rear-illumination (a) and front-illumination (b). Comparisons of samples of the same thicknesses at rear vs. front illumination (c-f).

To evaluate the effect of film thickness on the photocatalytic performance for OER, linear sweep voltammetry was performed under Xenon lamp illumination (>400nm). As observed in Figure 3.6a, the observed photocurrent related to OER increases with film thickness until 0.04M and then decreases for 0.08M under rear-side illumination. For front side illumination (Figure 3.6b), a similar trend is observed, but the current densities observed are lower than the rear-illuminated values. This observation is confirmed by comparing the rear vs. front illumination photocurrent at each thickness, where it is observed that the deviation between the two illumination geometries increases significantly with an increase in film thickness. The reason for this difference is related to the electron mobility in the bulk of the film; for rear-illumination, photogenerated carriers are generated close to the back contact of the electrode whereas front-illumination generates electrons at the front of the films, where they must then migrate through the bulk of the film to reach the back contact. This point is supported by the trend in Figures 3.6c-f. For the 0.01M film, there is not a statistically significant difference between rear- and front-illumination. As the amount of bulk material increases, the difference increases. It is also noted that the potential-dependent profile for front-illuminated 0.08M $BiVO_4$ is quite different from the other thicknesses in Figure 3.6b, indicating hindered extraction of the photogenerated charges. Together, these PEC results suggest that, in agreement with previous studies, carrier mobility is a limiting factor for $BiVO_4$-catalyzed OER in a PEC related primarily to the bulk layer of $BiVO_4$.

Conclusion

In conclusion, the $BiVO_4$-thickness dependence studies correlate the structure of the surface and bulk states of $BiVO_4$ films of different thickness with their charge separation dynamics and OER performance. Characterization with pXRD showed that monoclinic scheelite phase is maintained in all thicknesses of $BiVO_4$, however the local structure changes for the thinnest 0.01M film leading to a more compacted, symmetric Bi center. These differing structural factors provide a surface environment where electron trapping and multiple hole trapping processes occur, leading to trap-mediated recombination and a decrease in carrier lifetime in the absence of a significant bulk layer, as demonstrated by TA experiments. PEC experiments to perform the OER demonstrated that the catalytic activity increases with film thickness initially, likely due to enhanced visible light absorption and enhanced photogenerated carrier lifetime in thicker films. However, a critical thickness is reached where increasing the thickness further leads to decreased catalytic activity due to ineffective charge transportation in the bulk of the material.

3.2 Atomic Insight into the W-Doping Effect on Carrier Dynamics and Photoelectrochemical Properties of $BiVO_4$ Photoanodes

Introduction

The findings in the thickness dependence studies suggest possible routes to improve the photoelectrocatalytic OER efficiency of $BiVO_4$. First, the surface of the material was found to contain multiple hole trap sites, including what is likely a deep hole trap state, as well as electron trap states. The existence of these states means that the mobility of photogenerated carriers might be limited at the surface of the material, which in turn could negatively impact the OER efficiency. Additionally, trap-mediated recombination limits the lifetime of photogenerated carriers which causes wasted photon energy and, in a prototypical device, low solar to hydrogen efficiency. In addition to these properties of the surface states, the bulk of the material was found to have relatively poor electron mobility since the photoelectrocatalytic performance was very sensitive to film thickness and illumination geometry. While thin film thickness can compensate this poor mobility, the absorption path length is much shorter and negatively impacts the catalytic efficiency. Therefore, the improvement of $BiVO_4$-based OER materials requires the passivation of trap states as well as the improvement of carrier mobility in the bulk.

To explore the optimum performance of $BiVO_4$, it is essential to perform a systematic study of the influence of the doping on the electronic structure and carrier dynamics of $BiVO_4$. In this work, we will fill this need and uncover the origins that affect the carrier trapping and photoelectrochemical (PEC) performance perturbed by doping in molecular level using the combination of X-ray absorption spectroscopy (XAS) and transient absorption spectroscopy (TA). We found that W doping results a less distorted (more symmetric) local structure at Bi center, which favorably extend the electron lifetime and dramatically change the nature of hole traps in $BiVO_4$ films.

Results and Discussion

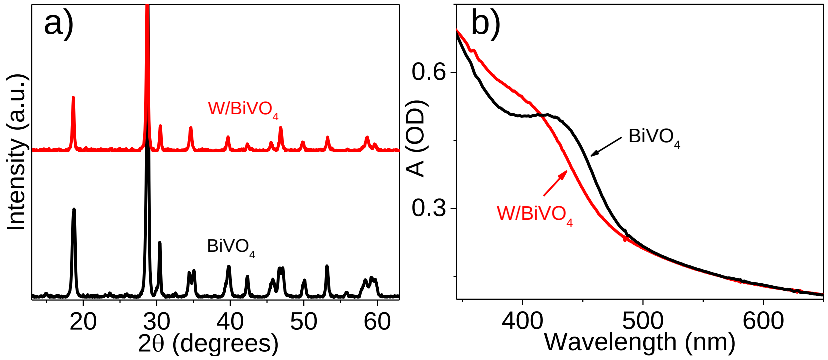

Figure 3.7. XRD patterns (a) and UV-Visible absorption spectra (b) comparing W/BiVO$_4$ and BiVO$_4$

One dopant that has been found to positively impact the OER efficiency for BiVO$_4$ materials is the electron donor atom W, which substitutes for V sites in the BiVO$_4$ structure. Using a similar synthesis strategy to undoped BiVO$_4$ films, W-doped BiVO$_4$ films were prepared by incorporating ammonium metatungstate into the precursor Bi solution at a known atom ratio. PEC experiments were carried out to test the photocatalytic efficiency at different dopant densities using the 0.04M film thickness. It was found that 1.8 at% W-doping gave the optimal results and, henceforth, will be referred to as W/BiVO$_4$. Figure 3.7a compares the pXRD patterns for BiVO$_4$ and W/BiVO$_4$. As evidenced by the reduced splitting at 35° and 46° 2θ, W/BiVO$_4$ has a partial phase change to tetragonal phase.[77,78] The structure change or the presence of W in the material also affects the optical properties of the film, which is observed in Figure 3.7b.

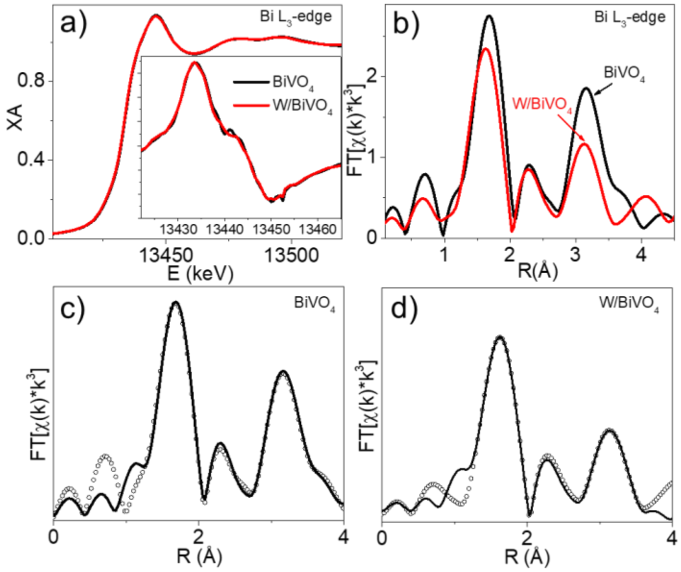

Figure 3.8. X-ray absorption spectroscopy at Bi L_3 edge (a) and first derivative inset. Fourier-transformed R-space comparison (b). FEFF fitting results for $BiVO_4$ (c) and $W/BiVO_4$ (d).

Table 3.3. EXAFS fitting parameters for $BiVO_4$ and $W/BiVO_4$ films.

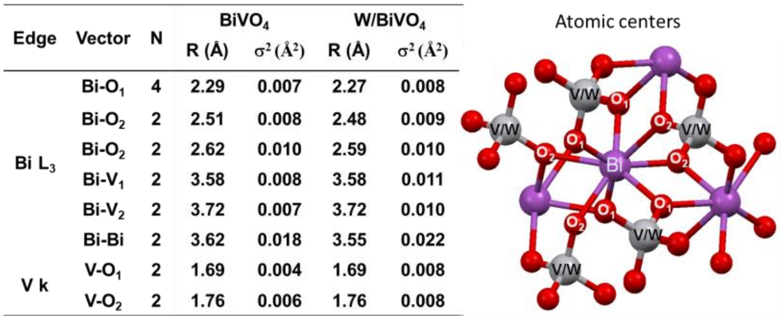

Edge	Vector	N	$BiVO_4$		$W/BiVO_4$	
			R (Å)	σ^2 (Å^2)	R (Å)	σ^2 (Å^2)
Bi L_3	Bi-O_1	4	2.29	0.007	2.27	0.008
	Bi-O_2	2	2.51	0.008	2.48	0.009
	Bi-O_2	2	2.62	0.010	2.59	0.010
	Bi-V_1	2	3.58	0.008	3.58	0.011
	Bi-V_2	2	3.72	0.007	3.72	0.010
	Bi-Bi	2	3.62	0.018	3.55	0.022
V k	V-O_1	2	1.69	0.004	1.69	0.008
	V-O_2	2	1.76	0.006	1.76	0.008

Because the optical properties might be closely related to the local structure of Bi or V atoms in the structure, XAS was performed to determine if any quantitative changes in the local structure could be observed due to W-doping. No obvious changes are observed in the XANES region for Bi L_3 edge (Figure 3.8a) indicating that the structure is not drastically altered by the incorporation of W dopants. Even though W is an electron-rich dopant atom, there is no shift in the first derivative peak corresponding to the $2p_{3/2}$-6d transition, indicating that the extra electron density resides on W atom and does not alter the oxidation state of Bi atoms. The Fourier-transformed R-space spectra (Figure 3.8b) indicate that W/$BiVO_4$ might result in the shortening of bond distances in both the first and second shells compared to $BiVO_4$ as a result of W incorporation. Quantitative EXAFS fitting (Figure 3.8c,d) was performed to confirm that, indeed, shorter bond lengths about Bi are observed. Table 3.3 shows that all of the Bi-O distances in W/$BiVO_4$ are shortened by 0.02-0.03 Å. Interestingly, the Bi-O_2 vectors are shortened more severely and Bi-O_1 vectors, resulting in a more symmetric local structure about Bi with W-doping. This result is in agreement with the partial phase change to tetragonal that was observed in pXRD, as the tetragonal structure contains a more symmetric Bi-O_8 dodecahedron. Additionally, as suggested by the reduced amplitude in R-space shown in Figure 3.8b, σ^2 fits to a larger value indicating a higher degree of static disorder in the doped films. The V K edge fits indicated that no change in the average V-O distance is imparted due to W-doping, however significant disorder was observed, in agreement with the Bi edge data.

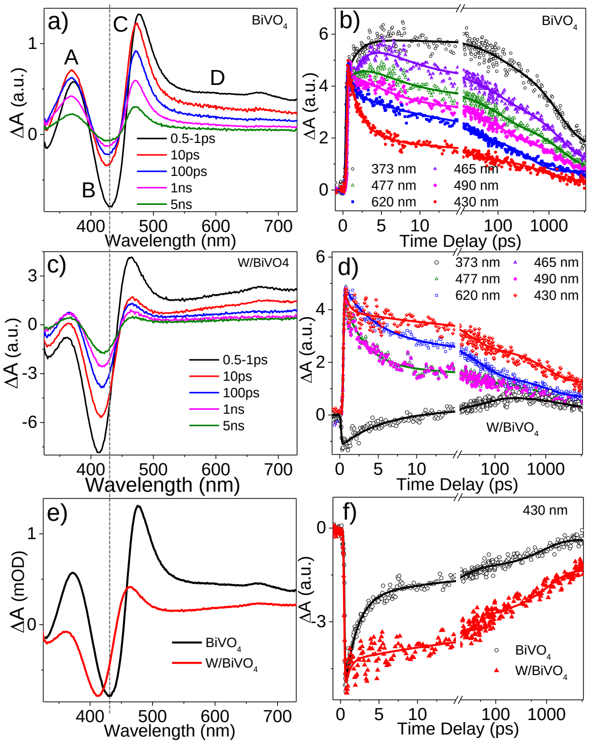

Figure 3.9. Femtosecond OTA spectra of undoped $BiVO_4$(a) and W/$BiVO_4$ (c). Probe wavelengths dependent kinetic traces of $BiVO_4$ (b) and W/$BiVO_4$ (d). Comparison of TA spectra at 0.5-1ps time delay (e). Comparison of exciton bleach recovery kinetics between $BiVO_4$ and W/$BiVO_4$ (f).

Table 3.4. Multiexponential fitting parameters for OTA kinetics of $BiVO_4$ and W/$BiVO_4$.

Sample	Probe	τ_1,ps (A_1,%)		τ_2, ps (A_2,%)		τ_3, ps (A_3,%)		τ_4, ps (A_4,%)	
$BiVO_4$	430 nm	1.6	(61.9)	36.6	(16.5)	835	(14.0)	>> 5ns	(7.6)
	370 nm	2.1	^{r}(100)	36.6	(6.5)	835	(43.3)	>> 5ns	(30.2)
	465 nm		^{r}(100)		(24.9)		(33.8)		(23.9)
	477 nm		(4.0)		(30.6)		(39.7)		(25.7)
	490 nm		(18.3)		(28.7)		(33.2)		(19.8)
	620 nm		(33.1)		(30)		(23.7)		(13.2)
W/$BiVO_4$	430 nm	4.0	(18.1)	50	(25.4)	1080	(27.5)	>> 5ns	(29.0)
	370 nm	3.1	^{r}(42.4)	50	^{r}(31.1)	1080	(13.7)	>> 5ns	(12.8)
	465 nm		(61.1)		(10.0)		(18.6)		(10.3)
	620 nm		(40.7)		(30.9)		(14.4)		(14.3)

The changes in carrier dynamics as a result of W-doping were investigated by OTA. Features A, C, and D in Figure 3.9a are assigned to trapped hole features and the negative feature, B is assigned to exciton bleach due to CB population after photoexcitation. For undoped $BiVO_4$, the kinetic traces in Figure 3.9b show that the exciton bleach is the fastest decaying feature and the hole features exhibit wavelength dependent kinetics that is characteristic of a carrier trapping process. Similar to the spectra of undoped $BiVO_4$, the spectra of W/$BiVO_4$ (Figure 3.9c) show the same four main features (A-D). However, some distinct differences are observed for W/$BiVO_4$: 1) it is observed that the intensities of A, C, and D have reduced intensity relative to the exciton bleach feature. This change is accompanied by a vanishing in the rising component at C. 2) The whole spectra for W/$BiVO_4$ shifts to shorter wavelengths, consistent with the shifts in steady-state UV-Visible results. 3) Instead of the strong probe wavelength dependence observed in $BiVO_4$ kinetics for C-D, the W/$BiVO_4$ kinetics have negligible probe wavelength dependence. 4) The exciton bleach recovery becomes much slower in W/$BiVO_4$ compared to $BiVO_4$.

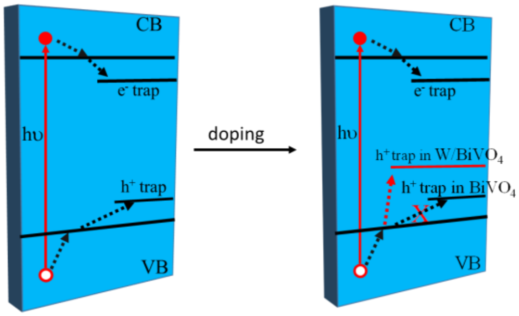

Figure 3.10. Proposed carrier dynamics scheme in $BiVO_4$ (left) and W/$BiVO_4$ (right) thin films.

The changes observed in the spectral features due to W doping can be well-explained by the model proposed in Figure 3.10. W doping alters the hole trapping dynamics by significantly removing the hole traps, accounting for the significantly reduced amplitudes at A, C, and D, the diminished rising component in C, and the negligible probe-wavelength dependence of C-D in the W-doped sample. These results imply that W-doping removes the intrinsic hole trap that was present in $BiVO_{4,}$ hence the reduce intensity in the hole absorption features at early time delay in OTA spectra for W/$BiVO_4$.While the hole trap features are less prominent in W/$BiVO_4$ compared to $BiVO_4$, the kinetic traces a A, C, and D are still different in W/$BiVO_4$. Instead of faster decay of D than C, which was observed in $BiVO_4$, C decays faster than D in W/$BiVO_4$ suggesting that a distinctly different trapping process still occurs in W/$BiVO_4$. Despite the formation of new hole traps in W/$BiVO_4$, the exciton bleach kinetics show slower recovery than $BiVO_{4,}$ indicating slower overall recombination between holes and electrons due to diminishing of the intrinsic hole traps.

A multiexponential model was used to quantify the carrier dynamics in undoped and doped films at the different probe wavelengths shown in Figure 3.9b,d. The kinetic traces at all wavelengths are best represented by a four-exponential function, where the fourth component is a >>5 ns component that accounts for remaining signal at the end of the available 5ns probe window. As shown in Table 3.4, the kinetic traces at 370 nm and 465 nm require a rising component (2.1 ps) and two decay components in addition to the >>5 ns component (36.6 ps and 835 ps). At the other hole features, 477, 490, and 620 nm, the rising component is no longer present and is replaced by a decay component of the same time constant. The exciton bleach kinetics at 430 nm are represented by a fast 1.6 ps decay component plus three additional decay components with the same time constant as the hole features. Because the early time constants for hole features (2.1 ps) and exciton bleach decay (1.6 ps) are distinctly different, we assign these time constants to hole trapping process and electron trapping process, respectively. The additional time constants are assigned to recombination between the trapped holes and electrons in the CB.

The same model was used to fit W/$BiVO_4$ kinetics, allowing the time constants representing trapping and recombination processes to change. The hole absorption features are fit with a hole trapping time constant of 3.1 ps and carrier recombination time constants of 50 ps, 1080 ps, and >>5 ns. The fast decay at early time delay for exciton bleach kinetics at 430 nm was fit with a time constant of 4.1 ps, which is much slower than the 1.6 ps time constant that was observed in undoped $BiVO_4$. This longer electron trapping time constant, along with longer exciton bleach lifetime for W/$BiVO_4$, imply that electron trapping is altered significantly by the incorporation of W dopant. While the full decay profile is well outside the time window of femtosecond OTA experiments, the carrier recombination rate cannot be compared quantitatively. However, estimation of the half-recovery time for the exciton bleach feature gives approximately 3.1 ps for $BiVO_4$ and 147.9 ps for W/$BiVO_4$ indicating that electron lifetime is elongated approximately 50x upon W doping.

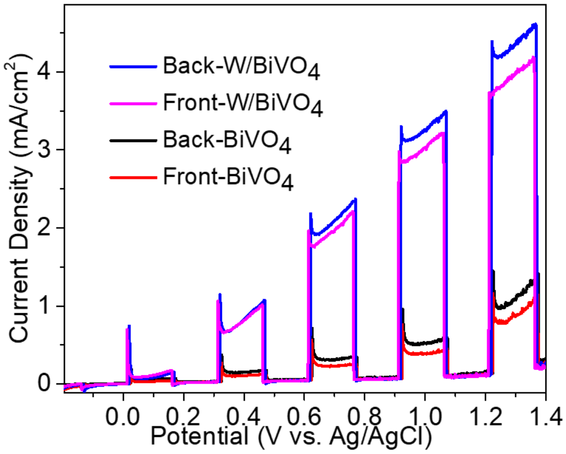

Figure 3.11. Photocurrent comparison of $BiVO_4$ and $W/BiVO_4$ photoanodes under back and front illumination with chopped Xenon lamp in 0.1M Na_2SO_4.

To correlate the fundamental photodynamic studies with PEC performance, $BiVO_4$ photoanodes were prepared on FTO using the same preparation procedures. The photocurrent was measured via linear sweep voltammetry under chopped Xenon lamp illumination. Figure 3.11 compares the photocurrents of $BiVO_4$ and $W/BiVO_4$ measured under both front and back illumination geometries. Compared to undoped $BiVO_4$, $W/BiVO_4$ displays significantly enhanced photocurrent for OER implying that W plays an important role in improving the PEC performance of $BiVO_4$. For both films, the difference between front and back illumination geometries is present, indicating that electron mobility in the bulk is still hindered in both films. However, at lower potentials, the difference is slightly improved by W doping. These results suggest that carrier transport is still the limiting factor in W/BiVO4 despite the greatly enhanced photocurrent compared to the undoped material. The significant improvement of PEC performance with limited increase in carrier transport leads us to believe that the increased electron lifetime due to the elimination of intrinsic hole traps plays a major role in the PEC performance of $W/BiVO_4$.

Conclusions

In summary, W-doping imparts improved PEC performance and charge separation to $BiVO_4$ thin films. Replacement of the V site by W dopant modifies the bulk structure slightly to cause a partial phase change to tetragonal structure while the local structure at the Bi center shows a reduction of the Bi-O bond distances and a less distorted, more symmetric structure compared to undoped $BiVO_4$. These structural changes are responsible for altering the nature of both hole and electron traps in the material by favorably removing the intrinsic hole traps in $BiVO_4$ and reducing the hole trapping process, allowing enhanced charge separation and longer electron lifetime. Because the carrier transport in the bulk has limited improvement upon W doping, the increased charge separation is likely the reason for the significant improvement in PEC performance in W/$BiVO_4$. These studies demonstrate that W-doping solves one of the limiting factors in $BiVO_4$, namely the intrinsic hole trapping dynamics, and highlight that further improvement of $BiVO_4$-based OER materials should focus on improving carrier mobility in the material.

3.3 The Effect of Mo Doping on the Charge Separation Dynamics and Photocurrent Performance of $BiVO_4$ Photoanodes

Introduction

Doping with electron-rich elements has been shown as an attractive approach to improve the overall OER performance. For example, several studies have demonstrated the improved electron mobility and photoelectrochemical performance by W and Mo doping, which has been attributed to the increased electron density.[90,135,145] In contrast, other studies suggested that doping can introduce trap states and serve as recombination centers that enhance electron-hole recombination, which may decompensate the improved carrier mobility.[135,146] Our recent studies on W-doped $BiVO_4$ photoanode, however, suggested that the increased photocurrent upon W doping is largely attributed to the significant reduction of hole trap states, which inhibit electron-hole pair recombination, while poor carrier mobility still remains as a limiting factor.[92] These previous studies suggest that doping may produce multipart influences on the electronic properties and charge separation efficiency despite its promise for overall OER improvement.

In order to gain a deep understanding of the doping mechanism in $BiVO_4$ photoanode, it is necessary to examine the effect of doping on the carrier dynamics and OER performance with different dopants other than W. In this work, we investigate the effect of Mo doping on the morphology, carrier dynamics, and photocurrent performance of $BiVO_4$ photoanode, as well as their dependence on Mo concentration.

Results and Discussion

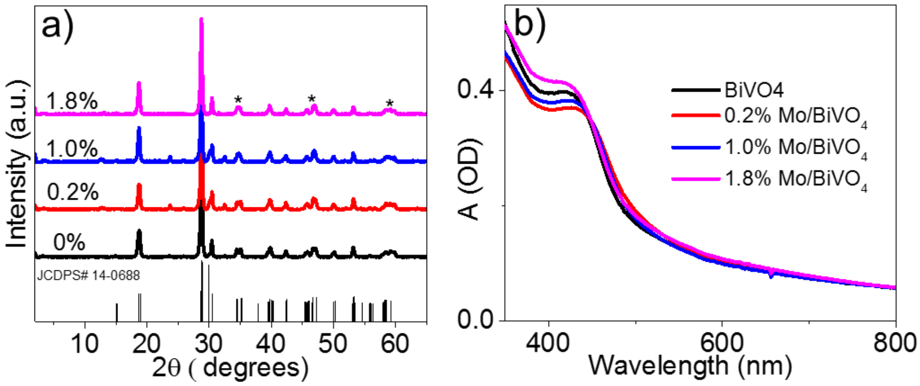

Figure 3.12. pXRD patterns (a) and UV-Visible spectra (b) for undoped and Mo/BiVO$_4$ at different % doping.

Mo/BiVO$_4$ films were prepared at a wide range of dopant concentrations from 0.2% through 5%, however >2% concentration led to severe morphological heterogeneity and reduced PEC performance, so they were excluded from photophysical studies. The crystalline phase of Mo/BiVO$_4$ was investigated using pXRD (Figure 3.12a). From undoped BiVO$_4$ to 1.8% Mo/BiVO$_4$, it is observed that the peak splitting at 35˚, 46˚, and 58˚ 2θ become less prominent. This could be consistent with a partial phase change to tetragonal, however no clear shifting is observed in the UV-Visible spectra (Figure 3.12b). These results suggest that Mo/BiVO$_4$ films maintain a mostly monoclinic scheelite structure.[77,78]

Table 3.5. Fitting parameters for TA kinetics of un-doped $BiVO_4$ and Mo-doped $BiVO_4$ films.

Probe	sample	τ_1,ps (A_1,%)	τ_2, ps (A_2,%)	τ_3, ps (A_3,%)	τ_4, ps (A_4,%)	
430 nm	0%	1.6 (64)	23 (14.5)	874 (15.1)	>> 5ns	(6.4)
	0.2%	2.2 (58.7)	37.7 (17.0)	1130 (12.7)		(11.5)
	1.0%	2.2 (45.5)	35.3 (22.8)	1130 (18.9)		(12.8)
	1.8%	2.2 (37.2)	49.1 (24.0)	1130 (24.2)		(13.8)
472 nm	0%	^{r}2.1 (100)	16.5 (32.5)	970 (44.4)	>> 5ns	(23.1)
	0.2%	^{r}4.2 (100)	21.1 (39.6)	964 (40.9)		(19.5)
	1.0%	^{r}5.3 (100)	15.6 (39.7)	794 (39.7)		(20.6)
	1.8%		5.0 (57.6)	628 (26.8)		(15.6)

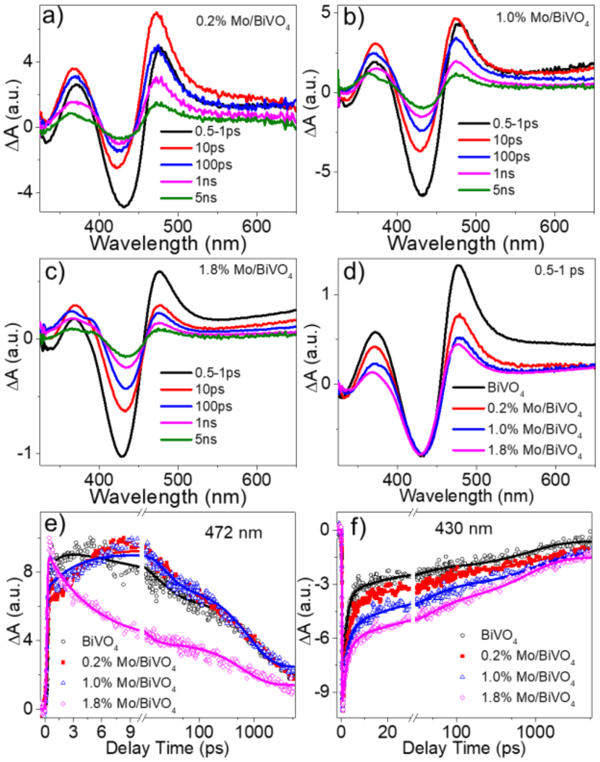

Figure 3.13. Femtosecond OTA spectra of 0.2-1.8% Mo/$BiVO_4$ (a-c). Comparison of undoped and doped OTA spectra at 0.5-1ps time delay (d). Normalized kinetic data and solid best fit lines at 472 nm (e) and 430 nm (f).

The carrier dynamics of Mo/$BiVO_4$ were investigated using femtosecond transient absorption spectroscopy. Figures 3.13a-c show the OTA spectra of Mo/$BiVO_4$ films with 0.2%, 1.0%, and 1.8% Mo concentrations, respectively. The Mo doped films exhibit the same features as undoped $BiVO_4$ after 315 nm excitation, namely the two positive hole trap features at 370 nm and 470 nm, the broad positive hole trap feature at >600nm, and the exciton bleach feature at 430nm. The comparison of the early delay time spectra in Figure 3.13d shows that when normalized to the initial exciton bleach intensity, the intensity of the trapped hole features are greatly reduced in Mo/$BiVO_4$ samples and follow a trend with increasing Mo concentration. Together with the apparent spectra trends of the trapped hole features, these results suggest that the intrinsic hole traps in the undoped $BiVO_4$ film are reduced due to Mo doping.

The reduction of hole traps in Mo-doped $BiVO_4$ films is further supported by the diminishing rising component at 472 nm, which is assigned to the hole trapping process in $BiVO_4$ films. As shown in Figure 3.13e, a clear rising component was observed in the kinetic trace of undoped $BiVO_4$ film. In contrast, this rising component becomes slower in 0.2% through 1.0% Mo/$BiVO_4$ and then completely disappears for the 1.8% Mo/$BiVO_4$ film. The kinetic traces for undoped $BiVO_4$, 0.2% Mo/$BiVO_4$, and 1.0% Mo/$BiVO_4$ can be adequately fitted by a single rising component and three decay components, whereas 1.8% Mo/$BiVO_4$ can be fitted by three decay components as shown by the fit parameters in Table 3.5. The hole trapping process time constant increases as 2.1 ps, 4.2 ps, and 5.3 ps for undoped $BiVO_4$, 0.2% Mo/$BiVO_4$, and 1.0% Mo/$BiVO_4$ respectively suggesting that the hole trapping process is retarded with increasing Mo concentration. The remaining decay components correspond to the recombination between trapped holes with electrons in the CB or electron trap states. In addition to the hole trapping dynamics, the effect of Mo doping on the electron dynamics was examined by probing the exciton bleach kinetics (Figure 3.13f), which can be fit by a four exponential decay function for all samples. The electron trapping time constant, τ_1, increases from 1.6 ps for the undoped sample to 2.2 ps for all of the Mo-doped films. Additionally, the overall exciton bleach recovery kinetics become slower in Mo/BiVO$_4$ and follow a trend with increasing dopant concentration, indicating that the overall electron-hole recombination is inhibited with increasing Mo concentration.

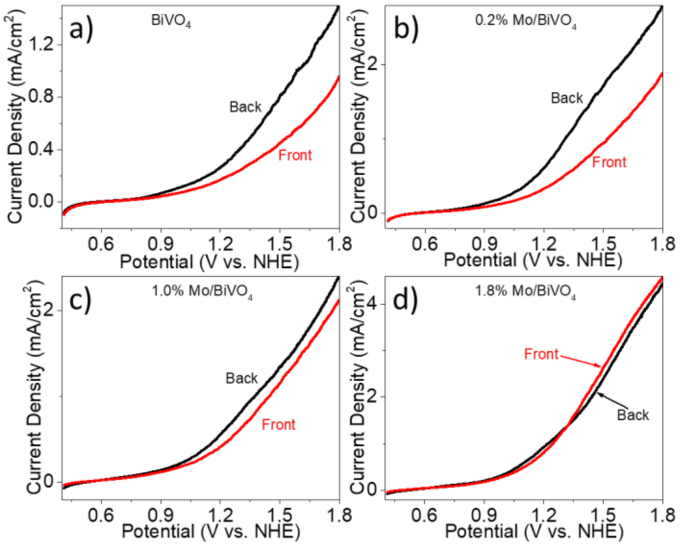

Figure 3.14. The comparison of photocurrent from back-side and front-side illumination for BiVO$_4$ and Mo/BiVO$_4$.

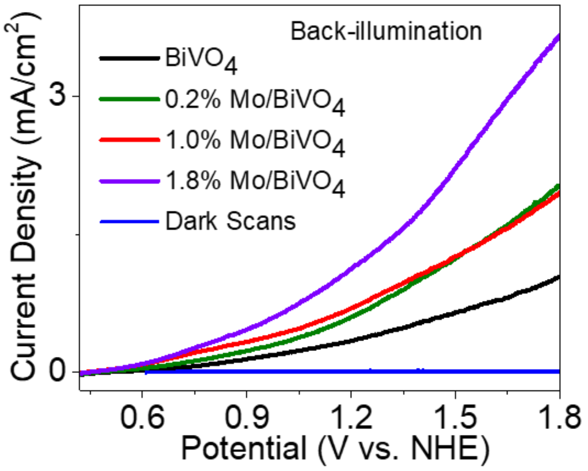

Figure 3.15. Comparison of the photocurrent for undoped BiVO$_4$ and Mo/BiVO$_4$ under back-side illumination.

While OTA studies showed that Mo doping caused a reduction in hole and electron trapping and elongated the overall electron-hole lifetime, characteristics that should aid in OER, they do not give direct insight into the PEC performance of the doped films. Photoanodes were prepared on FTO and irradiated with a Xenon lamp in either the front-illumination or rear-illumination geometry during linear-sweep voltammetry experiments as shown in Figure 3.14. Because rear-illumination generates more photogenerated electrons near the back contact, it will typically give larger photocurrents than the front-illumination geometry when electron mobility is limited in the material. From the photocurrent traces of undoped $BiVO_4$ (Figure 3.14a), it is evident that a large deviation between the two illumination geometries is present, implying poor carrier mobility in the material. With an increasing Mo dopant concentration (Figure 3.14 b-d), the difference between rear- and front-illumination becomes smaller and eventually disappears for 1.8% Mo/$BiVO_4$. This result strongly suggests that the poor electron mobility in $BiVO_4$ is significantly improved by Mo doping, leading to higher photocurrent densities with an increase in Mo-dopant concentration (Figure 3.15). Together, along with the reduced photogenerated carrier trapping observed in OTA experiments, it is shown that the benefits of Mo-doping are multifaceted and have an overall positive effect on the photoanode performance of $BiVO_4$.

Conclusions

In conclusion, the effect of Mo doping on the carrier dynamics and OER performance of $BiVO_4$ photoanodes was investigated. Using transient absorption spectroscopy, we show that both electron and hole traps are reduced upon Mo doping, inhibiting the electron-hole recombination. The studies of photocurrent measurement using linear sweep voltammetry reveal an improved photocurrent with increasing Mo concentration. Significantly enhanced electron mobility was observed due to the closing of the gap between frontside and backside illuminated photocurrents with increasing Mo concentration. These findings show great promise for Mo-BiVO4 as an OER photocatalyst and highlight the fundamental differences imparted due to Mo-doping.

Summary

$BiVO_4$ is a promising candidate as a photoanode to perform the water splitting reaction due to its favorable energetic alignment of its VB with OER and near-favorable alignment of its CB with HER. In its monoclinic scheelite form, its 2.4 eV bandgap allows the absorption of visible light and could be used in a tandem setup with an HER photocatalyst that absorbs light < 2.4 eV. Despite these favorable attributes, $BiVO_4$ suffers from some major drawbacks that were revealed by OTA and PEC studies in this work. First, significant photogenerated hole and electron trapping occurs at the surface of $BiVO_4$. While having a significant bulk layer delays the trapping process, it was shown that the poor electron mobility in the bulk of $BiVO_4$ can become a limiting factor in the PEC performance when the film thickness reaches a critical thickness. These factors imply that, for pristine $BiVO_4$, photoanode films must be sufficiently thin in order for electrons to migrate to the back contact of the photoanode to be transferred to the HER photocatalyst. However, thin films exhibit low photocurrent due to, in part, insufficient light absorption path length. As such, optimization of pristine $BiVO_4$ systems is full of challenge and compromise between unfavorable effects.

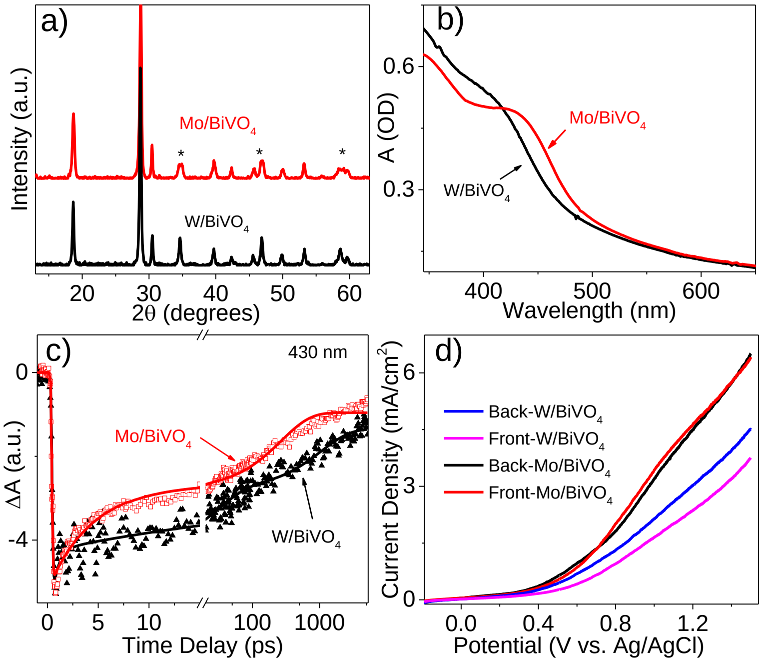

Figure 3.16. Comparison of XRD patterns (a) UV-Visible spectra (b), OTA exciton bleach kinetics at 430 nm (c) and PEC performance (d) for W/$BiVO_4$ and Mo/$BiVO_4$ at 1.8 at% doping.

It was shown that doping $BiVO_4$ with either W or Mo atoms significantly improves the material at an optimal concentration of 1.8 at%. For both dopants, hole and electron trapping were inhibited, which should be beneficial toward OER because improved carrier migration at the surface should assist with the difficult four-hole oxidation process in OER. Both dopants also significantly improved the photocurrent performance of the material. Still, some significant differences between the effects of the two dopants can be observed, and are compared in Figure 3.16. From pXRD comparisons, it can be observed that the reduction in splitting of the highlighted peaks is more complete in W/$BiVO_4$, indicating that the crystalline phase becomes more tetragonal in W/$BiVO_4$ than in Mo/$BiVO_4$. This observation is supported by the comparison of the UV-Visible spectra (Figure 3.16b), which shows an increase in bandgap energy for the more tetragonal species, W/$BiVO_4$. While both dopants decreased the electron-hole recombination rate, it was observed that W/$BiVO_4$ has longer lifetime (Figure 3.16c). Despite its slightly shorter lifetime, however, Mo/$BiVO_4$ exhibits larger photocurrent density compared to W/$BiVO_4$ likely due to the improved electron mobility in the bulk and its increased visible light absorption ability (Figure 3.16d). Together, these results suggest that from an OER efficiency perspective, Mo is the preferred dopant. However, because the effects of each dopant are slightly different, the dopant choice is dependent on the desired properties of the photocatalyst material.

Chapter 4

INTRINSIC PHOTODYNAMICS OF ZEOLITIC IMIDAZOLATE FRAMEWORKS AND EVIDENCE OF PHOTOINDUCED CHARGE SEPARATION

Driven by the increasing global energy demand, recent development in the field has extended the application of ZIF materials toward photocatalysis using visible light. Although still in the early stage of exploration, ZIFs have been used as photocatalysts for dye and phenol degradation as well as CO_2 reduction.[121,152-154] In these systems, photoactive nanostructures/molecules are incorporated into the highly porous structure of ZIFs, where ZIFs are used as a simple host or passive medium for dispersing the catalytic active species. This strategy has been widely used in developing zeolite-based photocatalysts[155] and recently in preparing MOF/nanocomposite or MOF/molecular catalyst hybrids,[154,156,157] yet suffers from challenges, notably the difficulty in preventing the guest material aggregation and the lack of the control over spatial distribution and homogeneity.[156,158-161] An alternative approach, which has recently been used in developing photoactive MOFs, is to develop the framework which exhibits an intrinsic photochemical response and thereby can be directly applied in photocatalysis.[162,163]

4.1 Excited State Dynamics in Zeolitic Imidazolate Framework

Introduction

As photocatalysis is based on a charge-transfer (CT) event following photoexcitation, it is essential to gain an intimate knowledge of the excited-state and charge transport properties within the ZIF framework, the properties that remain unexplored. Here, the first study on the excited-state dynamics in ZIF-67 thin film is reported using optical transient (OTA) and X-ray transient absorption (XTA) spectroscopy.

Results and Discussion

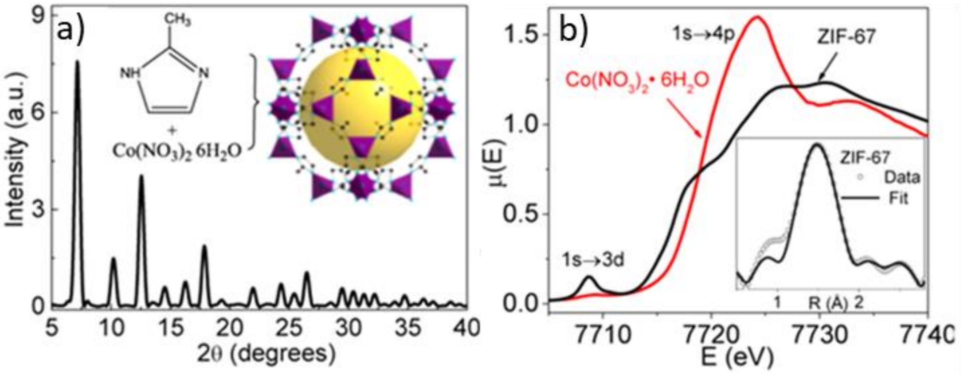

Figure 4.1. pXRD pattern for ZIF-67 (a) and Co K-edge XANES spectra (b) for ZIF-67 and $Co(NO_3)_2$•$6H_2O$. Inset of (a) shows the precursors used to form the displayed ZIF-67 SOD cage. The yellow sphere indicates the large cavity of the porous framework. The inset of (b) shows the EXAFS fitting in R-space for ZIF-67 fit using a FEFF model and the published ZIF-67 crystal structure.[164]

Thin films of ZIF-67 were prepared according to the established protocols.[165] Three film layers were grown to give films thick enough for optical characterization. The bulk structure of the as-synthesized ZIF-67 was measured by pXRD (Figure 4.1a). The patterns observed agree well with the peaks characteristic of the SOD structure of ZIF-67,[165,166] suggesting the successful synthesis of ZIF-67. Furthermore, the local structure of ZIF-67 at Co center was examine using steady-state X-ray absorption spectroscopy (XAS). Figure 4.1b shows the XANES spectrum of ZIF-67 at Co K-edge. The XANES spectrum of $Co(NO_3)_2$•$6H_2O$, the precursor used as Co^{2+} source in ZIF-67 synthesis, is compared to ZIF-67 because $Co(NO_3)_2$•$6H_2O$ is known to have octahedral coordination of Co. The prominent pre-edge feature in ZIF-67 is observed and is characteristic of tetrahedral coordination due to p-d mixing and the loss of an inversion center.[167,168] Notably, this feature is nearly absent in the octahedral Co precursor. Furthermore, the main absorption edge in the XANES spectrum of ZIF-67, arising from the dipole allowed 1s-4p transition, shows a less sharp peak than that of $Co(NO_3)_2 \cdot 6H_2O$, which can be ascribed to the decreased multiple scattering for a tetrahedral coordination in the former compared to octahedral geometry in the latter.[168] Further confirmation of the tetrahedral structure is confirmed by quantitative EXAFS fitting (inset of Figure 4.1b), which demonstrates that Co has four nitrogen neighbors with average Co-N distance of 1.99 Å.

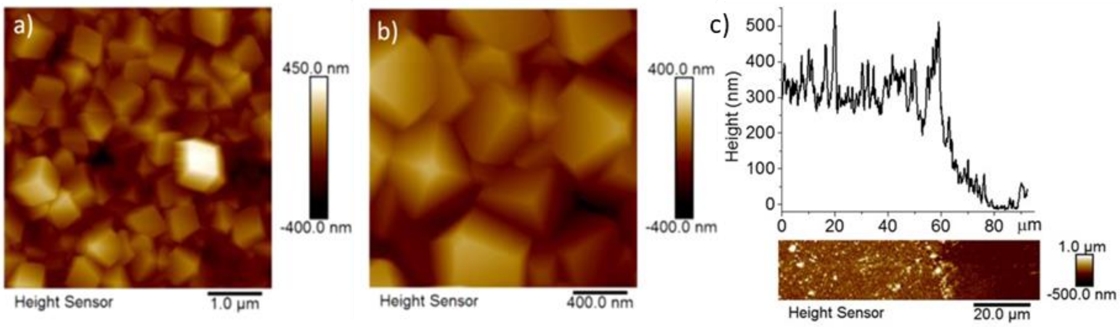

Figure 4.2. AFM topography images of ZIF-67 thin film at low (a) and high (b) resolution. The cross-section measurement of the film (c).

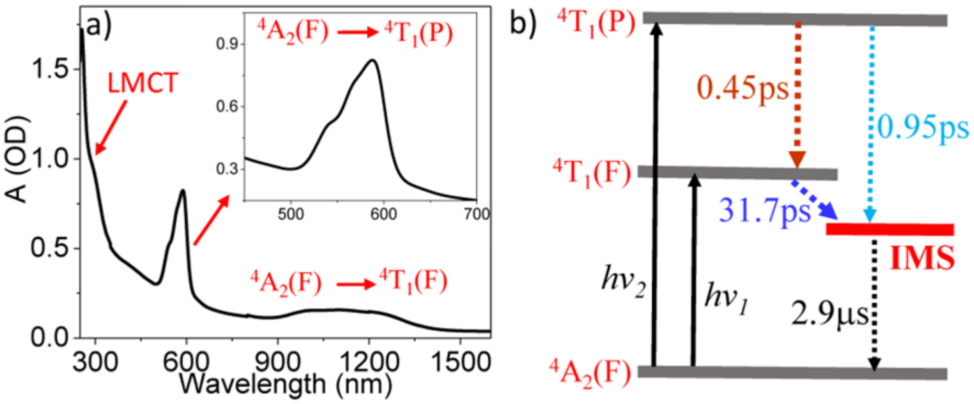

Figure 4.3. UV-Visible-NIR absorption spectrum of ZIF-67 thin film (a). The schematic representation of Co2+ in the tetrahedral geometry and the excited-state relaxation dynamics of ZIF-67.

The morphology of ZIF-67 films were characterized by atomic force microscopy (AFM) in PeakForce feedback mode. Figure 4.2a-b show the AFM images and demonstrate that the ZIF-67 film formed on the substrate is continuous and consists of crystals with truncated rhombic dodecahedral shape of ~300-500nm size. The cross-section of the film (Figure 4.2c) indicates that the thickness of the film is ~350nm, suggesting that the film is likely composed of a layer of single crystals.

The optical properties of ZIF-67 were first investigated by UV-Visible-NIR spectroscopy (Figure 4.3a). The spectrum exhibits three absorption features, including a broad absorption in the UV region <380 nm, a visible band with three distinct maxima centered at 588, 567, and 539 nm, and a broad NIR feature band from 900-1400 nm. These features can be attributed to the LMCT transition, the higher-lying [$^4A_2(F)$–$^4T_1(P)$] and lower-lying [$^4A_2(F)$–$^4T_1(F)$] d–d ligand field transitions, respectively, and are well-known features for Co^{2+} in tetrahedral environment,[169] consistent with the pXRD and XAS results. The schematic in Figure 4.3b shows the energetic ordering of the Co d-d states corresponding to the observed UV-Visible-NIR transitions from the singly-degenerate ground state to the triply-degenerate excited states.

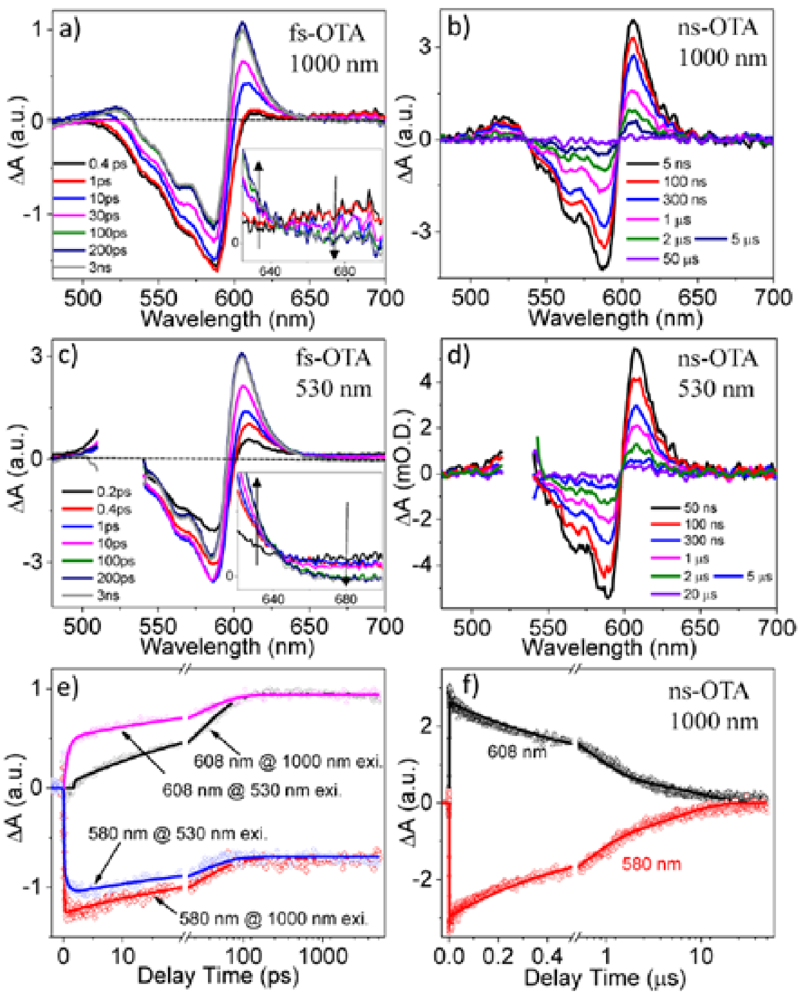

Figure 4.4. Femtosecond (a) and nanosecond (b) OTA spectra of ZIF-67 after 1000nm excitation. Femtosecond (c) and nanosecond (d) OTA spectra after 530 nm excitation. The comparison of kinetics at 608 and 580 nm in femtosecond OTA after 1000 and 530 nm excitation (e). The kinetics at 608 and 580 nm in nanosecond OTA spectra of ZIF-67 after 1000 nm excitation.

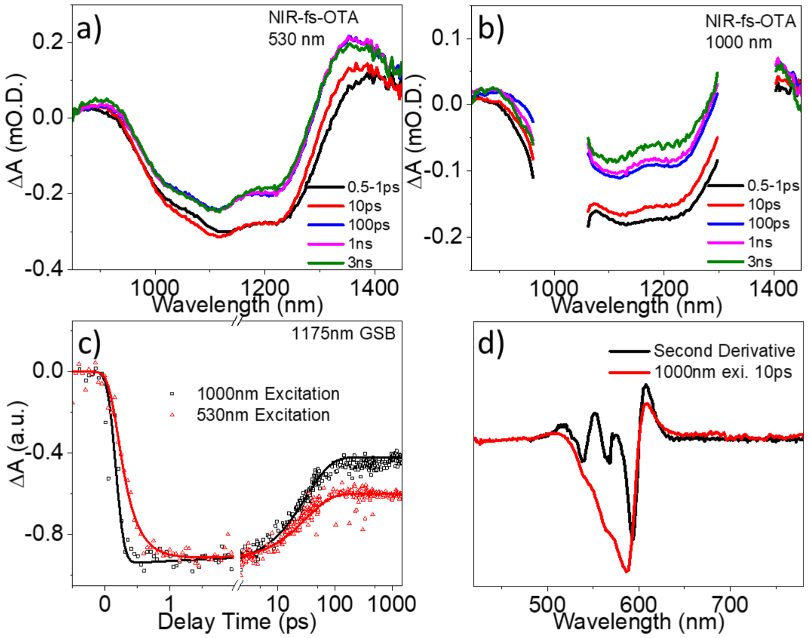

Figure 4.5. Femtosecond NIR OTA spectra of ZIF-67 thin films after 1000 nm (a) and 530 nm (b) excitation. Comparison of the kinetics after 1000 nm excitation and 530 nm excitation, showing the same trends observed at the visible d-d GSB bleach (c). Comparison of the second derivative of the steady-state UV-Visible spectra to the transient spectrum obtained at 10 ps time delay after 1000 nm excitation (d). In (b), the 1000 nm excitation and an artifact at ca. 1350 nm resulted in detector saturation and were removed from the spectra.

Ultrafast OTA spectroscopy was used to investigate the excited-state dynamics of ZIF-67 by selectively exciting the two d–d transitions. Figure 4.4a shows the femtosecond OTA (fs-OTA) spectra of ZIF-67 thin film in the visible region after exciting the lower-lying d–d band using 1000 nm light. Immediately following excitation, the OTA spectrum shows a negative band with triplet maximum in 520–600 nm region and a broad positive feature at >605 nm. The negative band strongly resembles the inverted ground-state (GS) absorption of $^4A_2(F)$–$^4T_1(P)$ transition and can thus be attributed to the bleach of $^4A_2(F)$ state due to photoexcitation. The broad positive band decays within ~200 ps (inset of Figure 4.4a), which is accompanied by the emergence of a new positive band centered at 605 nm. These two features are separated by a clear isosbestic point at 647 nm, suggesting that the decay of the former is associated with the formation of the latter. Meanwhile, another positive band was formed at ~525 nm within the same time regime. All of these spectral features together made the whole OTA spectra derivative-like shape, which maintains through the microsecond time as shown in nanosecond OTA (ns-OTA) spectra (Figure 4.4b), where the recovery of GS bleach and the decay of the two absorption bands centered 525 and 605 nm occur simultaneously. The presence of two isosbestic points at 536 and 599 nm confirms that these spectral evolutions are associated with the same recombination process. Similar spectral features were also observed in the near-IR OTA spectra representing the $^4A_2$(F)–$^4T_1$(F) transition (Figure 4.5a-c), consistent with our assignment earlier that the two d–d bands share the same GS, i.e., $^4A_2$(F).

Upon excitation of the higher-lying d–d band using 530 nm light, both fs- (Figure 4.4c) and ns-OTA spectra (Figure 4.4d) show the similar spectral features as the spectra after 1000 nm excitation, i.e., the instantly formed GS bleach and broad absorption (>605 nm) which decays to form a long-lived intermediate state with derivative-like spectral feature. However, extra rising components were observed in both GS bleach and 605 nm absorption band in the spectra of 530 nm excitation. These additional features can be more clearly seen in Figure 4.4e, where the kinetic traces at 580 and 608 nm after 530 and 1000 nm excitation were compared.

Table 4.1. Fitting parameters for fs- and ns-OTA results. ^{r}Superscript denotes rising component.

Pump (nm)	Probe (nm)	τ_1, ps (A_1,%)	τ_2, ps (A_2,%)	τ_3, μs (A_3,%)	τ_4, μs (A_4,%)
1000	608	31.7 (100)^r		0.64 (74.2)	9.2 (25.8)
	580	31.7 (43.3)		0.64 (42.1)	9.2 (14.6)
530	608	31.7 (46.2)^r	0.95 (53.8)^r	0.64 (74.2)	9.2 (25.8)
	580	31.7 (35.5)	0.45 (100)^r	0.64 (47.9)	9.2 (16.6)

Given the interpretation of the OTA spectra above, we can assign the transient species to each specific process according to the model proposed in Figure 4b. The 1000 nm excitation (hυ1) depletes the $^4A_2$(F) state accounting for the GS bleach in 520–600 and 900–1300 nm regions and populates $^4T_1$(F) excited state accounting for the instantly formed broad absorption at >605 nm. The latter can be assigned to the photoinduced absorption of $^4T_1$(F) state, which quickly decays to form the long-lived intermediate state (IMS) featured by the absorption bands centered at 525 and 605 nm. The kinetic traces at 580 and 608 nm in fs-OTA spectra can be fitted using biexponential functions, from which we obtained a short decay (580 nm) and rising (608 nm) component with 31.7 ps and a ultraslow decay component with ≫5 ns (Table 4.1). The 31.7 ps time constant can be assigned to the formation time of the IMS (Figure 4.3b). The ultraslow decay component can be accurately determined after fitting the ns-OTA kinetics (Figure 4.4f), from which we obtained two time constants of 0.64 μs (74.2%) and 9.2 μs (25.8%). The obtained amplitude weighted average time is 2.9 μs, suggesting the superlong lifetime of this IMS.

The kinetic traces at 580 and 608 nm in fs-OTA spectra after 530 nm excitation can be fitted using the same set of time constants above plus an additional rising component in each case (τ_2, Table 4.1). Because 530 and 1000 nm light excites Co^{2+} center from the same $^4A_2(F)$ to two different excited states, i.e., $^4T_1(P)$ and $^4T_1(F)$, respectively, we attribute the extra rising component (0.45 ps) at GS bleach of 530 nm excitation spectra to the relaxation process from $^4T_1(P)$ to $^4T_1(F)$, while the additional 0.95 ps time constant used in 608 nm kinetics to the formation of IMS directly from $^4T_1(P)$ state (Figure 4.3b). The ns-OTA kinetics after 530 nm excitation (not shown) can be adequately fitted using the same exponential function used in 1000 nm excitation, which further supports the formation of the same long-lived IMS regardless of the excitation of different d–d transitions.

It is interesting to note that the OTA spectra of the long-lived IMS closely match the second derivative of the GS absorption band (Figure 4.5d). The derivative-like features have been observed in inorganic and organic semiconductors and are typically attributed to the presence of local fields due to the photoinduced electron–hole separation, which modifies the optical spectra due to the Stark effect.[170-172] The derivative-like spectral feature, along with extremely long lifetime of IMS, implies that the final IMS formed in ZIF-67 film after photoexcitation might be a charge-separated (CS) state rather than a metal centered state. To test this hypothesis and identify the nature of this IMS, we used XTA, a powerful technique in capturing the intermediate electronic structure at a specific metal center,[140,173,174] to probe the IMS electronic structure at Co center.

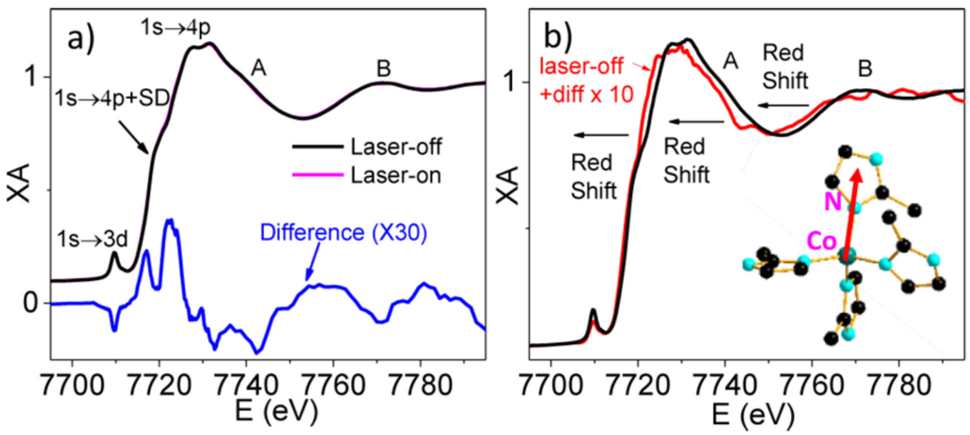

Figure 4.6. (a) XANES spectrum of ZIF-67 at Co K-edge before (laser-off) and 500 ps after (laser-on) 527nm laser excitation. The difference spectrum is obtained by subtracting the laser-off spectrum from the laser-on spectrum. (b) To better illustrate the spectral change, the laser-on XANES spectrum is regenerated after adding the difference spectrum (x 10) to the laser-off spectrum.

Figure 4.6a shows the XANES spectra of ZIF-67 before (laser-off) and after 527 nm excitation (laser-on) as well as the difference spectrum (blue curve) obtained after subtracting the laser-off spectrum from the laser-on spectrum. The laser-on spectrum was taken at 500 ps after laser pump pulse when IMS has completely formed according to the OTA results. Therefore, any transient signal observed at this time delay is directly correlated with the IMS electronic structure. As shown in the difference spectrum in Figure 4.6a, a broad positive transient absorption was observed at white-line region (7714.9–7725.3 eV) where 1s–4p shake-down[175] and 1s–4p transition[176] occurs, indicating that the edge of Co center shifts to lower energy and hence the reduction of Co center due to photoexcitation. Because Co atom and imidazolate ligand are the only two components in ZIF-67, the reduction of Co center must be accompanied by the oxidation of the ligand, which unambiguously confirm the formation of CS state with LMCT character. The LMCT nature of the IMS is further supported by the negative feature at 7709.7 eV, corresponding to the reduced intensity of pre-edge (1s–3d) transition,[168,176] where the photoinduced charge separation by LMCT reduces the number of unoccupied Co 3d orbitals and hence the possibility of 1s–3d transition.

In addition to the transient signals at white-line and pre-edge regions, noticeable spectral changes were also observed at higher energy region (A and B in Figure 4.6a). Feature A corresponds to multiple scattering processes. Feature B peaked around 7772 eV mainly comes from the single-scattering of the outgoing photoelectron from the nearest N atoms. To better illustrate the spectral changes in this region, we generated a new laser-on spectrum by adding the difference spectrum (× 10) to the laser-off spectrum. As shown in Figure 4.6b, clear red-shift is observed for B band in the laser-on spectrum (red plot) compared to the laser-off spectrum (black plot), which indicates the Co–N bond elongation after photoexcitation.

Conclusions

In summary, we examined the excited state and CS dynamics in ZIF-67 thin film using the combination of ultrafast OTA and XTA spectroscopy. OTA results clearly demonstrate the formation of an exceptionally long-lived IMS (~2.9 μs) within picosecond time scale after the photoexcitation of the spin-allowed d–d transition of Co^{2+} ion in ZIF-67. Using powerful element specific XTA spectroscopy, this IMS was unambiguously confirmed to be the CS state with LMCT character. The unusually long-lived CS state and the broad absorption in UV–vis-near IR region, along with its hybrid porous nature, strongly imply the potential application of ZIF-67 materials in photocatalysis and energy conversion. Future work on understanding the localization/delocalization properties of this long-lived CS state in ZIF-67 framework is essential to facilitate these applications, which is covered, in part, in the following section.

4.2 The Nature of Long-lived Excited State in Zeolitic Imidazolate Frameworks

Introduction

Results in the previous section demonstrated that photoexcitation of Co^{2+} d-d orbitals in ZIF-67 results in a shift in electron density from the 2-methylimidazole organic linker to the Co^{2+} metal node, resulting in a charge separated state with LMCT character that possesses a 2.9 μs lifetime.[177] The long lifetime and spectral features observed in optical transient absorption (OTA) experiments point to a charge separation mechanism in ZIF materials that prevents recombination of the photogenerated carriers, i.e. the local charge separated state where photogenerated Co^{1+} and oxidized 2-methylimidazole are directly adjacent to one another must convert to a non-local charge separated state.

Because the metal ions in ZIFs are bridged in a crystalline network, there have been investigations into the electronic band structure of ZIFs as semiconducting materials.[178-180] In this scenario, the metal ions might be viewed as part a continuous band that would allow charge migration if continuous wavefunction overlap is present in the system.[181,182] If wavefunction overlap is poor or discontinuous, a hopping mechanism might dominate and would lead to poorer mobility.[183] While either case is a possibility, the conductivity of Zn- and Co-based ZIFs have been measured previously by electrical impedance spectroscopy[181,184] where it was found that Co^{2+} ZIFs have significantly improved conductivity and pseudocapacitive behavior compared to highly resistive closed-shell Zn^{2+}-based ZIFs, even for those that are isostructural and differ only by the metal ion. This result implies that the metal ion plays an important role in charge transport in ZIFs and supports the existence of a mechanism for charges to separate regardless of if they are photogenerated or generated by electrochemical means.

Given these previous ZIF studies, we hypothesize that metal to metal charge transfer (MMCT) is a viable mechanism for photogenerated carrier transport in ZIFs that results in the formation of a charge separated state with long lifetime. To investigate if metal to metal communication is indeed present in ZIFs, time-resolved optical spectroscopy techniques such as optical transient absorption (OTA) are an ideal choice, as they are able to generate and track the fate of carriers to gain insight into their dynamics. If multiple metals are present in the system, OTA can be used in combination with X-ray transient absorption spectroscopy (XTA) to selectively probe the oxidation state and structure of different metals in a mixed-metal system. With these time-resolved techniques, in the following sections we investigate the possible existence of an MMCT mechanism using three model systems: 1) spatially restricted single unit model; 2) Co:Zn mixed metal ZIF; and 3) Cu-doped ZIF-67.

Results and Discussion

Single Unit Model

One possible method to study charge separation in ZIF-67 is to spatially restrict diffusion of the photogenerated charge characters by spectroscopically investigating small clusters or, optimally, a single Co[2MIM]$_2$ tetrahedron. If the diffusion of carriers is limited, it is then expected that recombination rate would be significantly faster than in the extended structure MOF. Synthetically, it is difficult to restrict growth of ZIF-67 framework while ensuring that Co is coordinated fully by four 2-methylimidazole ligands. In the ZIF-67 structure, 2-methylimidazole (2MIM) bridges two Co atoms together via its N groups and, as such, polymerization will occur when Co and 2MIM are present in solution. One viable strategy to prevent polymerization and MOF growth is to block one of the N groups on 2MIM such that only one N can coordinate to Co. Commercially available 1,2-dimethylimidazole (DMIM) was chosen to attempt the preparation of a single-unit ZIF model system $[Co(DMIM_4)]^{2+}$ by mixing Co^{2+} nitrate hexahydrate and DMIM in MEOH. Stoichiometric mixtures of Co and DMIM give a light purple color as the saturatively coordinated $Co(NO_3)_2\cdot(H_2O)_6$ octahedral species (pink in color) begins to coordinate instead to the DMIM ligand. By using a large excess of ligand, a maximum coloration of the solution is obtained indicating that equilibrium has shifted to the tetrahedrally coordinated $[Co(DMIM)_4]^{2+}$.

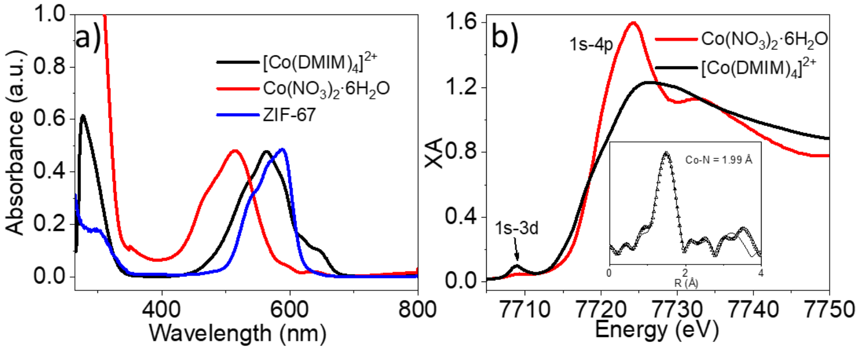

Figure 4.7. UV-Visible spectra in methanol (a) normalized to visible Co d-d transition peak, ZIF-67 spectrum was collected in reflectance mode using dry powder. Co K-edge XANES spectra for $[Co(DMIM)_4]^{2+}$ and $Co(NO_3)_2{\cdot}6H_2O$ (b) and Fourier-transformed EXAFS spectrum (inset) of $[Co(DMIM)_4]^{2+}$ with FEFF best fit.

Due to the equilibrium nature of $[Co(DMIM_4)]^{2+}$ formation, it is imperative to verify that the structure about Co is indeed tetrahedral, as suggested by the color change. The normalized UV-Visible spectra (Figure 4.7a) show that Co coordinated to either 2MIM (ZIF-67 MOF) or DMIM ($[Co(DMIM)_4]^{2+}$) has red-shifted absorption in comparison to the octahedral $Co(NO_3)_2{\cdot}6H_2O$ spectrum due to the lower ligand field splitting energy in the tetrahedral geometry. While the UV-Visible shift and similar peak position to ZIF-67 Co d-d transition suggest that $[Co(DMIM)_4]^{2+}$ has tetrahedral coordination, it does not confirm the coordination environment, which was further characterized by X-ray absorption spectroscopy (XAS). Figure 4.7b shows the comparison of $[Co(DMIM)_4]^{2+}$ and $Co(NO_3)_2{\cdot}6H_2O$ precursor Co K-edge XANES spectra. Both spectra display the prominent 1s-4p absorption onset, however, the strong white line transition in $Co(NO_3)_2{\cdot}6H_2O$ is reduced significantly after coordination to DMIM and, additionally, the shoulder structure on the edge for $[Co(DMIM)_4]^{2+}$ is absent in $Co(NO_3)_2{\cdot}6H_2O$; both of these differences suggest lower order coordination in $[Co(DMIM)_4]^{2+}$. Finally, the 1s-3d pre-edge transition is only present in $[Co(DMIM)_4]^{2+}$, suggesting that coordination with DMIM removed the center of inversion, which leads to the conclusion that $[Co(DMIM)_4]^{2+}$ is indeed tetrahedral. The first-shell Co-N distance fit to an identical distance for ZIF-67 of 1.99 Å and further confirmed tetrahedral coordination of Co (inset of Figure 4.7b).

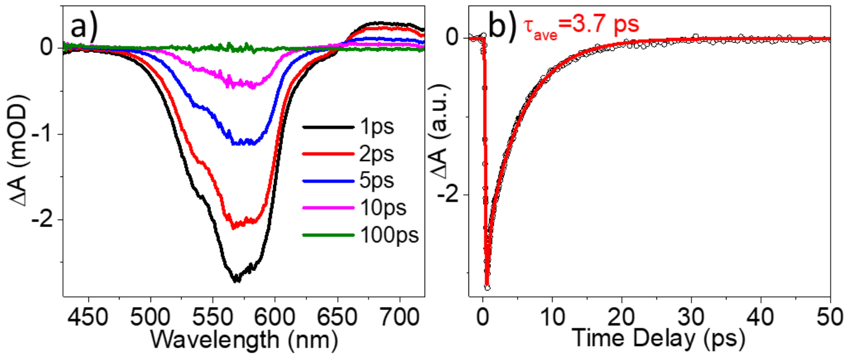

Figure 4.8. OTA spectra for $[Co(DMIM)_4]^{2+}$ after 1000nm excitation (a) and kinetic decay of 575nm GSB feature with biexponential fit (b).

With the confirmation that $[Co(DMIM)_4]^{2+}$ is indeed a tetrahedral complex and an appropriate model of ZIF-67 single unit, optical transient absorption spectroscopy (OTA) was used to investigate the photodynamics of $[Co(DMIM)_4]^{2+}$ after excitation of the lower lying $^4A_2(F)$-$^4T_1(F)$ transition using 1000nm pump pulses. The OTA spectra (Figure 4.8a) show a broad GSB that agrees with the steady state absorption spectrum of $[Co(DMIM)_4]^{2+}$ as well as a positive absorption feature centered at 700nm that is assigned to excited state of $[Co(DMIM)_4]^{2+}$. The features decay through an isosbestic point at <100ps, which suggests that there is fast recombination of photogenerated carriers. The kinetics of the GSB in Figure 4.8b show an amplitude-weighted time constant of 3.7 ps. Astonishingly, this time constant is 6 orders of magnitude faster than decay of ZIF-67 transients after excitation of the Co d-d orbitals (2.9 μs). This finding suggests that the long lifetime of ZIF-67 charge separated (CS) state is indeed dependent on extended MOF structure and might validate the presence of photogenerated charge carrier migration in the ZIF structure via MMCT or some other mechanism. In the following sections, we experimentally investigate the MMCT phenomenon in ZIF-67 materials via various spectroscopic techniques by metal doping strategies.

Co:Zn Mixed-Metal ZIF

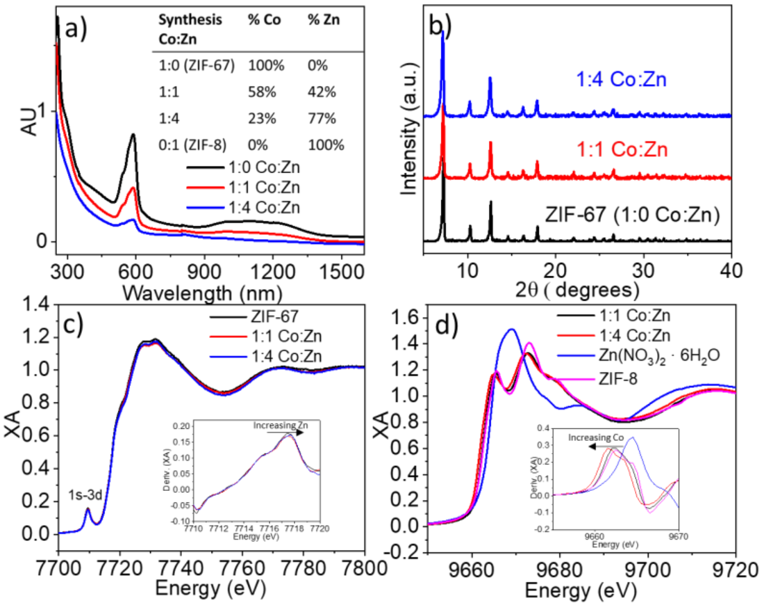

Synthesis Co:Zn	% Co	% Zn
1:0 (ZIF-67)	100%	0%
1:1	58%	42%
1:4	23%	77%
0:1 (ZIF-8)	0%	100%

Figure 4.9. Mixed-metal ZIF films UV-Visible spectra (a) and pXRD patterns (b) of Co:Zn mixed-metal ZIF at different metal ratios. Inset of (a) displays ICP-MS results corresponding to the synthesis ratios shown in the figure legends. XANES region spectra at Co K-edge (c) and Zn K-edge (d) for the mixed-metal ZIFs and $Zn(NO_3)_2 \bullet 6H_2O$ control sample with first derivative spectra insets.

ZIF-67 and ZIF-8 are isostructural ZIFs that differ by the metal ion nodes in the structure (Co^{II} or Zn^{II}, respectively). As such, it is facile to prepare a mixed-metal Co/Zn ZIF by simply varying the concentrations of Co and Zn in a methanolic mixed-metal ion precursor solution. As shown by the inset of Figure 4.9a, the synthetic molar ratios of Co and Zn correspond closely to the actual metal percentages measured by ICP-MS, where

Co composition is slightly higher than Zn in the mixed-metal ZIFs. The UV-Visible spectra (Figure 4.9a) show that the intensity of Co d-d transition features decreases with increasing amounts of d10 Zn, as ZIF-8 (Zn and 2-MIM) has no light absorption in the visible region. Additionally, the pXRD patterns (Figure 4.9b) show no changes as Zn in incorporated into the structure, confirming that SOD topology is maintained.

To investigate the local structure of the mixed-metal ZIFs about their metal centers, steady state X-ray absorption (XAS) spectroscopy was performed at the Co and Zn K-edges. Figure 4.9c shows the comparison of Co K-edge spectra showing that there is negligible change in the local structure about Co due to no change in the shape of the XANES region. The first derivative inset of Figure 4.9c, however, indicates that there is a slight shift in the Co K-edge to higher energy in the 1:4 Co:Zn sample, implying a decrease in the electron density of Co center when high amounts of Zn are incorporated into the structure.

The Zn K-edge spectra are compared to the octahedral $Zn(NO_3)_2 \cdot 6H_2O$ control sample in Figure 4.9d. While neither octahedral nor tetrahedral Zn^{II} centers are expected to show a forbidden 1s-3d pre-edge feature due to d10 electronic configuration, there is a distinct difference in the white line intensity of the 1s-4p absorption edge that has been previously ascribed to decreased p-character of the unoccupied ligand field states that participate in the white line transition for the tetrahedral geometry in comparison to the octahedral geometry.[185] The XANES region shows negligible difference between the mixed metal ZIFs. In the first derivative comparison of the XANES region (Figure 4.9d, inset), we observe the opposite change that was observed at the Co K-edge; increased Co composition results in a pronounced shift of the Zn K-edge to lower energies, corresponding to increased electron density on Zn center. Together, the Co and Zn derivative shifts show that some degree of electron density is shifted from Co to Zn in the composite mixed-metal structures. More generally, this implies that there may be electronic interaction between the metal centers in the ZIF structure, which is prerequisite to any charge-transfer interactions that might be observed.

The possibility of electronic interaction between Co and Zn metal nodes in the ZIF structure necessitated investigation of the photodynamics of Co:Zn ZIF after Co d-d excitation. Following the established scheme for ZIF-67 photodynamics[177] two different Co d-d excited states can be accessed by exciting the visible region (ca. 500-600nm) $^4A_2(F)$-$^4T_1(P)$ transition or the NIR (ca. 1000-1400nm) $^4A_2(F)$-$^4T_1(F)$ transition. Because the different energy levels of the excited states might result in different interactions with neighboring non-Co metal atoms, we excited both Co d-d transitions at 530nm and 1000nm and tracked the time-resolved photodynamics via optical transient absorption spectroscopy (OTA).

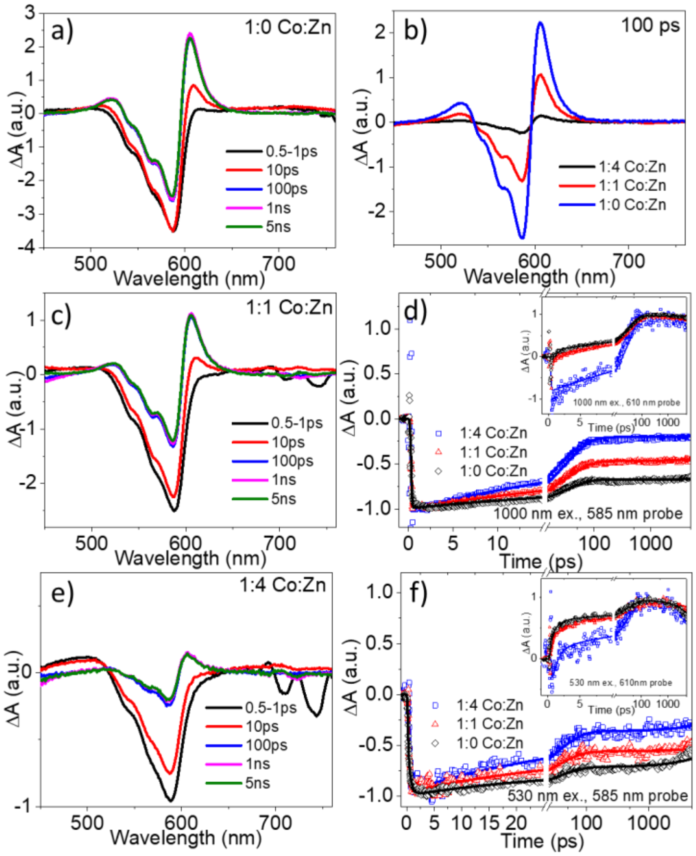

Figure 4.10. OTA spectra for different Co:Zn mixed-metal ZIFs (a,c,e). The comparison of spectra at 100ps delay time (b). Kinetic trace comparison of 585nm GSB feature (d) and 610nm stark feature (inset) after 1000nm excitation and after 530nm excitation (f and inset of f).

The OTA spectra for Co:Zn thin films on quartz are shown in Figures 4.10 a,c,e. For all three samples, we observe two main features in the spectra, namely the 585nm GSB that results from depleted ground state population after photoexcitation and the positive, derivative shaped positive excited state (ES) feature at 610nm that is assigned as a stark feature due to the presence of a charge-separated state in the material. There is additionally a weak, broad absorption feature on the red-side of the stark feature that is assigned to an excited state feature that decays through an isosbestic point with the stark feature growth and is assigned to excited state absorption after Co d-d excitation. The comparison of the spectra at 100 ps time delay (Figure 4.10b) suggest that the same spectral shape is present after the relaxation processes at earlier times for all Co:Zn ratios. Traces of the kinetics at 585nm GSB after 1000 nm excitation (Figure 4.10d) show, however, that there is significantly faster recovery of the ground state that is correlated with an increased amount of Zn in the structure. Additionally, the Stark feature (Figure 4.10d, inset) at 610nm shows a weaker trend that the growth component appears to be slowed in the presence of Zn. The same trends are observed in the 530 nm excitation spectra and the kinetic traces of the same features (not shown).

Best fits to the kinetic traces were accomplished using a multiexponential model that we have described previously that involves a bi-exponential fit for the 1000nm excitation data and a tri-exponential fit for the 530nm excitation data that includes the additional time constant for relaxation of the $^4T_1(P)$ state to lower-lying states. These time constants are shown in the scheme in Figure 4.3b. Examination of the changes in the GSB kinetic decays with 1000nm excitation (Figure 4.10d) with different Co:Zn ratios shows an interesting qualitative observation; the enhanced decay with increasing Zn appears to occur with a very similar time constant, which implies that the amplitude of the decay must be enhanced with increasing Zn content. Indeed, allowing the time constants to fit for 585nm GSB and 610nm ES feature yielded similar time constants that followed no apparent trend with changing Zn content. As a result, the multiexponential model was used to fit the data with time constants fixed to the same value as ZIF-67 decays. For 1000nm excitation, this includes τ_2 of 31.7ps corresponding to relaxation of $^4T_1(F)$ excited state to the CS state with LMCT character and τ_3 of >>5ns that corresponds to additional decay components outside the time range of our transient absorption setup on the μs timescale. For 530nm excitation, τ_1 corresponds to relaxation of $^4T_1(P)$ to $^4T_1(F)$ at GSB and direct relaxation of $^4T_1(P)$ to CS state in ES feature.

Table 4.2. Multiexponential fit parameters for Co:Zn TA kinetics.

Excitation	Co:Zn	Wavelength	τ_1	A_1	τ_2	A_2	τ_3	A_3
530 nm	1:4	585 nm	0.45	100	31.7	61.8	>>5ns	38.2
		610 nm	0.95	41.6		58.4		100
	1:1	585 nm	0.45	100		41.7		58.3
		610 nm	0.95	52.4		47.6		100
	1:0	585 nm	0.45	100		28.0		72.0
		610 nm	0.95	49.8		50.2		100
1000 nm	1:4	585 nm	n/a		31.7	79.9		20.1
		610 nm				100		100
	1:1	585 nm	n/a			52.6		47.4
		610 nm				100		100
	1:0	585 nm	n/a			32.2		67.8
		610 nm				100		100

The parameters from best fits are shown in Table 4.2. In the 1000nm excitation data, where only two time constants are used, it is evident in the GSB data that amplitude weight favors τ_2 over τ_3 increasingly with increasing Zn content. At the 610nm ES feature, τ_2 corresponds to growth in the transient signal and cannot be compared to τ_3. Following 530nm excitation, the same trend can be observed for τ_2 compared to τ_3 in the GSB. The growth of GSB (τ_1) cannot be compared to observe a trend. At the 610nm ES feature, the amplitudes don't show a strong trend, however it is observed that A_2 is largest for the 1:4 Co:Zn, in agreement with the kinetic traces.

In order to determine the role of Zn^{2+} in the photodynamics of Co:Zn ZIF after photoexcitation, all possible mechanisms that would result in changes of the TA kinetics must be accounted for. We can rule out energy transfer from Co^{2+*} to Zn^{2+} by energy conservation on the basis of the closed shell electronic structure of d^{10} Zn^{2+} that is corroborated by the lack of any Visible-NIR features beyond the UV region for ZIF-8, the isostructural 0:1 Co:Zn ZIF. If electron or hole transfer to the Zn^{II} atom following Co^{2+} atom excitation occurs, the expected kinetic trends in the GSB would be enhanced decay for electron transfer and delayed or unaffected decay for hole transfer. Since enhanced GSB decay is observed with increasing Zn content electron transfer could be a viable mechanism, however it is noted that the standard reduction potential for Co^{2+} is nearly 0.5V positive of Zn^{2+}, so it is unlikely that electron transfer from Co^{1+*} (the reduced Co^{1+} species formed directly after CS occurs) to Zn^{2+} neighbor would occur when there are more easily reduced Co^{2+} neighbors present. Additionally, because of the energetic differences, it is likely that electron transfer from Co^{1+*} to Zn^{2+} would result in a different time constant than Co^{1+*} to Co^{2+}, which was not observed with change in Co:Zn ratio.

Thus, if for the sake of argument, the assumption is made that MMCT is a viable mechanism for CS in ZIF-67, it can be speculated that Zn^{2+} is not participating in the mechanism due to its redox potential. Rather, it is blocking MMCT from occurring. In the ZIF-67 structure, Co has four nearest neighbor metal atoms linked to its 2-methylimidazole linkers. If a statistical number of these nearest neighbors are Zn^{2+}, it could lead to decreased CS efficiency since the available number of MMCT channels is decreased. If this is true, a correlation between the fraction of Zn^{2+} present in the structure and the quantified parameters by OTA fitting should exist. Indeed, if we compare the amplitude of τ_2 for the GSB feature, the decay time constant that corresponds to charge separation, to the fraction of Zn^{2+} present in the structure, we find a linear correlation in both 1000nm and 530nm excitation data (Figure 4.11a).

Interestingly, the slope of the lines (the degree to which inclusion of Zn affects the decay amplitude A_2 that we assign as MMCT efficiency) is different for the different excitation wavelengths (0.62 for 1000 nm and 0.44 for 530 nm). The y-intercept shows that for 1:0 Co:Zn, there is less GSB decay for 530nm ex. due to the direct formation of IMS from $^4T_1(P)$. Evidently, this pathway is less affected by the presence of Zn (A_1, 610nm) than A_2, so it is feasible that this fast 0.95ps process constitutes a larger portion of CS (i.e. a larger amount of A_3 is due to A_1 process instead of A_2 process) which results in less change in A_2 with increasing Zn content for 530nm excitation compared to 1000nm excitation. These assignments make conceptual sense because if Zn blocks MMCT from occurring, then CS processes compete with the relaxation of Co d-d excited state to the ground state, causing the kinetic trends discussed. Finally, supporting this assignment that charge separation is retarded with Zn incorporation, the GSB-normalized spectra compared at 100ps show that the stark feature intensity decreases with increasing Zn content (Figure 4.12).

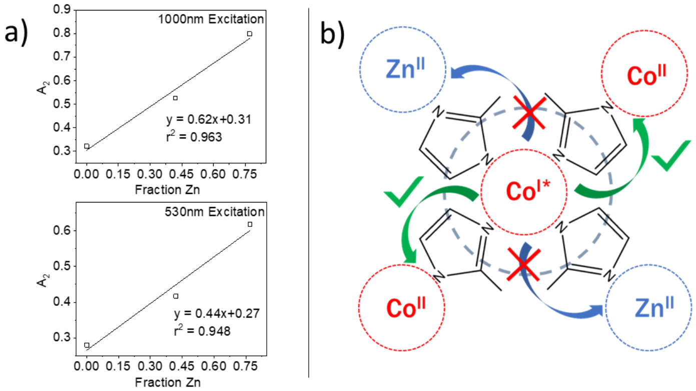

Figure 4.11. (a) The amplitude of τ_2 (A_2) at 585nm GSB feature following 1000nm (top) and 530nm (bottom) excitation correlated to the fraction of Zn in Co:Zn ZIF. (b) Cartoon model depicting MMCT from Co^{1+*} to neighboring metal ions in 1:1 Co:Zn ZIF. The arrows (representing MMCT) indicate MMCT is possible to Co^{2+} atoms but not Zn^{2+} atoms. The dashed circle represents positive charge after charge separation located on any one of the ligands around the central absorbing Co atom.

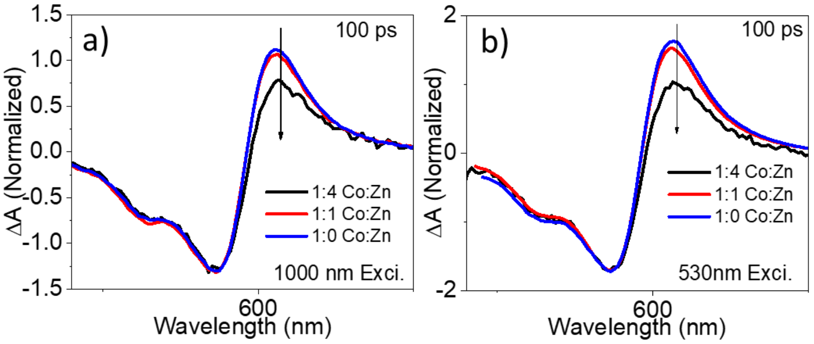

Figure 4.12. Comparison of TA spectra at 100ps for 1000nm excitation (a) and 530nm excitation (b). The GSB feature is normalized to account for the difference in Co concentration in each sample. The comparison of stark feature intensity supports the conclusion that charge separation is retarded with incorporation of Zn into the structure.

The cartoon model outlining this process is shown in Figure 4.11b. Depicted in the cartoon is the transient intermediate state directly after CS event in which electron density has shifted from 2-methylimidazole to the absorbing excited state Co^{2+*} in the center of the cartoon. The dashed circle represents the positive charge that could be localized on any of the four 2-methylimidazole ligands. While the Co:Zn ZIF photophysical studies support the existence of MMCT in ZIF-67 structure and complement the spatially restricted model, the evidence is only indirect. In the following section, we instead consider a mixed-metal ZIF that incorporates a non-closed-shell transition metal with the intent of observing changes at one metal when the d-d transition of the other metal is selectively excited.

Co:Cu Mixed-Metal ZIF

Various first-row transition metals of the +2 oxidation state have been doped into the ZIF-8 or ZIF-67 structure, such as Fe,[186] Ni,[165] and Cu[187,188]. Of these dopants, we chose Cu^{2+} because of its relatively positive reduction potential with the intent of using

Cu^{2+} dopant as a spectroscopic probe for MMCT. The highest doping density reported for Cu^{2+} was 8.54% of metal ions using methanolic synthesis precursors.[188] We first developed an aqueous synthesis procedure that allowed us to obtain up to a 17% Cu composition for ZIF-8 (CuZIF-8) and 15% Cu composition for ZIF-67 (CuZIF-67) since high Cu content was a prerequisite for photophysical studies. These percentages were determined via EDS.

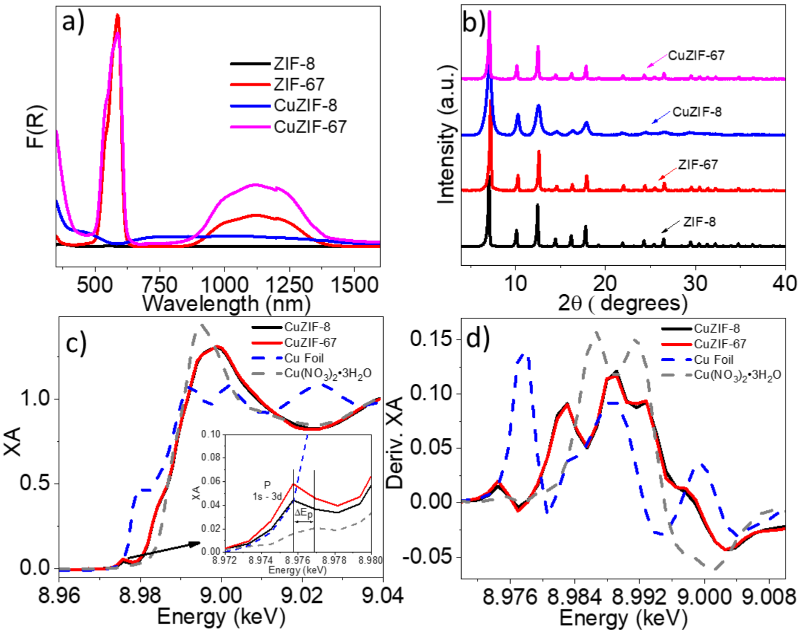

Figure 4.13. The reflective Kubelka-Munk spectra (a) and pXRD patterns (b) for Cu-doped and undoped ZIF samples. The Cu K-edge XANES spectra (c) of CuZIF samples and reference samples and first derivative of the XANES spectra (d). Inset of (c) is the enlarged pre-edge region.

The successful Cu doping of ZIF results in an observable color change for both CuZIF-8 and CuZIF-67 due to the d-d transitions of the dopant Cu atom. By inserting Cu into Zn-based ZIF-8, which is pure white color, the Cu d-d transitions are observable by reflective UV-Visible spectroscopy (Figure 4.13a) since ZIF-8 has no absorbance in the visible/NIR. Two broad absorbance bands are observed in the visible/NIR region from

400nm to 580nm and from 600nm to 1600nm for CuZIF-8. These bands are assigned to Cu d-d transitions and have reasonable agreement to a tetrahedral Cu^{2+} molecular complex reported previously.[189] Notably, there is little absorbance in the region from 580nm to 600nm, where the Co d-d transitions are at their maximum intensity as seen by ZIF-67 spectrum. The CuZIF-67 displays the typical Co d-d bands with additional weak, broad absorbance in the 400-500nm and NIR regions. The pXRD patterns (Figure 4.13b) confirm that incorporation of Cu does not result in changes to the SOD-topology bulk structure of ZIF-8 or ZIF-67. It is noted, however, that significant broadening of the pattern features are observed in CuZIF-8 that is likely due to crystallite grain size.

Although the bulk structure and UV-Visible results together imply that Cu is incorporated into the structure, they do not definitively verify that Cu occupies the tetrahedral Co or Zn sites in ZIF-67 or ZIF-8 respectively, an important prerequisite for MMCT studies. To selectively probe the local structure of Cu atoms in the ZIF, XAS was performed at Cu K-edge. Figure 4.13c shows the XANES spectra for the Cu-doped ZIFs in solid lines and two control samples in dashed lines, Cu foil and $Cu(NO_3)_2 \cdot 3H_2O$. First, it is evident that all of the spectra are shifted to higher energy with respect to Cu foil, indicating the presence of Cu ion. The shape of the XANES edge and peak corresponding to the 1s-4p transition are also very different between the ZIF samples and $Cu(NO_3)_2 \cdot 3H_2O$ along with the above-edge oscillations, indicating a different coordination environment in ZIF compared to the saturatively coordinated Cu salt. Hydrated $Cu(NO_3)_2 \cdot xH_2O$ salts form square planar complexes in the first coordination shell about Cu (Cu-O, 1.92-2.02 Å) and extended distance (≈ 2.35 Å) coordination to axial O atoms.[190] Thus, the geometry can be considered square planar or axially-extended octahedral. Square pyramidal, trigonal bipyramidal, and square pyramidal complexes are common for Cu^{2+}, whereas tetrahedral environments are uncommon.[189] Therefore, carefully determining the coordination in the CuZIF samples is important.

In-depth XAS studies have been previously performed on the copper(II) imidazole complex in aqueous solution[191] and in single crystals[192], where insights from polarized XAS support the assignments of randomly polarized XANES features, as is the case in the CuZIF XANES data. Polarized studies on the square planar $Cu[IM_4]\cdot 2NO_3$ complex revealed that polarization parallel to the axial (non-imidazole) ligands (1s-$4p_z$) showed two prominent features at approximately 8.987 keV and 8.993 keV while powdered (unpolarized) measurements give only a weak shoulder at 9.987 keV and broad main-feature at 9.993 keV similar to polarization perpendicular to axial ligands, which show less prominent shoulder. For the randomly polarized measurement of $Cu(NO_3)_2\cdot 3H_2O$, only a prominent, broad feature is observed in agreement with calculated axially elongated octahedral results for $Cu[IM_4]\cdot 2H_2O$.[191]

For the CuZIF samples there is a shoulder feature on the edge at 8.984 keV and the main feature at 8.995 keV is broad. These features are in agreement, with some intensity discrepancy, with the randomly polarized square pyramidal $Cu[IM_4]\cdot H_2O$ determined in aqueous solution[191] and polarized (1s-$4p_{x,y}$) spectra for $Cu[IM_4]\cdot 2NO_3$ crystals.[192] However, unlike the square planar variants, for the tetrahedral geometry, it is expected that the energy of $4p_{x,y,z}$ are degenerate.[193] Therefore, the shoulder at 8.984 keV observed cannot be explained as contribution from (1s-$4p_z$) if the geometry in CuZIF is indeed tetrahedral, but rather has been explained as a 1s-4p transition shakedown transition by comparing its intensity to the covalency of ligands in Cu^{II} complexes.[193]

Thus, due to similarity in the 1s-$4p_z$ features in square planar complexes and the shakedown transition feature in some Cu^{II} systems, it is difficult to discriminate between these possible geometries based on XANES profile alone.

The strong evidence that CuZIF contains a tetrahedral Cu center is shown by the enlarged pre-edge region in the inset of Figure 4.12c. Compared to the axially-extended octahedral $Cu(NO_3)_2 \cdot 3H_2O$ species that contains an inversion center, both increased intensity and shift to lower energy are observed for the CuZIF samples. Because the pre-edge feature is due to the 1s-3d transition, the increased intensity implies a loss in the inversion center. Additionally, the ~ 1 eV shift in pre-edge position (ΔE_p) to lower energy indicates lower energy of partially-occupied Cu d orbitals, the final state in the 1s-3d transition, due to decreased ligand field splitting strength. The position of the absorption edge is compared in the first derivative spectra in Figure 4.12d. The synthesis precursor Cu^{2+} salt, $Cu(NO_3)_2 \cdot 3H_2O$, and CuZIFs have edge positions of 8.987 and 8.989 keV, respectively. Because edge energy above 8.986 keV is characteristic of Cu in the +2 oxidation state,[193] we can assign the oxidation state of Cu to +2 in the CuZIF samples, indicating no change in the oxidation state during synthesis. Finally, the extended X-ray absorption fine structure (EXAFS) data for CuZIF-67 collected at both the Co K-edge and Cu K-edge (Figure 4.14, Table 4.3) indicate, both qualitatively and quantitatively, very similar structure about Co and Cu in the same sample, confirming the conclusion that Cu replaces Co sites in the sample without disrupting the local structure.

Table 4.3. Parameters for CuZIF-67 EXAFS fits.

Vector	Co K Edge			Cu K Edge		
	N	σ^2 (Å^2)	R (Å)	N	σ^2 (Å^2)	R (Å)
N	4	0.007	2.00	4	0.007	1.96
C	8	0.01	2.92	8	0.01	2.88
N-C	8	0.006	2.97	8	0.01	2.92
N-C	8	0.006	3.02	8	0.01	2.97
C (methyl)	4	0.01	3.47	4	0.01	3.28

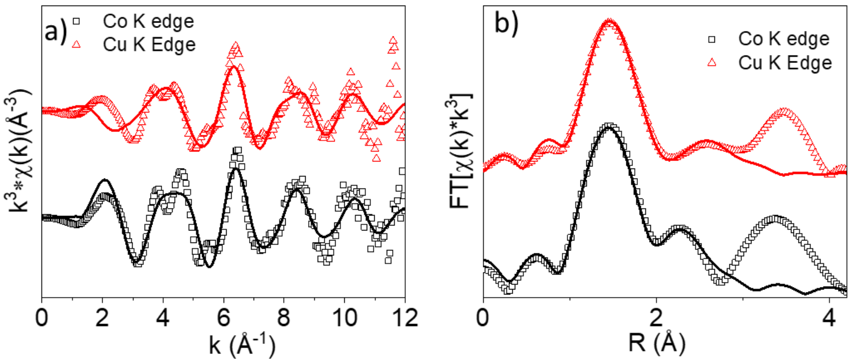

Figure 4.14. The EXAFS spectra in K space (a) and R-space (b) with open points as data and solid best fit lines using FEFF model in Table 4.3.

Because Cu cannot be incorporated into ZIF-67 at a broad range of compositions as with Co:Zn ZIF, there are limitations on the photophysical studies via OTA since a maximum Cu content of 15% can be incorporated into ZIF-67. Additionally, due to the broad absorbance spectra of Cu d-d transitions (Figure 4.13a), it is difficult to selectively excite Co without exciting Cu while still observing the spectral features from Co metal center. For instance, if 590nm excitation is used, which directly overlaps Co metal center absorbance and is at a minimum in Cu metal center absorbance, scattered pump light from the thin film samples will render the Co-centered features untraceable. Since Co metal center has no absorbance at 400nm, it is, however, feasible to selectively excite Cu without exciting Co. These considerations are taken into account in the following optical studies that focus on the changes observed at one metal center when the other is excited.

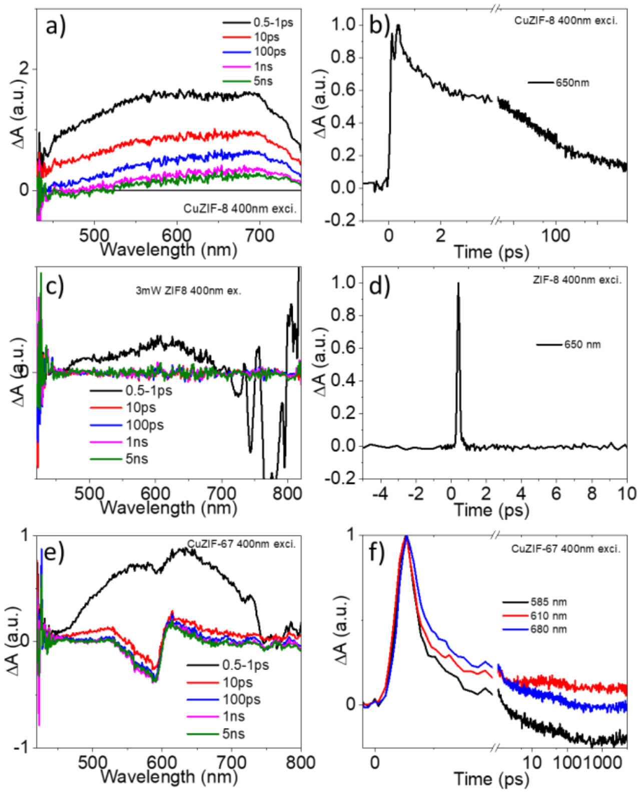

Figure 4.15. OTA spectra for CuZIF-8 (a), ZIF-8 (c), and CuZIF-67 (e) after 400nm excitation and their respective kinetic traces (b,d, and f). Note that for ZIF-8, the transient difference observed at early time is a substrate interaction that decays within instrument response, as shown by the kinetics in (d). For CuZIF-8, the broad positive feature decays to approximately 20% within the available time window. For CuZIF67, it is observed that the broad Cu feature decays quickly to give the typical Co signals, ending with a spectrum very similar to direct excitation of ZIF-67 using 530 or 1000nm pump. We note that ZIF-67 gives no transient signals under these experimental conditions, implying that Cu excitation plays a role in the formation of Co-centered features.

When Co, the primary metal component in CuZIF-67, is excited using either 530nm or 1200nm excitation, there are no changes observed in the OTA spectra or kinetic traces of the transient features. Because both metal centers should be excited at this wavelength, it is difficult to draw conclusions without the spectra for the direct excitation of Cu. To observe the transient spectra for Cu excitation, CuZIF-8 was measured under 400nm excitation (Figure 4.15). While the photodynamic processes in CuZIF-67 are likely different from CuZIF-8, the CuZIF-8 sample gives insight into the transient features of Cu embedded in an “inert” matrix, as suggested by Co:Zn results. It was confirmed that ZIF-8 alone gives no transient signal under these conditions (Figure 4.15c-d). When Cu was selectively excited in CuZIF-67 (Figure 4.15e-f) using 400nm pump pulses, a condition that gives no transient signal for undoped ZIF-67, the observed Cu features decay quickly to give features similar to directly excited Co features. Because of difficulty in assigning the Co features to reduction or excitation that has been discussed previously[194] these observations imply some interaction between Cu and Co when Cu is selectively excited, however they cannot be assigned definitively.

The difficulty in assigning the transient differences observed from OTA can be overcome by the utilization of an element-specific time-resolved technique, namely X-ray transient absorption (XTA). Using XTA, the X-ray absorption near edge spectra (XANES) can be collected both with laser excitation (at a specified delay time after photoexcitation) and without photoexcitation. The difference between these two spectra (laser on – laser off) is then used to identify changes in the oxidation state and structure as a result of photoexcitation. While structural information can be difficult to obtain from the XANES regions, changes in oxidation state, the desired information in this study, are easily identified by shift in the XANES edge energy.

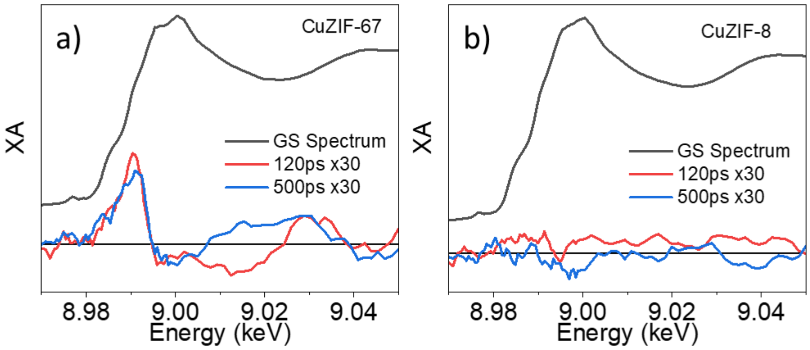

Figure 4.16. Excitation wavelength of 590 nm was used to selectively excite Co d-d transitions.

XTA experiments at the Cu K-edge were performed using 590nm excitation, where Co d-d transitions are at a maximum absorbance and Cu d-d transitions are at a minimum absorbance. We note that our previous experiments that used XTA to identify the LMCT character of intermediate state formed after Co d-d excitation also excited the visible Co d-d absorption band.[177] The role of CuZIF-8 is to act as a control sample to ensure that any differences observed in CuZIF-67 aren't due to direct excitation of Cu in ZIF environment. The Cu K-edge XTA difference spectra shown in Figure 4.16a were measured at delay times of 120ps and 500ps after photoexcitation. The positive difference feature observed at 8.99 keV that directly overlaps the 1s-4p transition edge is assigned to reduction of Cu metal center after 590nm excitation. In the control CuZIF-8 sample, no transient difference is observed, confirming that 590nm excitation does not result in oxidation state changes unless Co is incorporated into the structure.

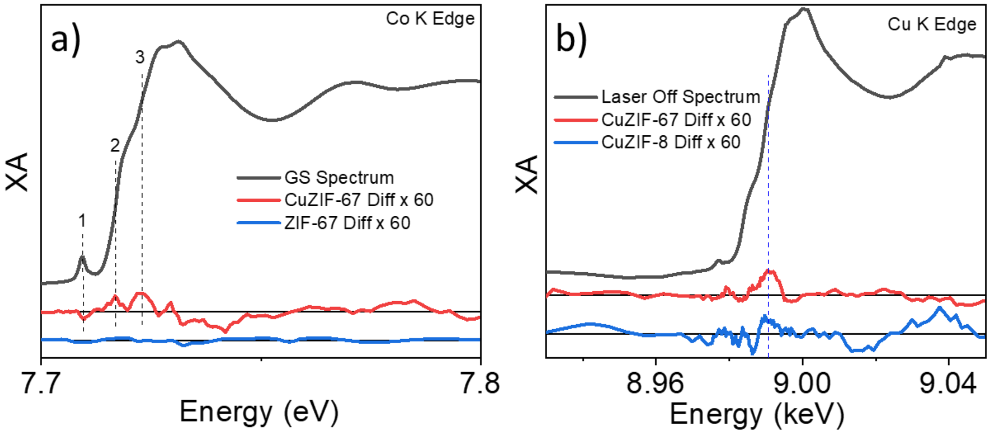

Figure 4.17. Co K-edge (a) and Cu K-edge (b) XTA spectra under 400nm excitation. At the Co K-edge in (a), the time delay between 400nm pump and X-ray probe is 1ns. In (b), the time delay is 50ps.

Using 400nm excitation, OTA experiments showed that Co d-d transitions cannot be excited in ZIF-67, however Co-centered transient signals were observed when Cu was incorporated into the structure. To investigate this result, 400nm excitation was used in XTA experiments at Co K-edge for ZIF-67 and CuZIF-67 (Figure 4.17a). Indeed, when no Cu is incorporated into the structure, negligible transient difference signal is obtained in agreement with OTA results. However, when Cu is incorporated into the structure, a distinct difference signal is observed with three main features in the edge region. The negative feature (1) is due to reduced transition probability for 1s-3d transition due to filling of the 3d orbital that was observed previously for ZIF-67.[177] This assignment is consistent with reduction of Co center after selective excitation of Cu center, as shown by the positive difference features at (2) and (3). Because the result in Figure 4.17a suggests that electron density moves from Cu center to Co center after photoexcitation of Cu d-d transition, it is expected that probing the Cu K-edge should result in the observation of oxidized Cu center. Contrarily, reduction of the Cu center is observed in CuZIF-67 after photoexcitation (Figure 4.17b). However, when CuZIF-8 is measured, a similar difference signal is obtained. Based on our previous ZIF-67 studies, however, this result is explainable because excitation of Co d-d transition in ZIF-67 results in reduced Co center. The 400nm excitation CuZIF-8 XTA experiment confirms that this same phenomenon is observed when Cu is excited in ZIF environment; formation of a charge-separated state with LMCT character occurs after Cu d-d photoexcitation. Then, it is unsurprising that the reduction signal is still observed in CuZIF-67 since XAS probes the average of all Cu atoms present. Evidently, while some Co is reduced after Cu excitation from Figure 4.17a, a majority of Cu atoms must remain reduced.

Together, these results indicate that communication between adjacent open-shell transition metals occurs after photoexcitation of metal d-d transitions. The single-unit ZIF model suggested that, without any extended ZIF structure, relaxation of Co d-d excited state is fast. From Co:Zn data, it can be inferred that, if closed-shell metals are present, charge separation is retarded. The CuZIF XTA studies directly show the presence of a charge separation mechanism that occurs between adjacent open-shell transition metals. With these insights, it is now understandable why excitation of Co d-d transition in ZIF-67 led to the formation of a long-lived charge-separated state; after the initial local charge-separation event between ligand and metal ion via an LCMT mechanism, the metal-centered negative charge is able to separate from the ligand-centered positive charge via a metal-to-metal charge separation mechanism. Beyond the scope of this study is the assignment of the exact mechanism of photogenerated carrier transport in ZIFs, and future efforts should be directed to understand whether transport occurs in a band transport mechanism or via a hopping mechanism. While the nature of MMCT in ZIFs remains unknown, this first direct evidence of metal-to-metal communication unveils new understanding of ZIF photodynamics and demonstrates the need for fundamental understanding of their properties that position them as promising photocatalytic materials.

Conclusions

The existence of a charge separation mechanism in ZIF materials was investigated using three model systems, namely a single-unit model that represented a single tetrahedral Co center, a Co:Zn composite ZIF, and Cu-doped ZIF-67. The single-unit model, which lacks the bridged metal ions present in ZIF-67, showed a 6 order of magnitude shorter lifetime in its excited state after Co d-d excitation compared to ZIF-67. Composite Co:Zn ZIFs demonstrated that Co must be adjacent to open-shell transition metals to facilitate charge separation. Cu-doped ZIFs were probed by XTA to unambiguously confirm the localization of charges on one type of metal atom after selective excitation of the other metal's d-d transitions. Together, these evidences together reveal that metal-to-metal communication exists in ZIF materials and is important for charge separation. These findings suggest importance in fundamentally understanding the mechanism of photogenerated charge transport in ZIFs in future efforts.

4.3 Photoinduced Interfacial Charge Separation Dynamics in Zeolitic Imidazolate Framework

Introduction

While exploratory works have demonstrated the potential of ZIFs in photocatalytic reactions, the roles that ZIFs play in these systems are either inert hosts or remain blurred. Our group found that ZIFs based on transition metal with unfilled d orbitals exhibit exceptional optical properties, including broad absorption bands in the UV-visible and near IR regions, with a surprisingly long-lived excited state for Co-ZIFs (Chapter 3). This suggests that ZIFs may afford facile charge separation (CS) and redox chemistry, a desirable property of heterogeneous photocatalysts. However, there have not yet been experimental reports of the CS dynamics from the excited state of ZIF materials. As fast and efficient charge transfer from excited ZIFs to substrates is essential for their application in photocatalysis, in this work, we report the first fundamental study of CS and charge recombination (CR) dynamics of ZIFs in the presence of methylene blue (MB+) as an electron acceptor. Using ultrafast transient absorption (TA) spectroscopy, we observe the reduction of methylene blue by ZIF-67 excited state following its selective excitation. This first insight into the CS dynamics of ZIF-67 will be essential toward developing ZIF materials as intrinsic light harvesting and CS materials for photocatalytic applications.

Results and Discussion

Thin films of ZIF-67 were prepared on quartz substrate following our previously established procedure.[177] Three layers of ZIF-67 were grown consecutively to give an appropriately thick, transparent film for optical characterizations. For MB$^+$ sensitized film (MB$^+$-ZIF-67), the as-synthesized ZIF-67 was immersed in a 0.1 M solution of MB$^+$ in methanol for 15 minutes and was then removed from solution and allowed to dry. For a control sample (MB$^+$-Quartz), the MB$^+$ solution was spin-coated onto quartz substrate to give a transparent film of comparable optical density with respect to the MB$^+$ on MB$^+$-ZIF-67 film.

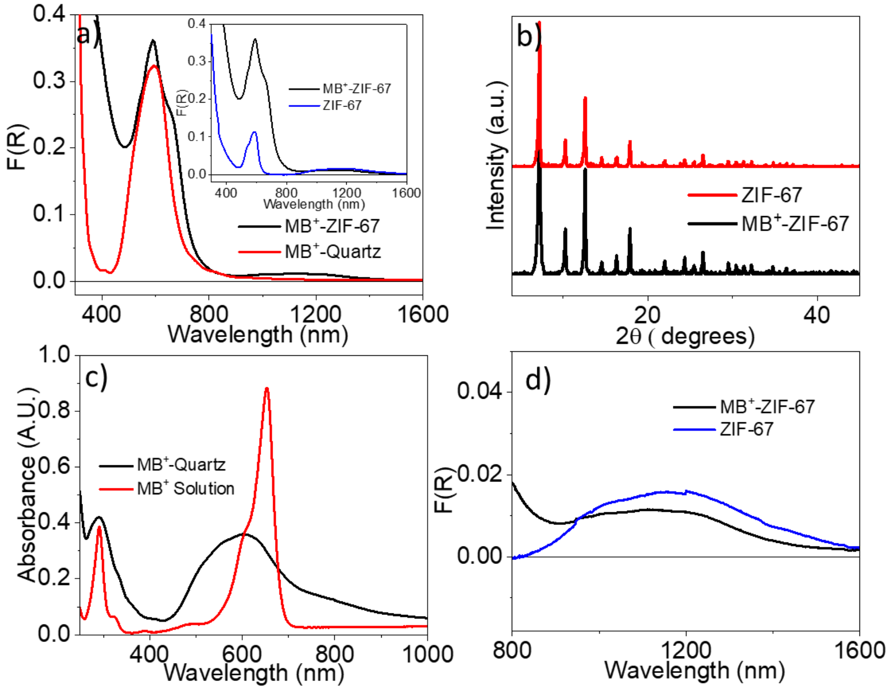

Figure 4.18. (a) UV-Visible reflectance diffuse spectra of MB$^+$ on quartz and MB$^+$ sensitized ZIF-67 films. Inset of (a) compares the UV-Visible reflectance diffuse spectra of bare ZIF-67 and MB$^+$ sensitized ZIF-67 films. (b) XRD patterns of bare ZIF-67 and MB$^+$ sensitized ZIF-67 films. (c) Comparison of MB$^+$-Quartz and MB$^+$ solution sample in MEOH. (d) Comparison of the NIR region for MB$^+$-ZIF-67 and ZIF-67.

The thin films were first characterized by diffuse reflectance UV-Visible spectroscopy (Figure 4.18a). The MB$^+$-Quartz sample (red spectrum) shows a prominent band from ~ 480-710 nm with an absorption tail into the near-IR region. The UV-Visible band observed is much broader than MB$^+$ in solution (Figure 4.18c). This phenomenon has been previously ascribed to dimerization, trimerization, or further aggregations of MB$^+$ molecules resulting in significant broadening of the UV-Visible features and the appearance of an absorption tail on the red-side of the peak.[195] In the spectra of MB$^+$-ZIF-67 film, a very similar MB$^+$ peak profile is present, indicating that MB$^+$-Quartz is an appropriate control sample. Additional features characteristic of ZIF-67 were also observed in the spectra of MB$^+$-ZIF-67. The prominent peak at 585 nm can be assigned to the higher-lying d-d transition of ZIF-67 ([^{4}A$_2$(F)–^{4}T$_1$(P)]) due to tetrahedral coordination of Co^{2+} in ZIF-67 structure.[177] The lower-lying [^{4}A$_2$(F)–^{4}T$_1$(F)] d–d transition, which has lower extinction coefficient than the higher-lying transition and much lower extinction coefficient than the MB$^+$ features, is visible at 900-1350 nm regime and is shown enlarged in Figure 4.18d. The higher-lying d-d transition in the spectrum of MB$^+$-ZIF-67 does not shift with respect to that in bare ZIF-67, indicating that the bulk structure of ZIF-67 does not change due to MB$^+$ adsorption. The unchanged structure of ZIF-67 in MB$^+$-ZIF-67 was further confirmed by XRD in Figure 4.18b, where the XRD patterns of MB$^+$-ZIF-67 resemble that of ZIF-67 and are consistent with the published SOD-topology ZIF-67 patterns.[196]

Table 4.4. TA kinetic fitting parameters with time constants τ and normalized amplitudes at selected representative wavelengths.

Sample	Probe	τ1,ps	A1,%	τ2,ps	A2,%	τ3,ps	A3,%	τ4	A4,%
ZIF-67	580	31.7	41.6	-	-	-	-	>>5ns	58.4
	608		48.2^{r}	-	-	-	-		51.8
	670		100	-	-	-	-		-
MB$^+$-ZIF-67	580		41.9	1.33	26.4	101.4	1.3^{r}		30.3
	608		42.1^{r}		36.0^{r}		14.0		7.9
	670		4.7		60.0		14.9^{r}		20.4

^{r}Rising Component

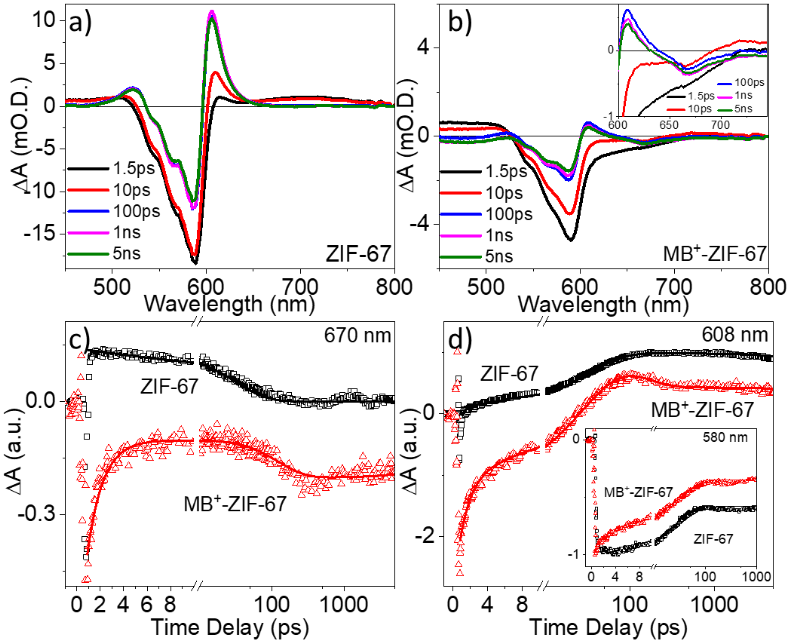

Figure 4.19. Transient absorption spectra of (a) ZIF-67 and (b) MB$^+$-ZIF-67 following 1000 nm excitation. The comparison of TA kinetics of ZIF-67 and MB$^+$-ZIF-67 at 670 nm (c), 608 nm(d), and 580 nm (inset of d). Inset of (b) shows enlarged MB$^+$ GSB region. The solid lines in (c) and (d) are the best fit lines from the global multiexponential result.

The CS dynamics in MB$^+$-ZIF-67 was investigated by femtosecond TA spectroscopy. Due to significant spectral overlap of MB$^+$ and ZIF-67 (Figure 4.18a), we are not able to selectively excite MB$^+$ or ZIF-67 in the visible spectral range. Instead, 1000 nm was used to selectively excite the lower-lying d-d transition of ZIF-67 as MB$^+$ has negligible absorption at this wavelength. This was further confirmed by the TA spectra of the control sample, i.e. MB$^+$-Quartz, which yields negligible TA signal under the same experimental conditions.

Figure 4.19a shows the TA spectra of ZIF-67 following 1000 nm excitation. The instantaneously formed negative feature centered at 580 nm and broad positive features from 450 nm to 500 nm and 650 nm to 800 nm can be assigned to the ground state bleach (GSB) of ZIF-67 and instantaneously formed excited Co d-d state ($^4T_1$) after photoexcitation that is intrinsic to ZIF-67, respectively. The Co d-d excited state features decay with time, which is accompanied by the formation of a prominent positive feature at 608 nm, corresponding to the formation of intermediate long-lived charge separated state that is consistent with our previous observations on ZIF-67 film.[177] However, distinct differences were observed in the spectra of MB+-ZIF-67 (Figure 4.19b) compared to that of ZIF-67. First, the GSB of ZIF-67 in the spectra of MB^+-ZIF-67 appears to decay faster while the growth of the positive feature at 608 nm is suppressed. Furthermore, an additional spectral feature, namely a broad negative feature, is visible from approximately 620 nm to 720 nm where it isn't overlapped by the larger ZIF-67 features. These features are highlighted in the inset of Figure 4.19b, where the region from 600 nm to 750 nm in the MB^+-ZIF-67 transient spectra is enlarged. The new negative feature observed which extends to 720 nm, is consistent with the ground state absorption of MB^+ and can thus be attributed to the GSB of MB^+. The formation of GSB of MB^+ in the spectra of MB^+-ZIF-67 can result from energy transfer or charge transfer process from the excited ZIF-67 to MB^+. Energy transfer process from ZIF-67 to MB^+ is not feasible in this system because of energy conservation; 1000 nm excitation is lower than the energy that can be absorbed by MB^+. We can also exclude the possibility of hole transfer from ZIF-67 to MB^+ as this process is thermodynamically unfeasible (MB^{2+}/MB^+ redox couple occurs at +1.105 V vs. SCE).[197,198] These results together lead us to believe that electron transfer occurs from excited ZIF-67 to MB^+, resulting in the formation of GSB of MB^+. We note that, while MB^+ signals are clearly observed, the ET event must have limited efficiency since highly efficient ET would lead to dominating MB^+-centered features. This is likely due to the heterogeneous nature of the sample (i.e. dye aggregation) as well as poor coupling between the electronic states of ZIF-67 and MB^+ due to surface contact only and the aforementioned dye aggregation.

Further evidence of ET process can be seen from the TA kinetics of MB^+-ZIF-67. As shown in Figures 4.19c and 4.19d, instead of positive amplitudes for the kinetics at 670 nm and 608 nm for ZIF-67, the kinetics of MB^+-ZIF-67 at both wavelengths initiate with negative amplitudes, which suggests the instant formation of MB^+ GSB, accounting for an ultrafast ET process from excited ZIF-67 to MB^+. The recovery of MB^+ GSB was observed at < 10 ps, which can be attributed to the charge recombination (CR) process from reduced MB^+ and oxidized ZIF-67, consistent with the enhanced GSB recovery of ZIF-67 in MB^+-ZIF-67 (inset of Figure 4.19d). Meanwhile, it is interesting to note that the GSB recovery of MB^+ stops after ~ 10 ps, which is indeed followed by the further growth of MB^+ GSB, as can be seen in the kinetic traces in Figure 4.19c and 4.19d as well as the enlarged spectral region in the inset of Figure 4.19b. We attributed this irregularity to ET from ZIF-67 to MB^+ but with different pathway, the origin of which will be discussed in next section. Different from the first ET pathway where ultrafast CR process was observed, the CR associated with this second ET process is slow (>> 5 ns).

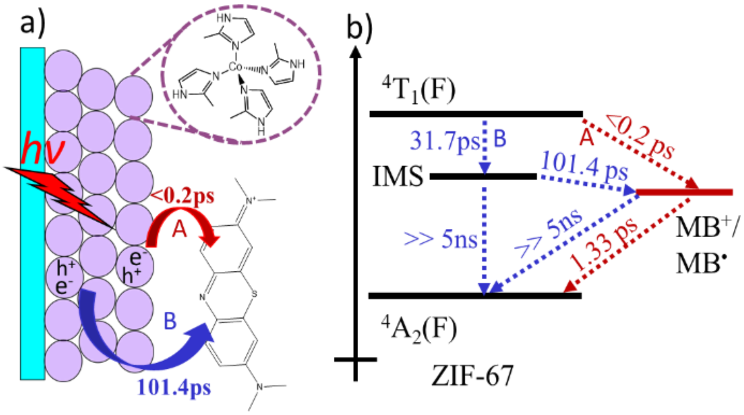

Figure 4.20. a) The proposed two-pathway electron transfer model in MB^+-ZIF-67. B) Schematic diagram depicting energetics and time constants for electron transfer dynamics in MB^+-ZIF-67.

A multiexponential model was used to fit multiple wavelengths globally across the TA probe range to quantify the kinetic trends observed (Table 4.4). The data <800 fs was excluded from the fits due to the combination of our 200 fs instrument response, coherent artifacts, and substrate effects that are visible in Figure 4.19c-d as data points above and below the baselines of the kinetic traces at early times. To facilitate discussion, the kinetic traces at 580 nm, 608 nm, and 670 nm only are shown and compared here as they are representative of the assigned processes. The ZIF-67 sample was first fit using the same time constant (τ_1 of 31.7 ps) found in our previous study at all wavelengths.[177] The 470 nm and 670 nm features, assigned to decay of ZIF-67 ES, were completely recovered by 100 ps and, thus, were fit with a single exponential. The 580 nm and 608 nm features, however, included a >> 5 ns component to account for the remaining signal at the end of our TA time window of 5 ns. The fast decay at the early time of all kinetic traces was fit with τ_2 of 1.33 ps and is assigned to recombination between some of the instantaneously generated $MB^\bullet$ and ZIF-67^+. The MB^+ GSB does not return to zero, however, indicating that some of the $MB^\bullet$ persists beyond this first recombination component, possibly due to charge separation/delocalization. As mentioned previously, a distinct growth in all kinetic features, except the ZIF-67 GSB feature at 580 nm where the remaining signal from ZIF-67 is relatively large, is present in the MB^+-ZIF-67 sample. To account for this signal growth, an additional time constant τ_2 of 101.4 ps needed to be included in the global fit model.

The evolution of TA features and the significant difference in time constants obtained can be well explained by a two-pathway model shown in Figure 4.20a. Due to their periodic nature of the ZIF-67 framework, there are two classes of $[Co^{II}(mim)_2]$ tetrahedron units: 1) the units that are located on the surface of the film and are directly in contact with MB^+ and 2) units that are in the bulk of the film and were isolated from MB^+ by the surface units. These different classes of $[Co^{II}(mim)_2]$ tetrahedron units lead to distinctly different pathways for ET to MB^+ in the MB^+-ZIF-67 system, A and B, respectively (Figure 4.20a). Pathway A is initiated by excitation of a ZIF-67 tetrahedron unit that is in direct contact or close proximity with MB^+, resulting in ultrafast ET to MB^+, followed by fast 1.33 ps recombination between $MB^\bullet$ and ZIF-67^+. Pathway B is initiated by excitation of a ZIF-67 tetrahedron unit that is not in direct contact with MB^+. Excitation results in the formation of an intermediate state (IMS) that we have previously shown to be an intrinsic charge-separated state in ZIF-67 with LMCT character.[177] We are unsure of the mechanism of charge separation within ZIF-67, which is an active area of research in our group, but it is suggested by our fundamental studies that it does occur and results in the long lifetime for photoexcited ZIF-67. The separated negative charge must then migrate to a site where it can reduce MB^+ from the long-lived IMS with a time constant of 101.4 ps. As evidenced by the lack of decay in the 670 nm kinetic trace

(Figure 4.19d) that can only be due to the GSB of $MB^\bullet$ since ZIF-67 has no signal at this wavelength at later times, recombination does not occur within our time window.

The scheme in Figure 4.20b depicts the energetics diagram inferred from the above TA results. ZIF-67 is first excited with 1000 nm light to promote an electron from the Co-centered $^4A_2(F)$ state to the Co-centered $^4T_1(F)$ state. From this state, some ET occurs from the ZIF-67 $^4T_1(F)$ state to MB^+ before our instrument response time (< 200 fs) while the remaining excited state relaxes down to the IMS with 31.7 ps time constant.[177] This 31.7 ps time constant should be unable to compete with the < 200 fs component of ET. However, as we proposed in two-pathway model (Figure 4.20a), there are ZIF-67 tetrahedron units that are not in contact with MB^+, which can prohibit the ultrafast ET event. In our previous study, the IMS has an amplitude weighted lifetime of 2.9 μs[177] and therefore does not evolve any further in the later times (>100 ps) of our TA time window. However, the additional rising component that fit with a time constant of 101.4 ps was observed and must be due to ET from IMS state to MB^+, as the evolution of ZIF-67 features after 31.7 ps component does not occur in the absence of MB^+. The two ET components are then associated with two recombination components of 1.33 ps and >> 5 ns, respectively.

While pathway A is important because it demonstrates the ability to extract an electron from ZIF-67 and provides a lower (positive) limit of -0.23V vs. SCE for the position of $^4T_1(F)$ state electrochemical potential, the existence of pathway B is particularly interesting because it demonstrates the possibility to extract electrons from a super long-lived charge separated state intrinsic to ZIF-67. This characteristic is paramount to the successful application of photocatalytic materials, provided the electrochemical potential of the material is negative enough, on an electrochemical scale, to perform useful photocatalytic reactions. The following discussion will focus on recent examples in the literature that corroborate our findings here and demonstrate the applicability of ZIF materials to photocatalytic materials.

A computational study based on periodic structure calculations indicated that Zn-based ZIF analogues with various linkers and mixed linkers all have LUCO (lowest unoccupied crystal orbital) levels negative enough to perform important photocatalytic reactions such as the proton reduction reaction and the reduction of CO_2(g) to methane or methanol.[198] When Zn was replaced with Co, it was found that the Co 3d orbital was positioned significantly more negative than the LUCO which could suggest that a charge-separated state with LMCT character in ZIF-67 would be capable of the redox activity observed in this study. A recent experimental work[127] demonstrated that a Co-based ZIF analogue with benzimidazole linkers, ZIF-9, can reduce CO_2(g) to CO(g) in conjunction with a molecular photosensitizer that reduced ZIF-9 to its anion, ZIF-9$^-$. If a corollary is made to a reduced Co center from intrinsic CS after photoexcitation, then it is feasible that photoexcited CoII-ZIF would have a similar redox potential to ZIF-9$^-$. In unpublished experiments, we have verified the ability of ZIF-67 to perform CO_2 reduction to CO under the same conditions. On an electrochemical scale vs. SCE, CO_2 reduction in aqueous media is reported to be -0.28V, -0.158V, and -0.005 V for the formation of CO (g), CH_3OH (l) and CH_4 (g) products, respectively.[199] These values compare well to the reported redox potential of MB^+ of -0.23V vs. SCE, indicating that computational and experimental works support our finding that ZIF-67 can reduce MB^+ after photoexcitation on an energetic basis.

Conclusions

In conclusion, we report that ZIF-67 can reduce MB^+ after photoexcitation. The dynamics of the ET event were characterized using ultrafast transient absorption spectroscopy after selective excitation of ZIF-67 d-d transition, which demonstrated the formation of $MB^\bullet$ on both an ultrafast (< 200 fs) timescale and on a relatively longer (101.4 ps) timescale. The ultrafast time constant is likely the ET time from the tetrahedral units located on the surface of the film that are directly in contact with MB^+, while the 101.4 ps time constant is likely attributed to ET time from the units in the bulk of the film that were isolated from MB^+ by the surface units. These results were compared with recent literature reports that corroborated the finding that the excited state redox potential of ZIF-67 is likely negative of the redox potential of MB^+, -0.23V vs. SCE. Since we have found the study of ZIF-67 via electrochemical means to be inaccessible, it is exceedingly important to pinpoint the excited state redox potential of ZIF-67 via photophysical studies. This first direct evidence of Co^{II}-ZIF photoredox chemistry strongly imply that ZIFs has large potential as intrinsic light harvesting and charge separation materials and deserve further attention to be developed as a viable and versatile photocatalyst material.

Summary

In summary, the photodynamics of ZIFs containing open-shell transition metal nodes were characterized using time-resolved spectroscopic techniques. The first system studied, ZIF-67, is based on only Co^{2+} metal nodes, giving the material a bright purple color due to the Co-centered d-d transitions. After photoexcitation, OTA and XTA experiments demonstrated a charge-separated state with LMCT character with a staggering 2.9μs lifetime.

Because this lifetime, along with direct evidence of charge separation, implies that exciton recombination is likely limited by spatial separation of the electron and hole, three model systems were prepared to interrogate the nature of charge separation in ZIFs. The single-unit model represented a system in which any photogenerated CS state with LMCT character would be unable to separate due to the lack of a 3D network. Building from this model, a mixed-metal Co:Zn system was used. In this system, it was found that closed-shell Zn^{2+} acted as an inert neighbor to Co^{2+} and inhibited charge separation through the metal nodes. Finally, direct evidence for charge separation was demonstrated via XTA experiments with the Cu-doped ZIF system, in which Cu^{2+} was reduced after selective photoexcitation of Co^{2+}. While these results do not give a mechanistic description of charge separation in photoexcited ZIFs, such as suggesting a tunneling or hopping transport mechanism, they demonstrate that MMCT is important in charge separation mechanism.

Lastly, interfacial charge separation was observed MB+-ZIF-67after selective excitation of Co d-d transitions. Interestingly, it was found that the interfacial electron transfer occurred over two distinctly different time constants, implying that the charge separated state could also participate in interfacial electron transfer. Observation of electron transfer gives insight into the electrochemical potential of ZIF-67 excited states, which were found to be reasonable well-aligned with solar fuel reactions. With these crucial insights, developments in the photocatalytic application of ZIFs with open-shell transition metal nodes will be better understood.

Chapter 5

PHOTOCATALYTIC APPLICATIONS OF ZIF-67

5.1 Mechanistic Probes of Zeolitic Imidazolate Framework for Photocatalytic Application

Introduction

Besides the early stage developments that demonstrate the promise of ZIFs as important catalytic materials, recent interests, driven by the need for solar fuel sources and environmental concerns, have extended their applications into the realm of photocatalysis. For example, after embedding photoactive species into the cavity, ZIFs have been used as photocatalysts for dye[152] and phenol[121] degradation. In the presence of photosensitizers, ZIF-9 (composed of Co^{II} and benzimidazole) has been used as photocatalysts for CO_2 reduction.[126,127] Very recently, we have also demonstrated that ZIF-67 (composed of Co^{II} and 2-methylimidazole) have intrinsic photoactivities for hydrogen evolution reaction (HER) through the formation of a long-lived intermediate state following energy transfer process from a molecular photosensitizer.[132]

While these studies certainly imply the potential application of ZIFs in photocatalysis, the catalytic activities of these systems are not impressive compared to other Co based HER catalysts.[200-202] Given the multiple advantages of ZIFs as catalysts that can provide unique means to engineer efficiency and selectivity, there is an urgent need to further develop these materials for photocatalytic applications. Progress in this endeavor clearly will require intimate knowledge of the mechanistic origins that guide light harvesting, charge separation, and HER kinetics during the photoinduced catalytic reaction, yet no experimental probes into these mechanistic functions are available to date. In this work, we report the first real-time spectroscopic study on atomic-scale mechanism of ZIF-67 that can efficiently catalyze HER in the presence of $[Ru(bpy)_3]^{2+}$ (bpy = 2,2'-bipyridine) photosensitizer. Specifically, we examined the light harvesting and charge separation dynamics using time-resolved optical transient absorption (OTA) spectroscopy, and investigated structure-function relationship of ZIF-67 under standard photocatalytic conditions using *in situ* X-ray absorption spectroscopy (XAS). Using OTA, we found that efficient electron transfer (ET) rather than energy transfer (ENT) pathway from $[Ru(bpy)_3]^{2+}$ photosensitizer to ZIF-67 is the key parameter that controls the HER efficiency. Using *in situ* XAS, we identified the key intermediate species representing the rate limiting step in HER, a problem that has long plagued the catalytic community. These results represent a new level understanding of the interplay between the microscopic and macroscopic properties of ZIF-67, paving the way for their novel application in photocatalysis.

Results and Discussion

Synthesis and Characterization of ZIF-67

ZIF-67 was synthesized according to the established method from a methanolic mixture of cobalt(II) nitrate hexahydrate and 2-methylimidazole at room temperature.[177] The violet-colored powder product was confirmed to be ZIF-67 via XRD (Figure 5.1a), which shows good agreement to the published SOD-topology ZIF-67 pattern.[203] Using this protocol, the size of ZIF-67 crystallites is ~ 300-500 nm (Figure 5.1b) with layered structure on the surface (Inset of Figure 5.1a). The as-synthesized samples can easily be suspended in solvent for catalytic application and mechanistic measurement.

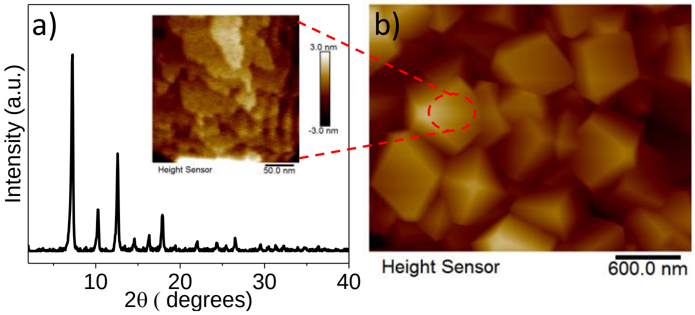

Figure 5.1. (a) Powder XRD patterns of ZIF-67. The inset shows the layered surface structure of ZIF-67 film. (b) AFM topography images of ZIF-67 thin film.

ZIF-67 for Photocatalytic HER

Table 5.1. Optimization of conditions for ZIF-67 catalyzed HER with 6 mL volume (acetonitrile + TEOA) and 3 mL headspace, using 450 nm LED illumination for 48 hours. [a]3 mL reaction volume was used to increase the head space such that H_2 concentration does not exceed GC calibration.

Optimized Reagent (Fixed Reagents)	Amount	µmoles H_2	Activity (µmol/g ZIF-67)
ZIF-67 (1.25 M TEOA, 2.2 x10^{-4} M $[Ru(bpy)_3]^{2+}$)	0	0.12	-
	1.7x10^{-2} g/L	0.854	8,540
	8.3x10^{-2} g/L	2.85	5,730
	1.7x10^{-1} g/L	5.22	5,220
TEOA (1.7x10^{-2} g/L ZIF-67, 2.2 x10^{-4} M $[Ru(bpy)_3]^{2+}$)	0	0.005	50
	0.625 M	0.443	4,430
	1.25 M	0.854	8,540
	2.5 M	0.362	3,620
$[Ru(bpy)_3]^{2+}$ (1.7x10^{-2} g/L ZIF-67, 1.25 M TEOA)	0	0	0
	1.1x10^{-4} M	0.384	3,840
	2.2 x10^{-4} M	0.854	8,540
	4.5x10^{-4} M	4.05[a]	40,500[a]

Photocatalytic performance of ZIF-67 for HER was examined upon illumination of a 450 nm LED light source in the presence of $[Ru(bpy)_3]^{2+}$ as photosensitizer and triethanolamine (TEOA) as electron donor and proton source in acetonitrile solution. The reaction conditions were systematically optimized to identify the parameters for optimum HER activity in terms of catalyst. As shown in Table 5.1, while $[Ru(bpy)_3]^{2+}$ alone can produce a small amount of H_2 (0.12 µmoles), the amount of H_2 generated significantly increases upon the addition of ZIF-67. Meanwhile, the control experiments in the dark or in the absence of $[Ru(bpy)_3]^{2+}$ or TEOA yields negligible amount of H_2, suggesting the necessity of these components in HER. A series of experiments were also carried out by varying the concentrations of ZIF-67, $[Ru(bpy)_3]^{2+}$, and TEOA (Table 4.1), as well as LED powers, from which an optimized condition, i.e. 1.7×10^{-2} g/L of ZIF-67, 1.25 M of TEOA, 4.5×10^{-4} M of $[Ru(bpy)_3]^{2+}$, and 1.02 mW of 450 nm LED power, was achieved.

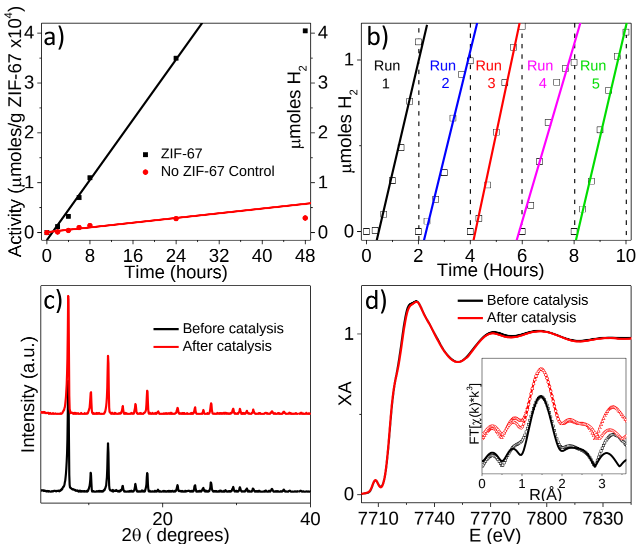

Figure 5.2. (a) The full-time profile of H_2 evolution under the optimized HER condition. (b) Recycling of ZIF-67 HER catalyst after multiple 2 hour experiments. (c) The comparison of XRD patterns of ZIF-67 before and after 5 catalytic cycles where after catalysis pattern was collected by using the same amount of ZIF-67 employed in before catalysis sample. (d) The comparison of *ex situ* XANES of ZIF-67 before and after catalysis. The inset compares the Fourier-transformed R-space data (open points) with their FEFF best fits (solid lines).

The full time H_2 generation profile measured under the optimum catalytic condition is shown in Figure 5.2a. The system produces hydrogen steadily for the first 24 hours until the catalysis ceases at 48 hours, reaching an activity of 40,500 µmoles/g ZIF-67. The ZIF-67 catalyzed HER reaction was further investigated via recycling experiments, in which the ZIF-67 catalyst was centrifuged from the catalysis mixture, washed with ACN, and redispersed in a fresh catalysis mixture after every 2 hours of photocatalysis. As shown in Figure 5.2b, the catalytic activity remains similar within 5 cycles of experiment, suggesting that the catalyst is recyclable and remains active for at least 10 hours, consistent with the full-time profile experiment above.

The cease of catalysis can be attributed to the degradation of $[Ru(bpy)_3]^{2+}$ as ZIF-67 retains its integrity while degradation of $[Ru(bpy)_3]^{2+}$ was observed after catalysis. First, we observed that the original orange colored $[Ru(bpy)_3]^{2+}$ in the system turns red-brown after being exposed to 450 nm LED light and the time-frame of this color change agrees well with the cease of catalysis. The red-brown colored products are likely permanently reduced $[Ru(bpy)_3]^{2+}$. The same change was observed in the sample where only $[Ru(bpy)_3]^{2+}$ and TEOA are present in the solution. As these changes agree well with that via electrochemical reduction of $[Ru(bpy)_3]^{2+}$, it is likely that the color change of $[Ru(bpy)_3]^{2+}$ after catalysis is due to permanent reduction of $[Ru(bpy)_3]^{2+}$ by TEOA. While we are not sure of the exact degradation mechanism of $[Ru(bpy)_3]^{2+}$, it is possible that -bpy ligand substitution of reduced $[Ru(bpy)_3]^{2+}$ by TEOA or its degradation products may occur. This is because the reduction of Ru center typically leads to the destabilization of Ru-N bonds, which is then followed by ligand substitution by coordinating anionic or lewis basic species.[204]

On the other hand, the integrity of ZIF-67 during catalysis was confirmed by comparing its structure before and after catalysis. As shown in Figure 5.2c, the XRD patterns of ZIF-67 before and after catalysis recycled from the reaction mixture remain unchanged, suggesting that HER does not disrupt the crystalline nature of ZIF-67. Furthermore, *ex situ* XAS was used to examine the effect of photocatalysis on the atomic-scale local structure about the Co nodes. As shown in Figure 5.2d, negligible difference was observed in the X-ray absorption near edge structure (XANES) spectra of ZIF-67 at Co K-edge before and after catalysis, suggesting that photocatalysis did not change the coordination geometry and oxidation state of Co nodes. This assignment was further supported by quantitative analysis of extended X-ray absorption fine structure (EXAFS) spectra using FEFF fitting, where Co-N bond distance in before- and after-catalysis samples remains same (within uncertainty) (inset of Figure 5.2d).[177] These results suggest that both the local and bulk structure of ZIF-67 do not change after catalysis, indicating excellent stability of ZIF-67 during photocatalysis.

An additional concern to address is the possibility of leaching of Co into solution. By ICP-MS measurements, it was determined that 0.03 μmoles of Co are leached into solution during a 2-hour catalysis run in the recycling experiment. According to the $Co(MIM)_2$ equation, this represents approximately 0.3% leaching. In order to know the contribution of leached Co species to HER activity, we performed H_2 generation experiment of the supernatant solution under the same experimental conditions. The supernatant experiment gives negligible increase in HER activity compared to no ZIF-67 control condition, which suggests that leached Co species is not the active catalytic species, further supporting that ZIF-67 is the heterogeneous HER photocatalyst.

The HER activity observed for our ZIF-67 system is remarkable in comparison to other MOF systems for HER.[157,205-215] In the absence of cocatalysts, the majority of these systems showed limited HER activity (0-10^3 μmol H_2/g MOF). In the presence of cocatalysts, many of these systems demonstrated significantly boosted HER activity (10^2-10^5 μmol H_2/g MOF). To best of our knowledge, the HER activity in our system (40,500 μmol/g ZIF) is indeed higher than the highest reported Pt containing MOF catalysts (~ 30,000 μmol/g MOF).[207] The current ZIF-67 system, however, benefits from ease of synthesis and the prospect of scalability, as having intrinsically catalytic metal nodes means that there is no need for special cocatalyst treatments or addition steps. With respect to the catalytic Co metal nodes, using the $Co(IM)_2$ equation, a TON of 8 is calculated. While higher TONs (10^1-10^3) were reported in some cocatalyst-containing systems,[207,216-218] these numbers were typically calculated with respect to cocatalyst instead of MOF. Indeed, the TON of our system is much higher than systems where TONs with respect to MOF (TON < 1) were reported.[206,208,209]

It is also noted that HER activity of ZIF-67 in the current system is ~ 3 orders of magnitude higher than a similar system recently reported by our group, i.e. ZIF-67/RuN3 hybrid (48.5 μmol H_2/g ZIF-67).[132] In that ZIF-67/RuN3 system, we have shown that enhanced HER activity can be attributed to efficient ENT from the excited RuN3 to ZIF-67, forming excited state ZIF-67. This leads to structural distortion of ZIF-67 accompanied with charge transfer from the imidazole ligand to Co center, ultimately resulting in H_2 production. The significantly enhanced HER activity in the current system using $[Ru(bpy)_3]^{2+}$ as photosensitizer in comparison to the previous system with RuN3 as photosensitizer implies that the photocatalytic mechanism in the two systems is fundamentally different. In the following sections, we aim to fundamentally characterize the distinct catalytic events and intermediate steps that contribute to ZIF-67 catalyzed HER by various spectroscopic means.

Light Harvesting and Charge Separation Dynamics in [Ru(bpy)$_3$]$^{2+}$/ZIF-67

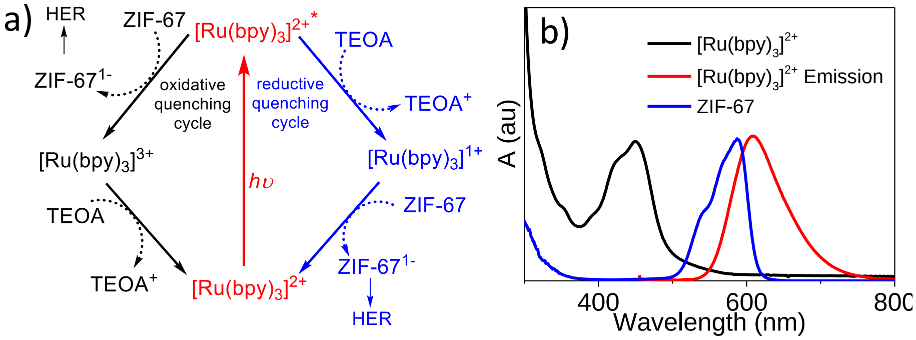

Figure 5.3. (a) Proposed catalytic mechanism of [Ru(bpy)$_3$]$^{2+}$/ZIF-67 for H_2 generation. (b) The UV-Visible absorption spectra of [Ru(bpy)$_3$]$^{2+}$ and ZIF-67, and the emission spectrum of [Ru(bpy)$_3$]$^{2+}$. The UV-visible absorption spectrum of ZIF-67 was collected in diffuse reflectance mode.

To fully understand the catalytic activity for HER observed, fundamental spectroscopic studies to elucidate the mechanism of interaction between the photosensitizer and ZIF-67 were performed. Due to the multicomponent nature of the photocatalytic system, there are multiple paths that could be followed to produce an activated ZIF-67 catalyst. The cartoon scheme in Figure 5.3a depicts these possibilities, namely A) the oxidative quenching cycle: ET from excited [Ru(bpy)$_3$]$^{2+}$ to ZIF-67, forming the reduced ZIF-67 (ZIF-67^{1-}) and oxidized [Ru(bpy)$_3$]$^{2+}$ ([Ru(bpy)$_3$]$^{3+}$); the latter accepts an electron from TEOA and returns to its ground state while the former proceeds to catalytic reaction. B) the reductive pathway: ET occurs from TEOA to excited [Ru(bpy)$_3$]$^{2+}$, forming reduced [Ru(bpy)$_3$]$^{2+}$ ([Ru(bpy)$_3$]$^{1+}$) and oxidized TEOA, which is followed by ET from ([Ru(bpy)$_3$]$^{1+}$ to ZIF-67, forming ZIF-67^{1-}. Another distinct possibility of ENT exists following our previous report of an ENT-based RuN3/ZIF-67 catalytic system.[132] Due to significant spectral overlap between the emission spectrum of $[Ru(bpy)_3]^{2+}$ and the absorption spectrum of ZIF-67 (Figure 5.3b) corresponding to the spin-allowed $^4A_2(F)–^4T_1(P)$ d-d transition of Co, ENT process from $[Ru(bpy)_3]^{2+}$ to ZIF-67 is also feasible and needs to be considered. These photophysical and photochemical processes typically occur in ultrafast scale and have distinct spectral features, and can thus be distinguished using time-resolved optical spectroscopy.

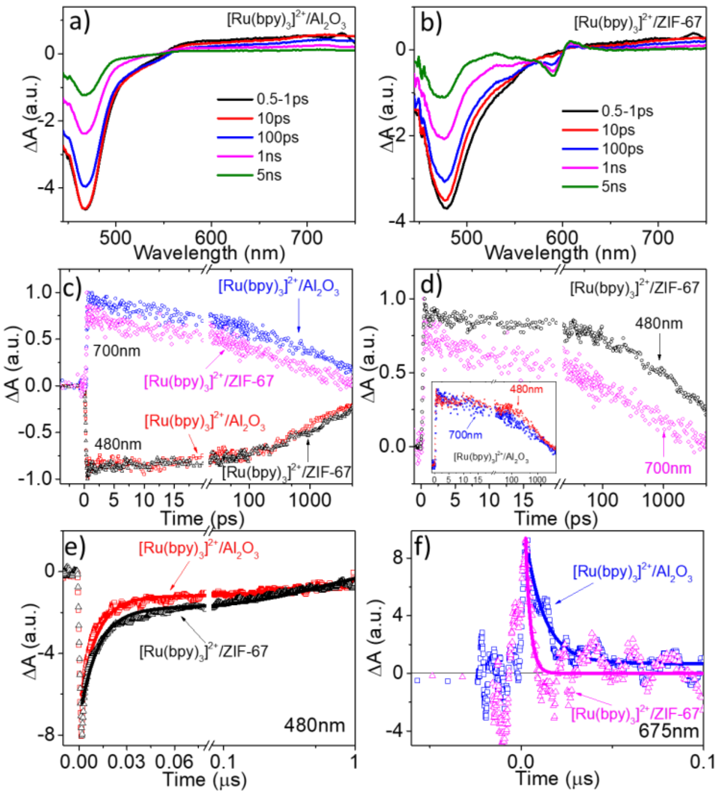

Figure 5.4. Femtosecond OTA results for selective excitation of $[Ru(bpy)_3]^{2+}$ on Al_2O_3 control (a) and ZIF-67 (b) at 410 nm. (c) The comparison of fs-OTA kinetics of $[Ru(bpy)_3]^{2+}$ ES and GSB between Al_2O_3 and ZIF-67. (d) The comparison of kinetics between ES and inverted GSB of $[Ru(bpy)_3]^{2+}$ on ZIF-67 and on Al_2O_3 (inset). Nanosecond OTA kinetics of the GSB recovery (e) and ES decay (f) on both substrates. Data is shown in open points and fits in solid lines.

Femtosecond optical absorption (fs-OTA) spectroscopy was first used to examine the ET/ENT dynamics between $[Ru(bpy)_3]^{2+}$ and ZIF-67. Figures 5.4a and 5.4b show the fs-OTA spectra of $[Ru(bpy)_3]^{2+}$ on Al_2O_3 and ZIF-67, respectively, after 410 nm excitation. 410 nm pump pulse was used to selectively excite $[Ru(bpy)_3]^{2+}$ only, as $[Ru(bpy)_3]^{2+}$ has prominent absorption at this wavelength while ZIF-67 has negligible absorption (Figure 5.3b). $[Ru(bpy)_3]^{2+}$ on Al_2O_3 substrate was used as control sample as neither ET nor ENT should occur from $[Ru(bpy)_3]^{2+}$ to Al_2O_3 due to extremely negative conduction band edge and large bandgap of Al_2O_3.[219] As shown in Figure 5.4a, the fs-OTA spectra of $[Ru(bpy)_3]^{2+}$ on Al_2O_3 show two instantaneously formed spectral features, including a negative feature centered at 480 nm and a broad positive feature from 565 nm to 750 nm. These features have been observed previously and can be attributed to ground-state bleach (GSB) of $[Ru(bpy)_3]^{2+}$ and ^{3}MLCT excited state (ES) absorption formed through ultrafast intersystem crossing (ISC) after photoexcitation, respectively.[219,220] The recovery of GSB and decay of ES occur simultaneously with a clear isosbestic point at ~560 nm, suggesting that these dynamics represent the same recombination process, i.e. relaxation of ES molecules to their GS.

While the similar GSB and ES absorption of $[Ru(bpy)_3]^{2+}$ on Al_2O_3 are observed in the spectra of $[Ru(bpy)_3]^{2+}$ on ZIF-67 (Figure 5.4b), two additional spectral features developed in the spectra of the latter, i.e. a negative feature at 580 nm and a positive absorption at 608 nm. These two features, resembling those observed previously in OTA spectra of ZIF-67 following direct excitation of ZIF-67,[177] can be attributed to the GSB and the formation of charge separated (CS) state in ZIF-67, respectively. Because no such features were observed in the fs-OTA spectra of ZIF-67 following 410 nm excitation, consistent with negligible absorption of ZIF-67 at 410 nm, the observed ZIF-67 features in the spectra of $[Ru(bpy)_3]^{2+}$/ZIF-67 must result from either ET or ENT from the excited $[Ru(bpy)_3]^{2+}$, which can be unambiguously distinguished by comparing the kinetic traces of $[Ru(bpy)_3]^{2+}$ GSB and ES on each sample. If ENT is responsible for the formation of ZIF-67 features, one would expect a simultaneously enhanced recovery of GSB and decay of ES of $[Ru(bpy)_3]^{2+}$, similar to our previous RuN3/ZIF-67 system.[132] However, as shown in Figure 5.4d, the decay of $[Ru(bpy)_3]^{2+}$ ES occurs much faster than $[Ru(bpy)_3]^{2+}$ GSB in $[Ru(bpy)_3]^{2+}$/ZIF-67 in contrast to the similar GSB and ES kinetics in $[Ru(bpy)_3]^{2+}/Al_2O_3$ (Figure 5.4d, inset). Furthermore, while the GSB recovery of $[Ru(bpy)_3]^{2+}$ in two samples remains similar, the ES decay in $[Ru(bpy)_3]^{2+}$/ZIF-67 sample is faster than that on Al_2O_3. These results, contradicting to the expected results for ENT, agree well with ET process from $[Ru(bpy)_3]^{2+}$ to ZIF-67. As illustrated in Equation 5.1, ET results in the formation of $[Ru(bpy)_3]^{3+}$ which facilitates ES decay and prohibits GSB recovery.

$$[Ru(bpy)_3]^{2+}* + ZIF-67 \xrightarrow{ET} [Ru(bpy)_3]^{3+} + ZIF-67^{-} \tag{5.1}$$

The ET process was further confirmed by nanosecond OTA (ns-OTA) which allowed us to probe the ET dynamics at later time scale. The ns-OTA spectra for $[Ru(bpy)_3]^{2+}$ on Al_2O_3 and ZIF-67 show similar spectral features to their fs-OTA spectra. However, from the kinetic traces (Figure 5.4e and 5.4f), it is apparent that while the ES of $[Ru(bpy)_3]^{2+}$ decays faster on ZIF-67 than on Al_2O_3, the GSB recovery of $[Ru(bpy)_3]^{2+}$ is slower in the former than the latter, further supporting our assignment of ET process from excited $[Ru(bpy)_3]^{2+}$ to ZIF-67.

The observation of ET does not exclude the possibility of ENT to ZIF-67, as the emission of $[Ru(bpy)_3]^{2+}$ has overlap with the absorption of ZIF-67 (Figure 5.3b). We are not able to examine ENT process by probing the emission of ZIF-67 because ZIF-67 is non-emissive in the visible range. However, according to the fact that the GSB recovery of $[Ru(bpy)_3]^{2+}$ on ZIF-67 is slower while its ES decay is faster than that on Al_2O_3, we are able to estimate the upper limit rate for ENT process. The kinetics of $[Ru(bpy)_3]^{2+}$ GSB recovery on ZIF-67 results from the combination of three possible paths, including 1) the intrinsic relaxation of ES molecules to GS, which follows the same GSB kinetics as on Al_2O_3; 2) the ENT process (if any), which is expected to enhance GSB recovery with respect to GSB kinetics on Al_2O_3; and 3) the recombination of the oxidized $[Ru(bpy)_3]^{2+}$ with the reduced ZIF-67 following ET process, which contributes to a slower GSB recovery on ZIF-67 than on Al_2O_3. Whether the GSB kinetics of $[Ru(bpy)_3]^{2+}$ on ZIF-67 is faster or slower than that on Al_2O_3 is determined by the competition between the 2nd and 3rd pathway. When the recombination through 3rd pathway is extremely slow and hardly contributes to the recovery of GSB, we can attribute the observed GSB recovery to ENT with an upper limit value of ENT rate. Through fitting the kinetic trace of $[Ru(bpy)_3]^{2+}$ GSB recovery on ZIF-67 (Figure 5.4e), the obtained ENT time, which represents shortest ENT time constant, is 420 ns. Because this is much longer than the ES decay time (2.7 ns), obtained from fitting the ES decay kinetics of $[Ru(bpy)_3]^{2+}$ on ZIF-67 (Figure 5.4f), we conclude that ENT process cannot compete with ET process. These results together suggest that photocatalysis proceeds through ET rather than ENT process from $[Ru(bpy)_3]^{2+}$ to ZIF-67. This also explains why HER activity in the current system is orders of magnitude higher than RuN3/ZIF-67 system which mainly undergoes ENT process.

Given the beneficial ET process and high HER efficiency in the current $[Ru(bpy)_3]^{2+}$/ZIF-67 system, one would expect that $[Ru(bpy)_3]^{2+}$ may link to ZIF-67 directly. However, we found that $[Ru(bpy)_3]^{2+}$ can neither directly attach to the surface of $[Ru(bpy)_3]^{2+}$, nor can it enter the pore of ZIF-67. While the origins of this problem remain uncertain to us, one possible explanation could be that $[Ru(bpy)_3]^{2+}$ may be associated with ZIF-67 through electrostatic attraction, as the surface of ZIF-67 is terminated by imidazole ligands which exhibit anionic character.[221]

To reveal whether photocatalysis undergoes reductive or oxidative quenching cycle (Figure 5.3a), we measured the ET dynamics between TEOA and $[Ru(bpy)_3]^{2+}$, which can be evaluated by measuring the steady state emission intensity of $[Ru(bpy)_3]^{2+}$ as a function of TEOA concentration. Stern-Volmer quenching experiments show that the emission intensity of $[Ru(bpy)_3]^{2+}$ is gradually quenched with increasing amount of TEOA added to the solution, suggesting that ET occurs from TEOA to $[Ru(bpy)_3]^{2+}$. The time constant for the emission quenching process was determined to be ~ 1.4 μs, which is much longer than ET time from excited $[Ru(bpy)_3]^{2+}$ to ZIF-67, suggesting that oxidative quenching cycle is the primary catalytic pathway for HER in the current $[Ru(bpy)_3]^{2+}$/ZIF-67 system.

In Situ XAS

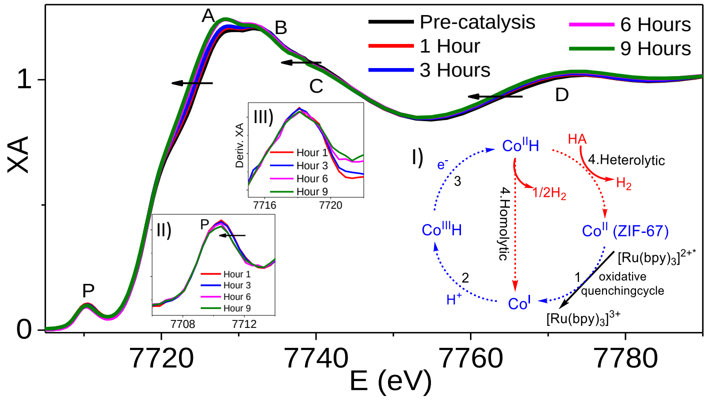

Figure 5.5. *In Situ* XANES spectra of ZIF-67 under standard HER condition. Inset I is the proposed catalytic mechanism for ZIF-67 catalyzed HER. Inset II is the zoom in picture of 1s-3d pre-edge feature. Inset III is the first derivative of XANES to illustrate the edge energy.

The time-resolved spectroscopic studies described above certainly provide important insight in the catalytic mechanism of the ZIF-67 catalysts, i.e. the light harvesting and charge separation (CS) dynamics which represents the key initial step to activate the catalytic cycle. However, many aspects of the mechanisms are yet unexplained. Besides the initial CS process (step 1 in inset I, Figure 5.5), the proposed catalytic pathway also involves the formation of hydride intermediates (step 2 and 3) which not only change the oxidation state (Co$^{I\text{-}III}$) but also the coordination environment at Co center. The multiple intermediates formed at Co center are further complicated by the possibilities of either homolytic or heterolytic H_2-producing mechanisms (step 4).[58] As a result, it is necessary to experimentally characterize the intermediate states with a technique that can follow both the oxidation state and coordination/structure of the Co metal center during catalysis simultaneously, namely *in situ* XAS, to gain direct information of the function of the photocatalyst in real time.

In order to obtain significant XAS signal from Co, the proportion of ZIF-67 in the optimized catalysis mixture was increased to 0.5 mg in a 3 mL solution for *in situ* measurement, i. e. 5 times more ZIF-67 than that used in optimized condition. In contrast to immediate generation of H_2 under the optimized conditions, an induction period was observed under the *in situ* conditions. Because induction period was typically associated with the multiple equilibriums that require conversion of Co center to its reduced intermediates or hydrides before H_2 generation,[25] the presence of induction period in the *in situ* condition but not in the optimized condition is likely due to that longer time is required to convert larger amount of ZIF-67 to their intermediate species to achieve multiple equilibriums.

Figure 5.5 shows the *in situ* XANES spectra collected during the course of HER catalysis. The initial XANES spectrum shows a prominent pre-edge feature (labeled P) that corresponds to the dipole-forbidden 1s-3d transition due to p-d mixing in the non-centrosymmetric tetrahedral ligand field geometry. The two distinct rising edges at 7718 eV and 7724 eV are typical of Co^{II} complexes with lower-order (<6) coordination.[222] In addition to these edge features, feature A and B, which correspond to the 1s-4p white line transition and are sensitive to coordination number at Co center, were also observed in the XANES spectra. During photocatalysis, multiple gradual changes to the XANES spectra are observed during the first 1-6 hours of illumination, which is consistent with the presence of induction period for H_2 generation. As seen from Figure 5.5, the overall spectrum (A-D bands) shows a gradual red-shift, suggesting that Co-N bond distance increase during photocatalysis. This assignment was further supported by the pre-edge feature P which shifts to lower energy accompanied by the reduction of their intensity

(Inset II). As pre-edge feature P is a measure of the ligand field strength at Co center,[175] the shift observed in P can be assigned to a decreased ligand field strength due to the elongation of Co-N bond. Furthermore, notable changes were observed in feature A and B, where the intensity of feature A increases while that of B decreases. As increased intensity for A and decreased intensity for B are responsible for a more highly-coordinated Co^{II} center,[222] we believe that the coordination number of Co increases during catalysis. Despite these changes, negligible shift was observed in the edge region (Inset III), suggesting that the intermediate species remains +2 oxidation state.

While the above *in situ* XAS results unravelled that intermediate species possess larger coordination number and longer Co-N distance, and remain an oxidation state of +2, there are possibilities that such features could result from the average of multiple Co intermediates involved in the complex catalytic cycle (Inset I in Figure 5.5) or a single intermediate that accumulated during catalysis. If the former is responsible for the observed spectral features, the concentration of Co^{I} and $Co^{III}H$ species (Inset I in Figure 5.5) is expected to remain similar during the catalytic cycle. In contrast, if the observed spectral features is mainly due to the accumulation of a single intermediate, this species is most likely Co^{II}-H because this is the only Co^{II} species in the proposed mechanism. As a result, the consumption of Co^{II}-H (step 4) is possibly the rate limiting step in the photocatalytic cycle. It is also difficult to determine whether the homo- or heterolytic mechanism dominates in the catalytic cycle for ZIF-67 catalyzed HER. However, a requisite for the heterolytic mechanism is a highly acidic environment,[58] which is not present in the catalytic system, as TEOA is the proton source and has a 7.77 pKa in water.[223] Furthermore, the Co sites are confined to a distance of approximately 6.00 Å in the crystal structure of ZIF-67.[164] Such short distance between Co sites make it possible that two $Co^{II}H$ species may interact within a single crystallite. These two factors together suggest that homolytic mechanism might be preferred in the current system, however, the heterolytic mechanism cannot be excluded.

Conclusion

In summary, we report a recyclable and highly efficient ZIF-67 catalyst for HER. In the presence of molecular photosensitizer, we achieved an activity of 40,500 μmol H_2/g ZIF, which is remarkable compared to other MOF H_2 evolution catalysts. More importantly, the mechanistic function for HER was investigated for the first time using time-resolved optical and real-time *in situ* XAS spectroscopic techniques. Using time-resolved OTA spectroscopy, we show that ET rather than ENT is the key factor that determines the efficiency of ZIF-67 for HER. Using *in situ* XAS, we uncovered the spectral features that correspond to the intermediate species for catalytic cycle, either resulting from the average of multiple intermediates or a single $Co^{II}H$ species.

As indicated by the charge separation pathway in this work, future work using photosensitizers that can facilitate ET but inhibit ENT process would certainly benefit HER efficiency. Inspired from the catalytic mechanism, future work should focus on the design of ZIF based catalytic systems with inherently large pore and cavity such that the key components for catalysis can be directly encapsulated, thereby making all catalytic metal sites accessible.

Appendix A

IRON-ZINC COMPOSITE ZEOLITIC IMIDAZOLATE FRAMEWORKS

Structural and Light-Harvesting Properties of Fe-Zn ZIFs

Introduction

As evidenced by the intrinsic photocatalytic activity of Co-based ZIF-67 toward HER and the observed intermediate species, the metal ion node can play a major role in the photocatalytic activity of ZIF. Although ZIFs are traditionally composed of Zn^{II} or Co^{II} ions, it was demonstrated and discussed in chapter 4 that other transition metals can occupy the Co^{II} ion location in the ZIF structure. This provides an important opportunity to tune the light harvesting properties and catalytic activity of ZIFs by incorporating metal ions of different identity into the framework.

Because Zn^{II} ions in ZIF are closed shell with d10 electronic structure, they demonstrate no photochemical response in the visible light range, thereby providing an opportunity to study the properties of other transition metals doped into the framework. Additionally, Zn^{II} based ZIFs have superior stability to Co^{II} based ZIFs, implying that a composite ZIF based on Zn^{II} and another open shell transition metal has the potential to be developed into a robust photocatalyst material. In this work, Fe^{III} is doped into the ZIF framework at varying amounts to study the photodynamic and structural properties of the new material.

Results and Discussion

First, a synthesis route to reliably incorporate Fe^{III} into the ZIF-8 structure was developed. A total of 400mg of metal nitrate precursor, composed of either $Zn(NO_3)_2 \cdot 6H_2O$ or $Fe(NO_3)_3 \cdot 9H_2O$ was dissolved in 10 mL of DI H_2O. While the solution was magnetically stirred, 2M NaOH was added until the PH became basic (PH 11). A second solution composed of 1 g of 2-methylimidazole was prepared in 15mL of DI H_2O. After stirring the PH 11 metal solution for 2 minutes, the 2-methylimidazole solution was dropped in at a rate of 2 drops/second into the vigorously stirred metal solution. Immediately, precipitation of the ZIF occurs. After the 2-methylimidazole solution was fully added, the solution was stirred for 10 minutes before subsequent washing via centrifugation using water, then methanol. The final product is dried in air after 2 methanol rinses.

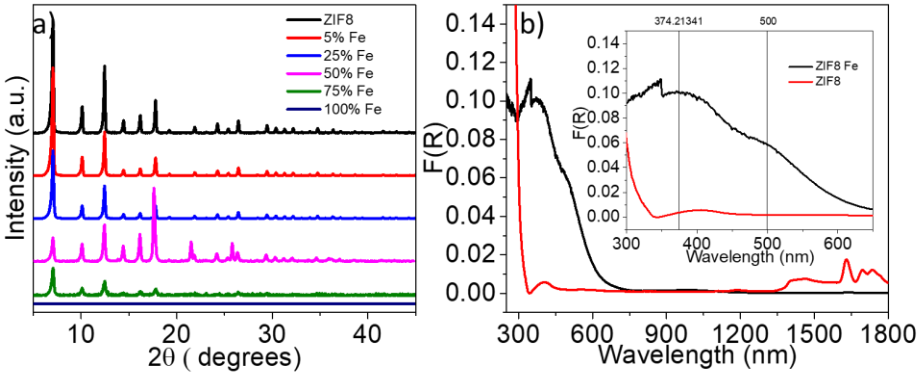

Figure A1. pXRD patterns (a) for various doping amounts of Fe. UV-Visible reflectance spectra (b) for ZIF-8 and 50% Fe-doped ZIF-8. Inset of (b) shows the magnified visible region and approximate wavelengths of observed peaks.

Unlike the pure white-colored ZIF-8 powder, the obtained product has a burnt red color that increases in intensity with the amount of Fe included in the synthesis. It is noted that the supernatant from the first rinse is colorless, likely indicating that all Fe is incorporated into the structure. The pXRD patterns (Figure A1a) show that SOD topology is maintained at all of the doping amounts that contain Zn (i.e. the 100% Fe product formed is amorphous). Interestingly, up to 50% Fe, the powders are not very dense by feel, however higher Fe amount leads to a more dense, brittle material with lower crystallinity. Additionally, 75% and 100% Fe samples cannot be easily suspended in water or organic solvent unlike the other Fe-ZIFs. Therefore, 50% Fe in the precursor represents a balance between crystallinity and incorporating a maximum number of Fe-sites while maintaining typical ZIF behavior.

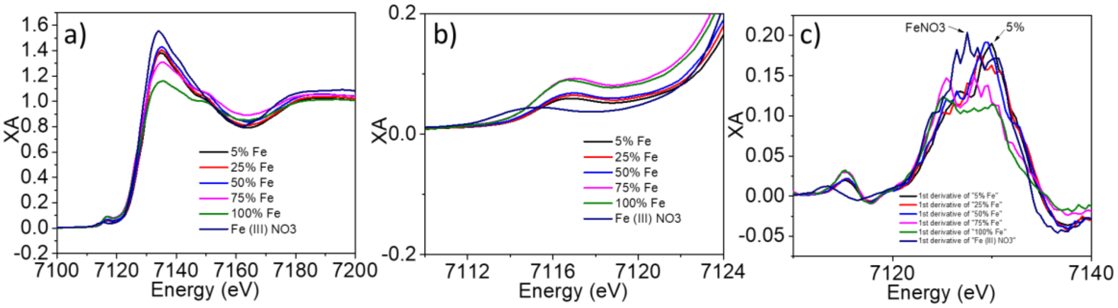

Figure A2. Fe K-edge XANES spectra for different compositions of Fe (a). Enlarged pre-edge region (b) and first derivative spectra (c).

The UV-Visible spectra in Figure A1b reflect the red coloration of Fe-ZIF. A broad absorbance band is observed in the 350-650nm range that is not present in ZIF-8 that must be due to the incorporation of Fe. If Fe is incorporated as a node in the ZIF structure, then it is expected to be in the same tetrahedral geometry as the Zn nodes in the structure.

To investigate the local structure of Fe in the composite ZIF, Fe K-edge XAS was performed. Figure A2a shows the XANES spectra for different compositions of Fe along with the $Fe(NO_3)_3 \cdot 9H_2O$ precursor spectrum. There is a weak trend in the intensity of the peak corresponding to the 1s-4p transition with increasing Fe content, however no significant differences are observed compared to the precursor. However, obvious changes are observed in the pre-edge region (Figure A2b). All of the Fe-doped ZIF-8 samples show a shifted 1s-3d transition, indicating a different ligand field compared to the precursor, providing evidence that the coordination environment of Fe is different in the ZIF samples. Additionally, the intensity of the pre-edge feature is more intense that that of the precursor, supporting tetrahedral coordination of the Fe metal ion.

The first derivative of the XANES region (Figure A2c). shows that the Fe-ZIFs all have a different shape in the spectrum compared to the precursor, suggesting a different electronic environment. Interestingly, there is a trend observed from low Fe % to high Fe %, where the first derivative peak at 7130 eV redshifts with increasing Fe, suggesting that the average oxidation state of Fe decreases with increasing Fe content. Because the peak at 7130eV is at higher energy than the Fe^{III} precursor peak, it is assigned as a signature of Fe^{III}. Therefore, the weakening of this feature relative to the lower energy shoulder indicates that lower oxidation states such as Fe^{II} might be present at high Fe %. While the nature of this trend is not clear, as it might be due to synthetic conditions, it implies that Fe-ZIF can adopt multiple stable oxidation states, an important prerequisite to effective photoredox catalysis.

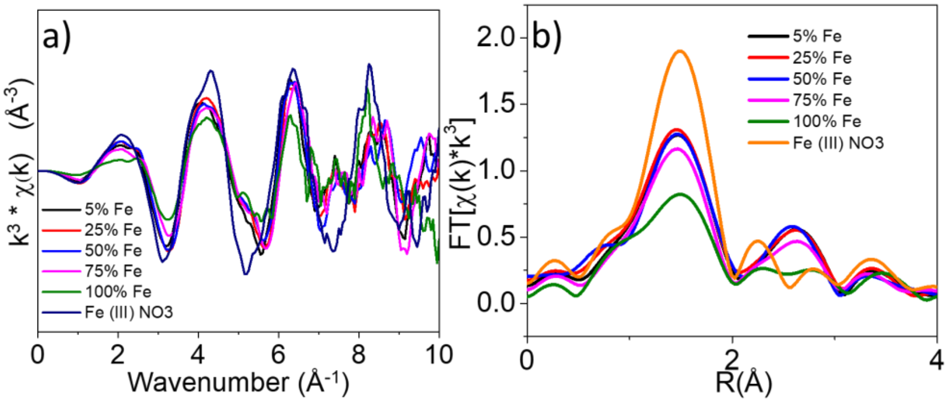

Figure A3. K-space EXAFS spectra (a) and R-space spectra (b) for Fe-K edge data.

The Fourier-transformed K-space spectra (Figure A3a) show that the oscillations are very similar for the Fe-ZIF samples, but have different frequency contributions that are observable, specifically, at approximately 4.2, 5.1, and 7.3 Å^{-1} compared to the precursor, indicating differing local structure. The reverse Fourier-transformed R-space spectra in Figure A3b demonstrate that the first-shell coordination difference in all of the samples, including the precursor, are all similar. However, significant difference is observed in the second shell, specifically at 2.5 Å. For all of the samples that showed crystallinity in pXRD, there is a single, prominent peak in the second shell corresponding to scattering of the photoelectron by atoms other than N. While it was confirmed that both 75% Fe and 100% Fe samples were coordinated to the ligand, it is possible that heterogeneity in the photoelectron path length could lead to the reduction of this feature for 75% Fe and disappearance of the feature for 100% Fe. This heterogeneity is likely related to the poor/amorphous crystallinity observed in 75%/100% Fe-ZIF-8. Therefore, these results support the conclusion that Fe can be incorporated into the ZIF structure, with negligible change in the local structure up to 50% Fe.

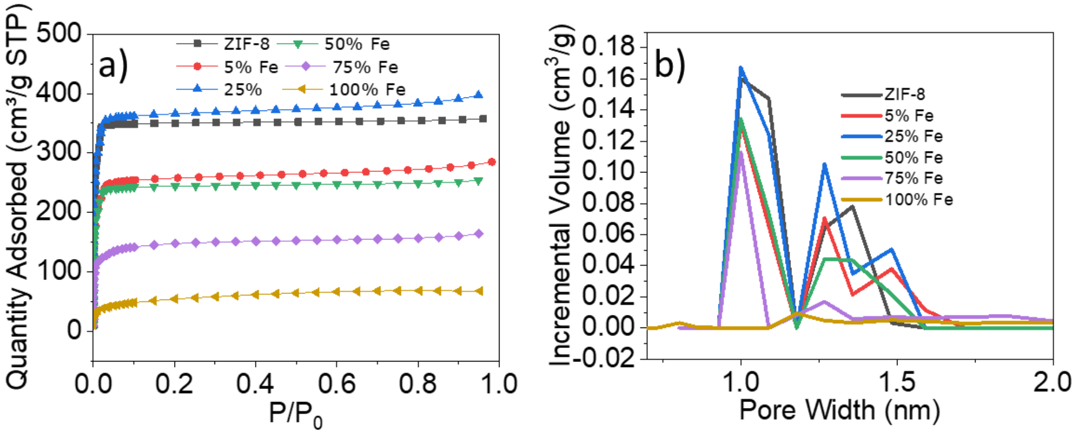

Figure A4. N_2 adsorption isotherms (a) and pore distributions (b) for ZIF-8 and the Fe-composite analogues.

The N_2 adsorption abilities of the Fe-ZIF-8 samples were analyzed to investigate the porosity of the materials in Figure A4. The N_2 adsorption isotherms in Figure A1.5a show that, despite some variability, there is significant decrease in the quantity of N_2 adsorbed per unit mass of the ZIF by 75% Fe content, and a further decrease at 100%. These results are in agreement with pXRD and XAS studies that suggested poor formation of the ZIF structure at high Fe%, confirming that the porous structure of ZIF-8 is compromised at >50% Fe content. The pore size distribution is compared in Figure A1.5b, showing that the pore sizes remain similar up to 75% Fe, however a decrease in the pore volume is observed at 75% Fe, especially for the larger pore sizes. For 100% Fe, very limited porosity remains, in agreement with all of the above studies.

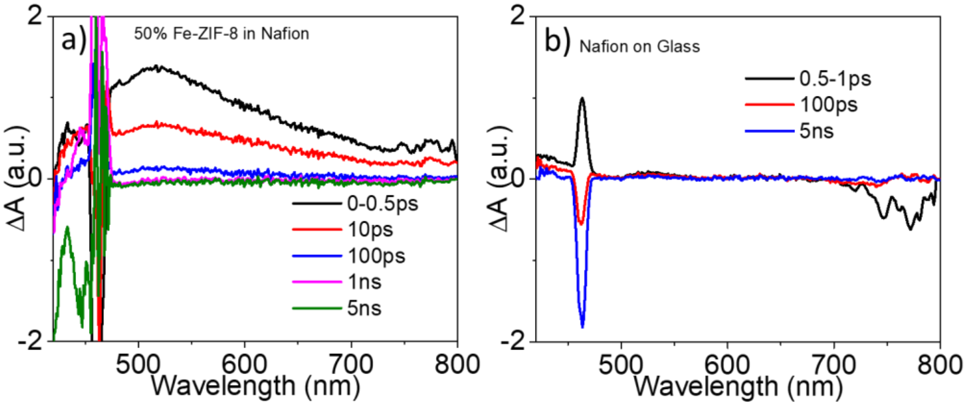

Figure A5. Femtosecond OTA spectra for 50% Fe-ZIF-8 in Nafion (a) and Nafion on glass as a control sample (b). The same femtosecond OTA setup described in chapter 2 was used, and 450nm excitation with 0.7 µJ/pulse pump fluence was used.

The optical properties of 50% Fe ZIF-8 were investigated by femtosecond OTA (Figure A5a). To prepare the sample, 3mg of Fe-ZIF-8 were suspended in nafion solution (1mL) and sonicated for 20 minutes. The nafion solution was then dropped onto glass substrate and allowed to dry at room temperature. After 450nm excitation, corresponding to excitation of the Fe d-d transitions, a broad, positive, transient feature is observed from the saturation at 450nm due to the scattered pump beam to the end of the detection window, approximately 800nm. The feature decays fully within 5ns, indicating that deactivation of the Fe d-d excited state is significantly shorter than that of Co-based ZIFs. The signal was confirmed to be due to the presence of Fe-ZIF-8 using the control sample of nafion on glass (Figure A5b).

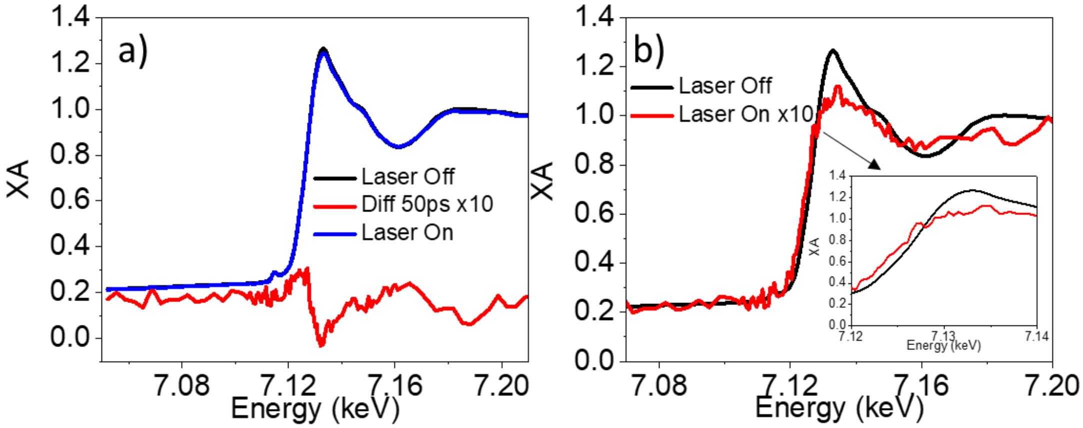

Figure A6. XTA results for 50% Fe ZIF-8. (a) The Fe K-edge XANES region. Laser off spectrum represents the ground state spectrum of Fe-ZIF-8 suspended in MeOH. The laser on spectrum is collected 50 ps after 400nm laser excitation of the sample. The difference signal in red was multiplied 10x to compare to the spectral features. In (b), the laser-on spectrum was regenerated with the 10x spectrum.

Even though the excited state lifetime observed in OTA experiments was significantly shorter than the Co-based analogue, the nature of the excited state is still of great interest for photocatalytic applications. To investigate the changes in oxidation state at Fe metal center after photoexcitation, X-ray transient absorption (XTA) was performed at the Fe K-edge. Figure A6a shows the XANES spectra of the laser on and laser off conditions and the difference between laser on – laser off. The difference signature observed indicates that, at the time delay of 50ps, reduction of Fe center is observed due to shift in the XANES edge to lower energy. To demonstrate this shift and the other changes that accompany it, the laser-on x10 spectrum was generated using the difference x10 spectrum and the laser off spectrum (Figure A6b).

This result shows that the Fe d-d transitions experience oxidation state changes after excitation of their d-d transitions. Because a mixture of different oxidation states was implied by the first derivative XANES results in Figure A2c, it is difficult to ascertain whether the electron the localizes on Fe after photoexcitation came from the ligand or from another metal atom with different oxidation state. Either of these results would be interesting, however, because they both fit the narrative uncovered in the previous ZIF studies presented in chapter 4. Evidently, the photodynamics of open-shell metal ions in the ZIF structure demands thorough investigation and strongly imply photocatalytic applications.

Conclusions

In conclusion, composite Fe-ZIF-8 was prepared at varying Fe %. The Fe was found to incorporate at Zn sites in the structure and had minimal effect on the local structure and porosity of the material up to 50% Fe. The 50% Fe-ZIF-8 sample was investigated to reveal its optical properties by OTA, indicating that the Fe d-d excited state is deactivated < 1ns. However, XTA experiments demonstrated that there is a shift in electron density after photoexcitation of Fe d-d transitions that results in a reduced Fe center. While the nature of this change is difficult to assign, it implies that, in combination with the XAS results that show the presence of multiple oxidation states, Fe-ZIF-8 is a stable, light-absorbing material capable of cycling between multiple oxidation states. Because this is an important prerequisite to photocatalysis, Fe-ZIF-8 should be investigated as a promising photocatalyst material. Because of the nature of ZIF structure, the ZIF framework offers Fe sites as accessible single-site metals in a porous framework, and these advantages may lend themselves well to photocatalytic applications.

REFERENCES

(1) O'Regan, B.; Gratzel, M. *Nature* **1991**, *353*, 737.

(2) Fujishima, A.; Honda, K. *Nature* **1972**, *238*, 37.

(3) Kojima, A.; Teshima, K.; Shirai, Y.; Miyasaka, T. *Journal of the American Chemical Society* **2009**, *131*, 6050.

(4) Saga, T. *NPG Asia Mater* **2010**, *2*, 96.

(5) Hou, Y.; Vidu, R.; Stroeve, P. *Industrial & Engineering Chemistry Research* **2011**, *50*, 8954.

(6) Gratzel, M. *Nature* **2001**, *414*, 338.

(7) Ryeol, W. D.; Hazar, A. D. *ChemPhotoChem* **2018**, *2*, 148.

(8) Gust, D.; Moore, T. A.; Moore, A. L. *Accounts of Chemical Research* **2009**, *42*, 1890.

(9) Barber, J.; Tran, P. D. *Journal of The Royal Society Interface* **2013**, *10*.

(10) Yutaka, A. *ChemCatChem* **2011**, *3*, 458.

(11) McConnell, I.; Li, G.; Brudvig, G. W. *Chemistry & Biology* **2010**, *17*, 434.

(12) Bard, A. J.; Fox, M. A. *Accounts of Chemical Research* **1995**, *28*, 141.

(13) Scanlon, D. O.; Dunnill, C. W.; Buckeridge, J.; Shevlin, S. A.; Logsdail, A. J.; Woodley, S. M.; Catlow, C. R. A.; Powell, M. J.; Palgrave, R. G.; Parkin, I. P.; Watson, G. W.; Keal, T. W.; Sherwood, P.; Walsh, A.; Sokol, A. A. *Nat Mater* **2013**, *12*, 798.

(14) Tan, M. X.; Laibinis, P. E.; Nguyen, S. T.; Kesselman, J. M.; Stanton, C. E.; Lewis, N. S. In *Progress in Inorganic Chemistry* 1994; Vol. 41, p 21.

(15) Swierk, J. R.; Mallouk, T. E. *Chemical Society Reviews* **2013**, *42*, 2357.

(16) Christensen, P. A.; Harriman, A.; Porter, G.; Neta, P. *Journal of the Chemical Society, Faraday Transactions 2: Molecular and Chemical Physics* **1984**, *80*, 1451.

(17) Santos, T. D.; Morandeira, A.; Koops, S.; Mozer, A. J.; Tsekouras, G.; Dong, Y.; Wagner, P.; Wallace, G.; Earles, J. C.; Gordon, K. C.; Officer, D.; Durrant, J. R. *The Journal of Physical Chemistry C* **2010**, *114*, 3276.

(18) Birel, Ö.; Nadeem, S.; Duman, H. *Journal of Fluorescence* **2017**, *27*, 1075.

(19) Kuppuswamy, K.; Michael, G. *Angewandte Chemie International Edition in English* **1979**, *18*, 701.

(20) Rillema, D. P.; Dressick, W. J.; Meyer, T. J. *Journal of the Chemical Society, Chemical Communications* **1980**, 247.

(21) Demas, J. N.; Taylor, D. G. *Inorganic Chemistry* **1979**, *18*, 3177.

(22) Duan, L.; Bozoglian, F.; Mandal, S.; Stewart, B.; Privalov, T.; Llobet, A.; Sun, L. *Nature Chemistry* **2012**, *4*, 418.

(23) Rabten, W.; Kärkäs, M. D.; Åkermark, T.; Chen, H.; Liao, R.-Z.; Tinnis, F.; Sun, J.; Siegbahn, P. E. M.; Andersson, P. G.; Åkermark, B. *Inorganic Chemistry* **2015**, *54*, 4611.

(24) Duan, L.; Fischer, A.; Xu, Y.; Sun, L. *Journal of the American Chemical Society* **2009**, *131*, 10397.

(25) Liu, F.; Concepcion, J. J.; Jurss, J. W.; Cardolaccia, T.; Templeton, J. L.; Meyer, T. J. *Inorganic Chemistry* **2008**, *47*, 1727.

(26) Daniel, Q.; Duan, L.; Timmer, B. J. J.; Chen, H.; Luo, X.; Ambre, R.; Wang, Y.; Zhang, B.; Zhang, P.; Wang, L.; Li, F.; Sun, J.; Ahlquist, M.; Sun, L. *ACS Catalysis* **2018**, *8*, 4375.

(27) Thomsen, J. M.; Huang, D. L.; Crabtree, R. H.; Brudvig, G. W. *Dalton Transactions* **2015**, *44*, 12452.

(28) Cristiano, Z.; Gianfranco, B.; Olga, B.; Alberto, B.; Arianna, S.; Alceo, M. *Chemistry – A European Journal* **2014**, *20*, 3446.

(29) Kasapbasi, E. E.; Whangbo, M.-H. *Inorganic Chemistry* **2012**, *51*, 10850.

(30) Hong, D.; Mandal, S.; Yamada, Y.; Lee, Y.-M.; Nam, W.; Llobet, A.; Fukuzumi, S. *Inorganic Chemistry* **2013**, *52*, 9522.

(31) Biaobiao, Z.; Fei, L.; Fengshou, Y.; Honghua, C.; Xu, Z.; Hua, L.; Yong, W.; Licheng, S. *Chemistry – An Asian Journal* **2014**, *9*, 1515.

(32) Toshiyuki, A.; Keiji, N.; Satoko, K.; Masao, K.; Akio, T.; Takayoshi, N. *Angewandte Chemie International Edition* **2006**, *45*, 2778.

(33) Rigsby, M. L.; Mandal, S.; Nam, W.; Spencer, L. C.; Llobet, A.; Stahl, S. S. *Chemical Science* **2012**, *3*, 3058.

(34) John, K.; Michael, G. *Angewandte Chemie International Edition in English* **1978**, *17*, 860.

(35) Nahor, G. S.; Hapiot, P.; Neta, P.; Harriman, A. *The Journal of Physical Chemistry* **1991**, *95*, 616.

(36) Hara, M.; Waraksa, C. C.; Lean, J. T.; Lewis, B. A.; Mallouk, T. E. *The Journal of Physical Chemistry A* **2000**, *104*, 5275.

(37) Jiao, F.; Frei, H. *Energy & Environmental Science* **2010**, *3*, 1018.

(38) Esswein, A. J.; McMurdo, M. J.; Ross, P. N.; Bell, A. T.; Tilley, T. D. *The Journal of Physical Chemistry C* **2009**, *113*, 15068.

(39) Mondschein, J. S.; Callejas, J. F.; Read, C. G.; Chen, J. Y. C.; Holder, C. F.; Badding, C. K.; Schaak, R. E. *Chemistry of Materials* **2017**, *29*, 950.

(40) Kanan, M. W.; Nocera, D. G. *Science* **2008**, *321*, 1072.

(41) Khnayzer, R. S.; Mara, M. W.; Huang, J.; Shelby, M. L.; Chen, L. X.; Castellano, F. N. *ACS Catalysis* **2012**, *2*, 2150.

(42) Morita, M.; Iwakura, C.; Tamura, H. *Electrochimica Acta* **1977**, *22*, 325.

(43) Huynh, M.; Bediako, D. K.; Nocera, D. G. *Journal of the American Chemical Society* **2014**, *136*, 6002.

(44) Khaselev, O.; Turner, J. A. *Science* **1998**, *280*, 425.

(45) Bolton, J. R.; Strickler, S. J.; Connolly, J. S. *Nature* **1985**, *316*, 495.

(46) Walter, M. G.; Warren, E. L.; McKone, J. R.; Boettcher, S. W.; Mi, Q.; Santori, E. A.; Lewis, N. S. *Chemical Reviews* **2010**, *110*, 6446.

(47) Chen, X.; Shen, S.; Guo, L.; Mao, S. S. *Chemical Reviews* **2010**, *110*, 6503.

(48) Hong, Y.-R.; Liu, Z.; Al-Bukhari, S. F. B. S. A.; Lee, C. J. J.; Yung, D. L.; Chi, D.; Hor, T. S. A. *Chemical Communications* **2011**, *47*, 10653.

(49) Chatman, S.; Zarzycki, P.; Rosso, K. M. *ACS Applied Materials & Interfaces* **2015**, *7*, 1550.

(50) Cummings, C. Y.; Marken, F.; Peter, L. M.; Upul Wijayantha, K. G.; Tahir, A. A. *Journal of the American Chemical Society* **2012**, *134*, 1228.

(51) Spray, R. L.; McDonald, K. J.; Choi, K.-S. *The Journal of Physical Chemistry C* **2011**, *115*, 3497.

(52) Maeda, K. *ACS Catalysis* **2013**, *3*, 1486.

(53) Voiry, D.; Salehi, M.; Silva, R.; Fujita, T.; Chen, M.; Asefa, T.; Shenoy, V. B.; Eda, G.; Chhowalla, M. *Nano Letters* **2013**, *13*, 6222.

(54) Sun, Y.; Liu, C.; Grauer, D. C.; Yano, J.; Long, J. R.; Yang, P.; Chang, C. J. *Journal of the American Chemical Society* **2013**, *135*, 17699.

(55) Miao, R.; Dutta, B.; Sahoo, S.; He, J.; Zhong, W.; Cetegen, S. A.; Jiang, T.; Alpay, S. P.; Suib, S. L. *Journal of the American Chemical Society* **2017**, *139*, 13604.

(56) McKone, J. R.; Sadtler, B. F.; Werlang, C. A.; Lewis, N. S.; Gray, H. B. *ACS Catalysis* **2013**, *3*, 166.

(57) Jović, B. M.; Lačnjevac, U. Č.; Krstajić, N. V.; Jović, V. D. *International Journal of Hydrogen Energy* **2014**, *39*, 8947.

(58) Dempsey, J. L.; Brunschwig, B. S.; Winkler, J. R.; Gray, H. B. *Accounts of Chemical Research* **2009**, *42*, 1995.

(59) Gross, M. A.; Reynal, A.; Durrant, J. R.; Reisner, E. *Journal of the American Chemical Society* **2014**, *136*, 356.

(60) Rana, A.; Mondal, B.; Sen, P.; Dey, S.; Dey, A. *Inorganic Chemistry* **2017**, *56*, 1783.

(61) Mizoguchi, Y.; Fujihara, S. *Electrochemical and Solid-State Letters* **2008**, *11*, K78.

(62) Nattestad, A.; Mozer, A. J.; Fischer, M. K. R.; Cheng, Y. B.; Mishra, A.; Bäuerle, P.; Bach, U. *Nature Materials* **2009**, *9*, 31.

(63) Gardner, J. M.; Beyler, M.; Karnahl, M.; Tschierlei, S.; Ott, S.; Hammarström, L. *Journal of the American Chemical Society* **2012**, *134*, 19322.

(64) Lv, H.; Wang, C.; Li, G.; Burke, R.; Krauss, T. D.; Gao, Y.; Eisenberg, R. *Proceedings of the National Academy of Sciences* **2017**, *114*, 11297.

(65) Makarov, N. S.; Lim, J.; Lin, Q.; Lewellen, J. W.; Moody, N. A.; Robel, I.; Pietryga, J. M. *Nano Letters* **2017**, *17*, 2319.

(66) Kim, J. H.; Jo, Y.; Kim, J. H.; Jang, J. W.; Kang, H. J.; Lee, Y. H.; Kim, D. S.; Jun, Y.; Lee, J. S. *ACS Nano* **2015**, *9*, 11820.

(67) Reece, S. Y.; Hamel, J. A.; Sung, K.; Jarvi, T. D.; Esswein, A. J.; Pijpers, J. J. H.; Nocera, D. G. *Science* **2011**, *334*, 645.

(68) Nocera, D. G. *Accounts of Chemical Research* **2012**, *45*, 767.

(69) Liu, C.; Colón, B. C.; Ziesack, M.; Silver, P. A.; Nocera, D. G. *Science* **2016**, *352*, 1210.

(70) Tan, H. L.; Amal, R.; Ng, Y. H. *Journal of Materials Chemistry A* **2017**, *5*, 16498.

(71) Martinez Suarez, C.; Hernández, S.; Russo, N. *Applied Catalysis A: General* **2015**, *504*, 158.

(72) Lamm, B.; Trześniewski, B. J.; Döscher, H.; Smith, W. A.; Stefik, M. *ACS Energy Letters* **2018**, *3*, 112.

(73) Park, Y.; McDonald, K. J.; Choi, K.-S. *Chemical Society Reviews* **2013**, *42*, 2321.

(74) Cooper, J. K.; Gul, S.; Toma, F. M.; Chen, L.; Glans, P.-A.; Guo, J.; Ager, J. W.; Yano, J.; Sharp, I. D. *Chemistry of Materials* **2014**, *26*, 5365.

(75) Sleight, A. W.; Chen, H. Y.; Ferretti, A.; Cox, D. E. *Materials Reserach Bulletin* **1979**, *14*, 1571.

(76) Bierlein, J. D.; Sleight, A. W. *Solid State Communications* **1975**, *16*, 69.

(77) Tokunaga, S.; Kato, H.; Kudo, A. *Chemistry of Materials* **2001**, *13*, 4624.

(78) Usai, S.; Obregón, S.; Becerro, A. I.; Colón, G. *The Journal of Physical Chemistry C* **2013**, *117*, 24479.

(79) Walsh, A.; Yan, Y.; Huda, M. N.; Al-Jassim, M. M.; Wei, S.-H. *Chemistry of Materials* **2009**, *21*, 547.

(80) Zhao, Z.; Li, Z.; Zou, Z. *Physical Chemistry Chemical Physics* **2011**, *13*, 4746.

(81) David, W. I. F.; Wood, I. G. *Journal of Physics C: Solid State Physics* **1983**, *16*, 5127.

(82) Stoltzfus, M. W.; Woodward, P. M.; Seshadri, R.; Klepeis, J.-H.; Bursten, B. *Inorganic Chemistry* **2007**, *46*, 3839.

(83) Fan, H.; Jiang, T.; Li, H.; Wang, D.; Wang, L.; Zhai, J.; He, D.; Wang, P.; Xie, T. *The Journal of Physical Chemistry C* **2012**, *116*, 2425.

(84) Atkins, P. O., Tina; Rourke, Jonathan; Weller, Mark; Armstrong, Fraser; Hagerman, Michael *Inorganic Chemistry*; Oxford University Press: Great Britain, 2010.

(85) Wang, J.; Sun, H.; Huang, J.; Li, Q.; Yang, J. *The Journal of Physical Chemistry C* **2014**, *118*, 7451.

(86) Kong, L.; Wang, C.; Zheng, H.; Zhang, X.; Liu, Y. *The Journal of Physical Chemistry C* **2015**, *119*, 16623.

(87) Niu, M.; Cheng, D.; Cao, D. *The Journal of Physical Chemistry C* **2013**, *117*, 15911.

(88) Zhou, M.; Bao, J.; Xu, Y.; Zhang, J.; Xie, J.; Guan, M.; Wang, C.; Wen, L.; Lei, Y.; Xie, Y. *ACS Nano* **2014**, *8*, 7088.

(89) Ye, H.; Lee, J.; Jang, J. S.; Bard, A. J. *The Journal of Physical Chemistry C* **2010**, *114*, 13322.

(90) Park, H. S.; Kweon, K. E.; Ye, H.; Paek, E.; Hwang, G. S.; Bard, A. J. *The Journal of Physical Chemistry C* **2011**, *115*, 17870.

(91) Jiang, Z.; Liu, Y.; Jing, T.; Huang, B.; Zhang, X.; Qin, X.; Dai, Y.; Whangbo, M.-H. *The Journal of Physical Chemistry C* **2016**, *120*, 2058.

(92) Pattengale, B.; Ludwig, J.; Huang, J. *The Journal of Physical Chemistry C* **2016**, *120*, 1421.

(93) Pattengale, B.; Huang, J. *Physical Chemistry Chemical Physics* **2016**, *18*, 32820.

(94) Zhong, D. K.; Choi, S.; Gamelin, D. R. *Journal of the American Chemical Society* **2011**, *133*, 18370.

(95) Furukawa, H.; Cordova, K. E.; O’Keeffe, M.; Yaghi, O. M. *Science* **2013**, *341*.

(96) Yaghi, O. M.; O'Keeffe, M.; Ockwig, N. W.; Chae, H. K.; Eddaoudi, M.; Kim, J. *Nature* **2003**, *423*, 705.

(97) Li, H.; Eddaoudi, M.; Groy, T. L.; Yaghi, O. M. *Journal of the American Chemical Society* **1998**, *120*, 8571.

(98) Li, M.; Li, D.; O’Keeffe, M.; Yaghi, O. M. *Chemical Reviews* **2014**, *114*, 1343.

(99) Eddaoudi, M.; Kim, J.; Rosi, N.; Vodak, D.; Wachter, J.; O'Keeffe, M.; Yaghi, O. M. *Science* **2002**, *295*, 469.

(100) Zhou, H.-C.; Long, J. R.; Yaghi, O. M. *Chemical Reviews* **2012**, *112*, 673.

(101) Getman, R. B.; Bae, Y.-S.; Wilmer, C. E.; Snurr, R. Q. *Chemical Reviews* **2012**, *112*, 703.

(102) Li, J.-R.; Sculley, J.; Zhou, H.-C. *Chemical Reviews* **2012**, *112*, 869.

(103) Li, J.-R.; Kuppler, R. J.; Zhou, H.-C. *Chemical Society Reviews* **2009**, *38*, 1477.

(104) Kong, X.; Scott, E.; Ding, W.; Mason, J. A.; Long, J. R.; Reimer, J. A. *Journal of the American Chemical Society* **2012**, *134*, 14341.

(105) Bloch, E. D.; Queen, W. L.; Krishna, R.; Zadrozny, J. M.; Brown, C. M.; Long, J. R. *Science* **2012**, *335*, 1606.

(106) Li-Chiang, L.; Jihan, K.; Xueqian, K.; Eric, S.; M., M. T.; R., L. J.; A., R. J.; Berend, S. *Angewandte Chemie International Edition* **2013**, *52*, 4410.

(107) Zhu, L.; Liu, X.-Q.; Jiang, H.-L.; Sun, L.-B. *Chemical Reviews* **2017**, *117*, 8129.

(108) Rossin, A.; Tuci, G.; Luconi, L.; Giambastiani, G. *ACS Catalysis* **2017**, *7*, 5035.

(109) Hendon, C. H.; Rieth, A. J.; Korzyński, M. D.; Dincă, M. *ACS Central Science* **2017**, *3*, 554.

(110) Li, Y.; Xu, H.; Ouyang, S.; Ye, J. *Physical Chemistry Chemical Physics* **2016**, *18*, 7563.

(111) Yang, S.; Pattengale, B.; Lee, S.; Huang, J. *ACS Energy Letters* **2018**, *3*, 532.

(112) Wei, W.; Xiaomin, X.; Wei, Z.; Zongping, S. *Advanced Science* **2017**, *4*, 1600371.

(113) Banerjee, R.; Phan, A.; Wang, B.; Knobler, C.; Furukawa, H.; O'Keeffe, M.; Yaghi, O. M. *Science* **2008**, *319*, 939.

(114) Phan, A.; Doonan, C. J.; Uribe-Romo, F. J.; Knobler, C. B.; O’Keeffe, M.; Yaghi, O. M. *Accounts of Chemical Research* **2010**, *43*, 58.

(115) Park, K. S.; Ni, Z.; Côté, A. P.; Choi, J. Y.; Huang, R.; Uribe-Romo, F. J.; Chae, H. K.; O’Keeffe, M.; Yaghi, O. M. *Proceedings of the National Academy of Sciences* **2006**, *103*, 10186.

(116) Nguyen, L. T. L.; Le, K. K. A.; Truong, H. X.; Phan, N. T. S. *Catalysis Science & Technology* **2012**, *2*, 521.

(117) Zhu, M.; Srinivas, D.; Bhogeswararao, S.; Ratnasamy, P.; Carreon, M. A. *Catalysis Communications* **2013**, *32*, 36.

(118) Miralda, C. M.; Macias, E. E.; Zhu, M.; Ratnasamy, P.; Carreon, M. A. *ACS Catalysis* **2012**, *2*, 180.

(119) Nguyen, L. T. L.; Le, K. K. A.; Phan, N. T. S. *Chinese Journal of Catalysis* **2012**, *33*, 688.

(120) Kuo, C.-H.; Tang, Y.; Chou, L.-Y.; Sneed, B. T.; Brodsky, C. N.; Zhao, Z.; Tsung, C.-K. *Journal of the American Chemical Society* **2012**, *134*, 14345.

(121) Isimjan, T. T.; Kazemian, H.; Rohani, S.; Ray, A. K. *Journal of Materials Chemistry* **2010**, *20*, 10241.

(122) Jing, H.-P.; Wang, C.-C.; Zhang, Y.-W.; Wang, P.; Li, R. *RSC Advances* **2014**, *4*, 54454.

(123) Ramesh, C.; Mala, N. *ChemistrySelect* **2017**, *2*, 7711.

(124) Wang, X.; Liu, J.; Leong, S.; Lin, X.; Wei, J.; Kong, B.; Xu, Y.; Low, Z.-X.; Yao, J.; Wang, H. *ACS Applied Materials & Interfaces* **2016**, *8*, 9080.

(125) Ding, Y.-H.; Zhang, X.-L.; Zhang, N.; Zhang, J.-Y.; Zhang, R.; Liu, Y.-F.; Fang, Y.-Z. *Dalton Transactions* **2018**, *47*, 684.

(126) Wang, S.; Wang, X. *Applied Catalysis B: Environmental* **2015**, *162*, 494.

(127) Wang, S.; Yao, W.; Lin, J.; Ding, Z.; Wang, X. *Angewandte Chemie International Edition* **2014**, *53*, 1034.

(128) Wang, S.; Lin, J.; Wang, X. *Physical Chemistry Chemical Physics* **2014**, *16*, 14656.

(129) Qin, J.; Wang, S.; Wang, X. *Applied Catalysis B: Environmental* **2017**, *209*, 476.

(130) Luo, W.; Yang, Z.; Li, Z.; Zhang, J.; Liu, J.; Zhao, Z.; Wang, Z.; Yan, S.; Yu, T.; Zou, Z. *Energy & Environmental Science* **2011**, *4*, 4046.

(131) Lin, C. T.; Boettcher, W.; Chou, M.; Creutz, C.; Sutin, N. *Journal of the American Chemical Society* **1976**, *98*, 6536.

(132) Yang, S.; Pattengale, B.; Kovrigin, E. L.; Huang, J. *ACS Energy Letters* **2017**, *2*, 75.

(133) Liu, T.; Zhou, X.; Dupuis, M.; Li, C. *Physical Chemistry Chemical Physics* **2015**, *17*, 23503.

(134) Abdi, F. F.; van de Krol, R. *The Journal of Physical Chemistry C* **2012**, *116*, 9398.

(135) Abdi, F. F.; Savenije, T. J.; May, M. M.; Dam, B.; van de Krol, R. *The Journal of Physical Chemistry Letters* **2013**, *4*, 2752.

(136) Seabold, J. A.; Choi, K.-S. *Journal of the American Chemical Society* **2012**, *134*, 2186.

(137) McKenna, K. P.; Shluger, A. L. *Proceedings of the Royal Society A: Mathematical, Physical and Engineering Science* **2011**, *467*, 2043.

(138) Greuter, F.; Blatter, G. *Semiconductor Science and Technology* **1990**, *5*, 111.

(139) Tamaki, Y.; Furube, A.; Murai, M.; Hara, K.; Katoh, R.; Tachiya, M. *Journal of the American Chemical Society* **2006**, *128*, 416.

(140) Ludwig, J.; An, L.; Pattengale, B.; Kong, Q.; Zhang, X.; Xi, P.; Huang, J. *The Journal of Physical Chemistry Letters* **2015**, *6*, 2671.

(141) Ravensbergen, J.; Abdi, F. F.; van Santen, J. H.; Frese, R. N.; Dam, B.; van de Krol, R.; Kennis, J. T. M. *The Journal of Physical Chemistry C* **2014**, *118*, 27793.

(142) Cho, S. K.; Park, H. S.; Lee, H. C.; Nam, K. M.; Bard, A. J. *The Journal of Physical Chemistry C* **2013**, *117*, 23048.

(143) Rettie, A. J. E.; Lee, H. C.; Marshall, L. G.; Lin, J.-F.; Capan, C.; Lindemuth, J.; McCloy, J. S.; Zhou, J.; Bard, A. J.; Mullins, C. B. *Journal of the American Chemical Society* **2013**, *135*, 11389.

(144) Jiang, C.; Wang, R.; Parkinson, B. A. *ACS Combinatorial Science* **2013**, *15*, 639.

(145) Luo, W.; Li, Z.; Yu, T.; Zou, Z. *The Journal of Physical Chemistry C* **2012**, *116*, 5076.

(146) Karakitsou, K. E.; Verykios, X. E. *The Journal of Physical Chemistry* **1993**, *97*, 1184.

(147) Thalluri, S. M.; Hernández, S.; Bensaid, S.; Saracco, G.; Russo, N. *Applied Catalysis B: Environmental* **2016**, *180*, 630.

(148) Heald, S. M.; DiMarzio, D.; Croft, M.; Hegde, M. S.; Li, S.; Greenblatt, M. *Physical Review B* **1989**, *40*, 8828.

(149) Dalba, G.; Fornasini, P. *Journal of Synchrotron Radiation* **1997**, *4*, 243.

(150) Ma, Y.; Pendlebury, S. R.; Reynal, A.; Le Formal, F.; Durrant, J. R. *Chemical Science* **2014**, *5*, 2964.

(151) Grigioni, I.; Stamplecoskie, K. G.; Selli, E.; Kamat, P. V. *The Journal of Physical Chemistry C* **2015**, *119*, 20792.

(152) Dey, C.; Banerjee, R. *Chemical Communications* **2013**, *49*, 6617.

(153) Sibo, W.; Wangshu, Y.; Jinliang, L.; Zhengxin, D.; Xinchen, W. *Angewandte Chemie International Edition* **2014**, *53*, 1034.

(154) Zhan, W.-w.; Kuang, Q.; Zhou, J.-z.; Kong, X.-j.; Xie, Z.-x.; Zheng, L.-s. *Journal of the American Chemical Society* **2013**, *135*, 1926.

(155) Corma, A.; Garcia, H. *Chemical Communications* **2004**, 1443.

(156) Lu, G.; Li, S.; Guo, Z.; Farha, O. K.; Hauser, B. G.; Qi, X.; Wang, Y.; Wang, X.; Han, S.; Liu, X.; DuChene, J. S.; Zhang, H.; Zhang, Q.; Chen, X.; Ma, J.; Loo, S. C. J.; Wei, W. D.; Yang, Y.; Hupp, J. T.; Huo, F. *Nature Chemistry* **2012**, *4*, 310.

(157) Pullen, S.; Fei, H.; Orthaber, A.; Cohen, S. M.; Ott, S. *Journal of the American Chemical Society* **2013**, *135*, 16997.

(158) Tsuruoka, T.; Kawasaki, H.; Nawafune, H.; Akamatsu, K. *ACS Applied Materials & Interfaces* **2011**, *3*, 3788.

(159) Buso, D.; Nairn, K. M.; Gimona, M.; Hill, A. J.; Falcaro, P. *Chemistry of Materials* **2011**, *23*, 929.

(160) Lohe, M. R.; Gedrich, K.; Freudenberg, T.; Kockrick, E.; Dellmann, T.; Kaskel, S. *Chemical Communications* **2011**, *47*, 3075.

(161) Falcaro, P.; Hill, A. J.; Nairn, K. M.; Jasieniak, J.; Mardel, J. I.; Bastow, T. J.; Mayo, S. C.; Gimona, M.; Gomez, D.; Whitfield, H. J.; Riccò, R.; Patelli, A.; Marmiroli, B.; Amenitsch, H.; Colson, T.; Villanova, L.; Buso, D. *Nature Communications* **2011**, *2*, 237.

(162) Johnson, J. A.; Luo, J.; Zhang, X.; Chen, Y.-S.; Morton, M. D.; Echeverría, E.; Torres, F. E.; Zhang, J. *ACS Catalysis* **2015**, *5*, 5283.

(163) Laurier, K. G. M.; Vermoortele, F.; Ameloot, R.; De Vos, D. E.; Hofkens, J.; Roeffaers, M. B. J. *Journal of the American Chemical Society* **2013**, *135*, 14488.

(164) Banerjee, R.; Phan, A.; Wang, B.; Knobler, C.; Furukawa, H.; O'Keeffe, M.; Yaghi, O. M. *Science* **2008**, *319*, 939.

(165) Xia, W.; Zhu, J.; Guo, W.; An, L.; Xia, D.; Zou, R. *Journal of Materials Chemistry A* **2014**, *2*, 11606.

(166) Yang, L.; Yu, L.; Sun, M.; Gao, C. *Catalysis Communications* **2014**, *54*, 86.

(167) Kornienko, N.; Resasco, J.; Becknell, N.; Jiang, C.-M.; Liu, Y.-S.; Nie, K.; Sun, X.; Guo, J.; Leone, S. R.; Yang, P. *Journal of the American Chemical Society* **2015**, *137*, 7448.

(168) Simmance, K.; Sankar, G.; Bell, R. G.; Prestipino, C.; Beek, W. v. *Physical Chemistry Chemical Physics* **2010**, *12*, 559.

(169) Yumashev, K. V.; Denisov, I. A.; Posnov, N. N.; Kuleshov, N. V.; Moncorge, R. *Journal of Alloys and Compounds* **2002**, *341*, 366.

(170) Cappel, U. B.; Feldt, S. M.; Schöneboom, J.; Hagfeldt, A.; Boschloo, G. *Journal of the American Chemical Society* **2010**, *132*, 9096.

(171) Klimov, V. I. *The Journal of Physical Chemistry B* **2000**, *104*, 6112.

(172) Boxer, S. G. *The Journal of Physical Chemistry B* **2009**, *113*, 2972.

(173) Bressler, C.; Chergui, M. *Chemical Reviews* **2004**, *104*, 1781.

(174) Chen, L. X. *Annual Review of Physical Chemistry* **2005**, *56*, 221.

(175) Sarangi, R.; Cho, J.; Nam, W.; Solomon, E. I. *Inorg Chem* **2011**, *50*, 614.

(176) Canton, S. E.; Zhang, X.; Zhang, J.; van Driel, T. B.; Kjaer, K. S.; Haldrup, K.; Chabera, P.; Harlang, T.; Suarez-Alcantara, K.; Liu, Y.; Pérez, J.; Bordage, A.; Pápai, M.; Vankó, G.; Jennings, G.; Kurtz, C. A.; Rovezzi, M.; Glatzel, P.; Smolentsev, G.; Uhlig, J.; Dohn, A. O.; Christensen, M.; Galler, A.; Gawelda, W.; Bressler, C.; Lemke, H. T.; Møller, K. B.; Nielsen, M. M.; Lomoth, R.; Wärnmark, K.; Sundström, V. *The Journal of Physical Chemistry Letters* **2013**, *4*, 1972.

(177) Pattengale, B.; Yang, S.; Ludwig, J.; Huang, Z.; Zhang, X.; Huang, J. *Journal of the American Chemical Society* **2016**, *138*, 8072.

(178) Butler, K. T.; Hendon, C. H.; Walsh, A. *ACS Applied Materials & Interfaces* **2014**, *6*, 22044.

(179) Grau-Crespo, R.; Aziz, A.; Collins, A. W.; Crespo-Otero, R.; Hernández, N. C.; Rodriguez-Albelo, L. M.; Ruiz-Salvador, A. R.; Calero, S.; Hamad, S. *Angewandte Chemie International Edition* **2016**, *55*, 16012.

(180) Butler, K. T.; Hendon, C. H.; Walsh, A. *Journal of the American Chemical Society* **2014**, *136*, 2703.

(181) Butler, K. T.; Worrall, S. D.; Molloy, C. D.; Hendon, C. H.; Attfield, M. P.; Dryfe, R. A. W.; Walsh, A. *Journal of Materials Chemistry C* **2017**, *5*, 7726.

(182) Sun, L.; Campbell, M. G.; Dincă, M. *Angewandte Chemie International Edition* **2016**, *55*, 3566.

(183) Stallinga, P. *Advanced Materials* **2011**, *23*, 3356.

(184) Worrall, S. D.; Mann, H.; Rogers, A.; Bissett, M. A.; Attfield, M. P.; Dryfe, R. A. W. *Electrochimica Acta* **2016**, *197*, 228.

(185) Rose, J.; Moulin, I.; Masion, A.; Bertsch, P. M.; Wiesner, M. R.; Bottero, J.-Y.; Mosnier, F.; Haehnel, C. *Langmuir* **2001**, *17*, 3658.

(186) Thanh, M. T.; Thien, T. V.; Du, P. D.; Hung, N. P.; Khieu, D. Q. *Journal of Porous Materials* **2017**.

(187) Yang, H.; He, X.-W.; Wang, F.; Kang, Y.; Zhang, J. *Journal of Materials Chemistry* **2012**, *22*, 21849.

(188) Schejn, A.; Aboulaich, A.; Balan, L.; Falk, V.; Lalevee, J.; Medjahdi, G.; Aranda, L.; Mozet, K.; Schneider, R. *Catalysis Science & Technology* **2015**, *5*, 1829.

(189) Shimizu, I.; Morimoto, Y.; Faltermeier, D.; Kerscher, M.; Paria, S.; Abe, T.; Sugimoto, H.; Fujieda, N.; Asano, K.; Suzuki, T.; Comba, P.; Itoh, S. *Inorganic Chemistry* **2017**, *56*, 9634.

(190) Troyanov, S. I.; Morozov, I. V.; Znamenkov, K. O.; Korenev, Y. M. *Zeitschrift für anorganische und allgemeine Chemie* **1995**, *621*, 1261.

(191) Frank, P.; Benfatto, M.; Hedman, B.; Hodgson, K. O. *Inorganic Chemistry* **2012**, *51*, 2086.

(192) Smith, T. A.; Penner-Hahn, J. E.; Berding, M. A.; Doniach, S.; Hodgson, K. O. *Journal of the American Chemical Society* **1985**, *107*, 5945.

(193) Kau, L. S.; Spira-Solomon, D. J.; Penner-Hahn, J. E.; Hodgson, K. O.; Solomon, E. I. *Journal of the American Chemical Society* **1987**, *109*, 6433.

(194) Pattengale, B.; Yang, S.; Lee, S.; Huang, J. *ACS Catalysis* **2017**, *7*, 8446.

(195) Heger, D.; Jirkovsk, J.; Kln, P. *The Journal of Physical Chemistry A* **2005**, *109*, 6702.

(196) Qian, J.; Sun, F.; Qin, L. *Materials Letters* **2012**, *82*, 220.

(197) Takizawa, T.; Watanabe, T.; Honda, K. *The Journal of Physical Chemistry* **1978**, *82*, 1391.

(198) Grau-Crespo, R.; Aziz, A.; Collins, A. W.; Crespo-Otero, R.; Hernández, N. C.; Rodriguez-Albelo, L. M.; Ruiz-Salvador, A. R.; Calero, S.; Hamad, S. *Angewandte Chemie International Edition* **2016**, *55*, 16012.

(199) White, J. L.; Baruch, M. F.; Pander, J. E.; Hu, Y.; Fortmeyer, I. C.; Park, J. E.; Zhang, T.; Liao, K.; Gu, J.; Yan, Y.; Shaw, T. W.; Abelev, E.; Bocarsly, A. B. *Chemical Reviews* **2015**, *115*, 12888.

(200) Wakerley, D. W.; Reisner, E. *Physical Chemistry Chemical Physics* **2014**, *16*, 5739.

(201) Popczun, E. J.; Read, C. G.; Roske, C. W.; Lewis, N. S.; Schaak, R. E. *Angewandte Chemie International Edition* **2014**, *53*, 5427.

(202) Caban-Acevedo, M.; Stone, M. L.; Schmidt, J. R.; Thomas, J. G.; Ding, Q.; Chang, H.-C.; Tsai, M.-L.; He, J.-H.; Jin, S. *Nat Mater* **2015**, *14*, 1245.

(203) Chen, E.-X.; Yang, H.; Zhang, J. *Inorganic Chemistry* **2014**, *53*, 5411.

(204) Juris, A.; Balzani, V.; Barigelletti, F.; Campagna, S.; Belser, P.; Von Zelewsky, A. *Coordination Chemistry Reviews* **1988**, *84*, 85.

(205) Horiuchi, Y.; Toyao, T.; Saito, M.; Mochizuki, K.; Iwata, M.; Higashimura, H.; Anpo, M.; Matsuoka, M. *The Journal of Physical Chemistry C* **2012**, *116*, 20848.

(206) Song, T.; Zhang, L.; Zhang, P.; Zeng, J.; Wang, T.; Ali, A.; Zeng, H. *Journal of Materials Chemistry A* **2017**, *5*, 6013.

(207) Kim, D.; Whang, D. R.; Park, S. Y. *Journal of the American Chemical Society* **2016**, *138*, 8698.

(208) Wen, M.; Mori, K.; Kamegawa, T.; Yamashita, H. *Chemical Communications* **2014**, *50*, 11645.

(209) He, J.; Wang, J.; Chen, Y.; Zhang, J.; Duan, D.; Wang, Y.; Yan, Z. *Chemical Communications* **2014**, *50*, 7063.

(210) Yuan, Y.-P.; Yin, L.-S.; Cao, S.-W.; Xu, G.-S.; Li, C.-H.; Xue, C. *Applied Catalysis B: Environmental* **2015**, *168–169*, 572.

(211) Fateeva, A.; Chater, P. A.; Ireland, C. P.; Tahir, A. A.; Khimyak, Y. Z.; Wiper, P. V.; Darwent, J. R.; Rosseinsky, M. J. *Angewandte Chemie International Edition* **2012**, *51*, 7440.

(212) Zhou, T.; Du, Y.; Borgna, A.; Hong, J.; Wang, Y.; Han, J.; Zhang, W.; Xu, R. *Energy & Environmental Science* **2013**, *6*, 3229.

(213) Sasan, K.; Lin, Q.; Mao, C.; Feng, P. *Chemical Communications* **2014**, *50*, 10390.

(214) Zhang, Z.-M.; Zhang, T.; Wang, C.; Lin, Z.; Long, L.-S.; Lin, W. *Journal of the American Chemical Society* **2015**, *137*, 3197.

(215) Nasalevich, M. A.; Becker, R.; Ramos-Fernandez, E. V.; Castellanos, S.; Veber, S. L.; Fedin, M. V.; Kapteijn, F.; Reek, J. N. H.; van der Vlugt, J. I.; Gascon, J. *Energy & Environmental Science* **2015**, *8*, 364.

(216) Zhang, Z. M.; Zhang, T.; Wang, C.; Lin, Z. K.; Long, L. S.; Lin, W. B. *Journal of the American Chemical Society* **2015**, *137*, 3197.

(217) Wang, C.; deKrafft, K. E.; Lin, W. B. *Journal of the American Chemical Society* **2012**, *134*, 7211.

(218) Shen, L. J.; Luo, M. B.; Huang, L. J.; Feng, P. Y.; Wu, L. *Inorganic Chemistry* **2015**, *54*, 1191.

(219) Kallioinen, J.; Benkö, G.; Sundström, V.; Korppi-Tommola, J. E. I.; Yartsev, A. P. *The Journal of Physical Chemistry B* **2002**, *106*, 4396.

(220) Kalyanasundaram, K. *Coordination Chemistry Reviews* **1982**, *46*, 159.

(221) Tian, F.; Cerro, A. M.; Mosier, A. M.; Wayment-Steele, H. K.; Shine, R. S.; Park, A.; Webster, E. R.; Johnson, L. E.; Johal, M. S.; Benz, L. *The Journal of Physical Chemistry C* **2014**, *118*, 14449.

(222) Della Longa, S.; Bianconi, A.; Palladino, L.; Simonelli, B.; Congiu Castellano, A.; Borghi, E.; Barteri, M.; Beltramini, M.; Rocco, G. P.; Salvato, B. *Biophysical Journal* **1993**, *65*, 2680.

(223) Hall, H. K. *Journal of the American Chemical Society* **1957**, *79*, 5441.